SPATIOTEMPORAL CHANGES OF SUPRAGLACIAL HYDROLOGY ON ELLESMERE ISLAND IN RESPONSE TO INCREASES IN SURFACE MELT

PÉNÉLOPE GERVAIS

A thesis submitted in partial fulfillment of the requirements for the

Master of Science degree in Geography

Department of Geography, Environment, and Geomatics

Faculty of Arts

University of Ottawa

Abstract

Over the past two decades, the Canadian Arctic Archipelago (CAA) has experienced unprecedented glacier mass loss, with surface melt and runoff contributing 90% of this decline since 2005. This has led to the formation and expansion of supraglacial streams and river networks. This study employs remotely sensed optical satellite imagery, historical air photographs, and digital elevation models (DEMs) to provide the first comprehensive spatiotemporal assessment of supraglacial drainage patterns on Ellesmere Island between 1959 and 2020.

Through multi-decadal qualitative and quantitative analyses of five glaciers along the ~830 km latitudinal gradient of Ellesmere Island, consistent drainage patterns influenced by surface topography were observed, which affects channelization and sinuosity. Substantial increases in drainage density (D_d) from 1959 to 2020 were driven by the expansion of perennial incised and canyon rivers, especially at higher elevations. This shift is observed through a reorganization of channel types towards a more perennial system, with incised rivers becoming predominant and canyons contributing more to the total channel length. Notably, Unnamed 1 Glacier on far northern Ellesmere Island has shown increased channelization of its perennial system and a trend towards straighter channels, while Unnamed 2 and John Evans glaciers to the south have experienced more pronounced canyon development in their lower ablation areas.

The presence of cold ice near the surface on Unnamed 1 Glacier, evidenced by limited sinks and numerous incised channels, results in high D_d dominated by canyon and incised rivers. Similarly, Henrietta-Nesmith Glacier's low moulin count and high canyon D_d suggest a comparable cold ice pattern. In contrast, southern glaciers with extensive moulin fields, such as Unnamed 2 and John Evans Glacier, show better supraglacial-subglacial connectivity, affecting the development of the subglacial system and glacier dynamics. The limited change in sinuosity, combined with channel dynamism, indicates varied stages of canyon evolution influenced by hydraulic factors such as surface slope and watershed area.

These findings align with modeled increases in surface melt, with southern glaciers experiencing higher melt production and rapid expansion of their supraglacial systems, while northern glaciers like Unnamed 1 show relative stability in part due to lower melt rates. In

contrast, greater cumulative summer losses on Sydkap combined with extensive crevassing limit the development of a perennial supraglacial system. Future climate warming is expected to raise the Equilibrium Line Altitude (ELA) and enhance melt rates at higher elevations, particularly impacting glaciers with a substantial amount of ice at mid-elevations, such as Unnamed 2. Although glaciers like Unnamed 1 may continue to expand their supraglacial systems, especially at higher elevations, this glacier's overall retreat suggests a future potential for complete glacier loss.

Acknowledgements

The completion of this thesis would not have been possible without the unwavering support and encouragement of numerous individuals and organizations.

First and foremost, I would like to express my sincere gratitude to my supervisor, Dr. Luke Copland. Your belief in me from the very beginning, especially during moments of self-doubt, has been invaluable. Thank you for listening patiently and offering guidance when I felt overwhelmed. Luke, you have taught me that it's okay to not be perfect, and for that, I thank you. Without this constant reminder, this thesis would probably not be complete. Thank you for providing me with countless opportunities to grow as an Arctic researcher, both in the field and at conferences. I have learned so much over the past two years and look forward to our future collaborations. I would also like to extend my gratitude to my committee members, Dr. Anders Knudby and Dr. Wesley Van Wychen, for their guidance and insightful feedback during the development stages of this work.

Support for this research has been graciously provided by the University of Ottawa and the Department of Geography, Environment and Geomatics. I am deeply thankful to the Northern Scientific Training Program (NSTP), the Remote-Ex Norwegian/Canadian/American Partnership Program, the Natural Sciences and Engineering Research Council of Canada (NSERC) Discovery Grant and Northern Supplement, and the NSERC Canada Graduate Scholarship – Master's. Additional support came from the Polar Continental Shelf Program (PCSP), ArcticNet Network of Centres of Excellence Canada, le Fonds de recherche du Québec – Nature et Technologies (Maîtrise), and Dr. Dorthe Dahl-Jensen (Canada Excellence Research Chair). I am also grateful to The Weston Family Foundation (Award in Northern Research), Amundsen Science, and the Canadian Coast Guard staff, as well as the amazing community of Grise Fiord.

A special thank you goes out to my labmates at the Laboratory for Cryospheric Research. Being surrounded by such talent and determination has been truly inspiring. Thank you for being incredible field teammates and turning fieldwork into a memorable adventure. A special shoutout to the Ottawa lab girlies – Erika, Jaime, and Brittany – for their support and constant encouragement. Seeing the light on in the lab and knowing you are there always brings a smile to my face.

Thank you to my amazing family and friends who have always supported me through all my endeavors. À mes parents, merci d'avoir soutenu mes rêves les plus fous et de m'avoir montré que tout est possible. Vous êtes les personnes les plus travaillantes que je connaisse et ma plus grande inspiration. Je n'aurais jamais pu le faire sans vous. Mes frérots, merci de m'avoir aidé à travers mes études, de m'avoir aidé à étudier pour me préparer à des examens, et de m'avoir apporté de la bouffe lorsque je ne mangeais pas assez.

I owe my deepest gratitude to my partner. Orin, thank you for your constant support and for building us a home while I was typing away at my computer. Thank you for forcing me away from my desk to take breaks and recenter myself. I could not have asked for a better life partner. Also, thank you to my second family who have always made me feel the most welcome and have supported me through it all.

Finally, to our little Mishka bear. Your big smile and your joy for life have been what has kept me going the last few months. Thank you for always keeping me company when times were tough.

Preface

This thesis is presented in a hybrid format under the supervision of Dr. Luke Copland, with plans to publish Chapter 2 as a collaborative paper with co-authors. Chapter 1 introduces the subject through a background and literature review, detailing the thesis structure and research objectives. Chapter 2 contains the manuscript intended for submission to a peer-reviewed journal, such as the Journal of Glaciology. All references are listed at the end of the thesis, and most tables and figures are included directly within the manuscript text, with a few presented in the Appendix. The manuscript (Chapter 2) is prepared in a format suitable for journal submission. The proposed title and authorship are as follows:

Gervais, P., Copland, L., Medrzycka, D., Noël, B., Dahl-Jensen, D., Alley, K. (in prep). Spatiotemporal Changes of Supraglacial Hydrology on Ellesmere Island in Response to Increases in Surface Melt.

As the primary author, I developed the methods and conducted the collection, analysis, and processing of most of the datasets in Chapter 2. Dr. Luke Copland, my thesis supervisor, provided crucial input and guidance throughout the project, including planning and organizing fieldwork logistics, and supplied historical air photographs and WorldView imagery. Dr. Dorota Medrzycka offered invaluable field training and assistance with troubleshooting during data analysis. Dr. Brice Noël contributed the modeled surface mass balance data used in the discussion, Dr. Dorthe Dahl-Jensen provided funding for the completion of this thesis and Dr. Karen Alley helped during my first field season on southern Ellesmere Island.

Table of Contents

List of Figures

List of Tables

List of Abbreviations

AAR	Accumulation Area Ratio
a.s.l.	Above Sea Level
ASTER	Advanced Spaceborne Thermal Emission and Reflection Radiometer
CAA	Canadian Arctic Archipelago
D_d	Drainage Density
DEM	Digital Elevation Model
ELA	Equilibrium Line Altitude
GCP	Ground Control Point
GIS	Geographic Information System
GrIS	Greenland Ice Sheet
MWU	Mann-Whitney U
NCAA	Northern Canadian Arctic Archipelago
$NDWI_{ice}$	Normalized Difference Water Index for Ice
QEI	Queen Elizabeth Islands
RACMO	Regional Atmospheric Climate Model
SCAA	Southern Canadian Arctic Archipelago
SD	Standard Deviation
SMB	Surface Mass Balance
SPOT	Satellite Pour l'Observation de la Terre
SSMB	Specific Surface Mass Balance
USGS	United States Geological Survey
UTM	Universal Transverse Mercator
W.Avg	Weighted Average
w.e.	Water Equivalent
WGS	World Geodetic System
W.SD	Weighted Standard Deviation
W.Skew	Weighted Skew
WV	WorldView

Chapter 1: Introduction

1.1 Background

1.1.1 Supraglacial Hydrology

Supraglacial hydrological networks activate on glacier surfaces during the summer melt season across the cryosphere (Pitcher and Smith, 2019). These networks typically form in unfissured depressions where meltwater from extensive catchment areas accumulates (Ferguson, 1973). They evolve as solar radiation initiates surface meltwater production within the still-intact seasonal snowpack. As the snowpack becomes saturated, slush flows can occur, initiating drainage toward lower elevations (Irvine-Fynn and others, 2011). Similar to hillslope processes in alluvial terrestrial systems, runoff begins when the near-surface ice becomes saturated (Cuffey and Paterson, 2010; Pitcher and Smith, 2019), which is more often observed below the snowline where the storage capacity of water is reduced, causing rapid flow (Dozier, 1974). Supraglacial channels facilitate the transport of this meltwater across the glacier surface, influencing the rate and efficiency at which water reaches the englacial, subglacial, and proglacial systems. Water is transferred to these systems through drainage via supraglacial lakes, crevasses, moulins, or directly off the ice surface (Fountain and Walder, 1998; Karlstrom and others, 2013; King and others, 2016; Nienow and others, 2017; Yang and others, 2019).

Collectively, supraglacial rivers and streams are referred to as channels. Pitcher and Smith (2019) define supraglacial rivers as perennially occupied incised channels, while supraglacial streams have a shallow depth and can change course annually. Supraglacial streams often serve as tributaries to these larger, regularly spaced mainstem channels, typically oriented parallel to ice flow in an elongated pattern (Rippin and others, 2015; Pitcher and Smith, 2019). As suggested by St. Germain and Moorman (2019), supraglacial channels can be classified into three categories: surface, incised, and canyon channels. Due to their evolutionary nature, surface channels can be considered "streams" as they can often change their course on an annual basis, while incised and canyon channels can be considered "rivers" as water often reoccupies these channels perennially. Canyons are larger, deeply incised rivers where the flowing water usually occupies only a small fraction of the total valley volume (St. Germain and Moorman, 2019). The formation and evolution of these stream and river networks are thought to be influenced by

factors such as meltwater supply, vertical incision rate, surface topography, and weathering crust hydrology (Pitcher and Smith, 2019).

While runoff originates from four main water sources—snowmelt, ablation of the glacier surface, summer precipitation (often as rain), and additional melting of the channel bed and walls through thermal and frictional erosion (Marston, 1983)—surface melt is widely recognized as the predominant source of meltwater for most glaciers (Bennett and Glasser, 2009). This meltwater plays a crucial role in providing the necessary water for the development and expansion of glacial hydrological networks (Bennett and Glasser, 2009). During the melt season and from year to year, changes in solar radiation, which affects air temperatures, can cause fluctuations in the supply of meltwater on glacier surfaces (Pitcher and Smith, 2019). The rate and amount of surface melt are controlled by the surface energy balance, which is given by:

$$Qm = Qn + Qh + Qr + Qe$$

where Qm is the energy available to melt ice, Qn is the net radiation, Qh is the sensible heat transfer, Qr is the sensible heat flux supplied by rain, and Qe is the latent heat transfer (Benn and Evans, 2010). Notably, Qn, which reflects the disparity between incoming and outgoing shortwave and longwave radiation, can contribute to over 75% of the total energy available to melt the ice (Arnold and others, 1996; Hock, 2005). Within this component, net shortwave radiation is the most important (Pellicciotti and others, 2005; Benn and Evans, 2010; Pitcher and Smith, 2019). Net shortwave radiation is strongly modulated by the glacier surface albedo, which encompasses the collective reflection of shortwave radiation across the entire spectrum of wavelengths (Mortimer and Sharp, 2018; Pitcher and Smith, 2019).

In the northern Canadian Arctic Archipelago (NCAA), Mortimer and Sharp (2018) revealed a strong negative correlation (r = -0.86) between black-sky shortwave broadband albedo and mean land surface temperature from 2001 to 2016. As the ice melts and surface snow is reduced, darker surfaces such as bare ice, meltwater ponds, and debris are exposed, which have a lower albedo than fresh snow or ice. This leads to a positive ice-albedo feedback, where decreasing albedo (less reflection, more absorption) leads to increased melting and subsequently higher rates of mass loss (Mortimer and Sharp, 2018). As demonstrated by Williamson and others

(2020), average modeled albedo measurements from the Moderate Resolution Imaging Spectroradiometer (MODIS) Terra satellite are highly correlated with the net annual mass balance of glaciers in the NCAA, indicating that interpolated albedo measurements alone can accurately estimate the annual mass balance of Arctic glaciers and ice caps in this region.

The associated changes in runoff and discharge can impact the frequency, geometry, and morphology of channels. Recent studies shed light on this phenomenon: Lu and others (2020) found a positive correlation between supraglacial drainage densities (D_d) and runoff estimates derived from Modèle Atmosphérique Régional on Devon Ice Cap, showing that the increase in D_d over a melt season was controlled by surface runoff. Meanwhile, St. Germain and Moorman (2019) found that high discharge was crucial for the evolution of perennial supraglacial rivers, as it increased incision due to thermal and frictional erosion of the channel bed. This aligns with earlier research by Marston (1983), who proposed a direct relationship between channel discharge and vertical incision. Additionally, St. Germain and Moorman (2019) noted a temporal increase in sinuosity in supraglacial rivers with higher discharge, owing to the greater eroding potential of the outer bank. Changes in sinuosity have been shown to be an important indicator of channel dynamism (Rippin and others, 2015), while also affecting overall D_d, which measures the total length of channels per unit area and reflects the degree of channelization and surface water flow across glaciers surfaces.

While the development and evolution of surface hydrological networks rely on and are modulated by meltwater supply (Ignéczi and others, 2018), supraglacial channels may only develop in areas where the rate of vertical channel incision exceeds the rate of surface ablation (Knighton, 1981; Marston, 1983; Gulley and others, 2009; Karlstrom and Yang, 2016; St. Germain and Moorman, 2019). Frictional and mechanical erosion, along with radiative and thermal melting, are the primary erosional agents leading to incision (St. Germain and Moorman, 2019). Modeled and measured absolute incision rates compiled by Pitcher and Smith (2019) yield a wide range of results, with modeled results showing incision rates as low as 1 cm day^{-1} on the Greenland Ice Sheet (GrIS) (Karlstrom and Yang, 2016) and greater than 10 cm day^{-1} on mountain glaciers in Switzerland, Russia, and Patagonia (Ferguson, 1973; Isenko and others, 2005). This

broad spectrum of results likely correlates with variations in the surface temperature of the ice, which can have a considerable impact on the surface hydrology.

Cold and polythermal glaciers exhibit higher rates of incision relative to surface ablation compared to temperate glaciers, while also having reduced rates of ice deformation which limits the formation of crevasses (Irvine-Fynn and others, 2011; Rippin and others, 2015). These conditions collectively enable the development of extensive networks of deeply incised perennial supraglacial rivers on glaciers with a greater cold ice content (Irvine-Fynn and others, 2011; Rippin and others, 2015), such as in the ablation area of glaciers in the NCAA (St. Germain and Moorman, 2019; Bash and others, 2022), Svalbard (Müller, 2007; Rippin and others, 2015) and northern Greenland (Rawlins and others, 2023). Lower surface ablation on these glaciers promotes increased network stability over time (Rippin and others, 2015), as evidenced by the presence of deeply incised channels (~10-30 m) and supraglacial lakes (Ryser and others, 2013). This is important as deeply incised rivers can create cut-and-closure channels through the incision and subsequent roof closure of supraglacial channels (Gulley and others, 2009). These channels facilitate efficient englacial flow paths and increase chances of water reaching the subglacial system (St. Germain and Moorman, 2016).

Once formed, supraglacial channels drain water along the path of the steepest slope direction, forming drainage patterns preconditioned by the glacier surface topography (Mantelli and others, 2015). Surface topography is influenced by external forcing such as variations in bed roughness, glacier dynamics (e.g., location of crevasses), glacier thickness and surface ablation (Ignéczi and others, 2018; Pitcher and Smith, 2019; St. Germain and Moorman, 2019; Lu and others, 2020). Yang and others (2019) found variability in drainage patterns on the GrIS, and Devon and Barnes ice caps in the Canadian Arctic Archipelago (CAA), which coincide with variations in surface topography. Dense supraglacial river drainage systems composed of straight and subparallel rivers were preferentially found in areas of low surface relief, while dendritic drainage networks occupied regions of high topographic variability. At a smaller scale, St. Germain and Moorman (2019) bridged an important knowledge gap on the long-term development of supraglacial channels, suggesting the importance of surface slope in the development of perennial rivers on Fountain Glacier, Bylot Island (CAA). The overall glacier

surface slope, which is controlled by surface topography, was found to increase the energy available to erode the channel bed and bank, increasing incision and sinuosity. This study found that increased sinuosity occurred due to inefficient dissipation of the energy of the flowing water by linear flow patterns. The resulting curvature of the channel reduced the slope and discharge velocity, inducing turbulence and allowing for greater erosion potential of the channel banks (St. Germain and Moorman, 2019).

1.1.2 Subglacial Connectivity

The efficacy at which surface-generated meltwater is transferred and distributed across all interconnected components of the glacier hydrological system has implications for glacier mass balance and, by extension, sea level rise (Nienow and others, 2017). Irvine-Fynn and others, (2011) suggest that each hydraulic subsystem exhibits spatial and temporal variability in their roles and activities, yet their interconnection profoundly influences ice dynamics. The accessibility of surface meltwater to the subglacial drainage system depends on two critical factors: the volume of surface meltwater produced and the temperature of the ice, which dictates the stress regime within the ice and thereby shapes the structure of the englacial system (Nienow and others, 2017). Understanding the factors influencing the prevalence, spatial distribution, and transport of surface meltwater between these systems (Yang and others, 2019) is essential for elucidating the complex relationship between glacier hydrology and dynamics; a topic which has become the primary motivation of the study of supraglacial hydrology.

The coupling between surface melt and glacier dynamics has the potential to accelerate ice losses, by transferring enhanced mass to lower elevations as surface meltwater accesses the glacier bed, raises basal water pressure, and induces basal sliding (Bennett and Glasser, 2009; Schoof, 2010; Irvine-Fynn and others, 2011; Smith and others, 2021). Where supraglacial channels terminate in moulins, large amounts of meltwater can be transported to the subglacial drainage system. On the southwest GrIS, Smith and others (2015) estimated a mean moulin discharge of 3.15 m^3 s^{-1} in July 2012, suggesting efficient meltwater routing through the supraglacial channel network (Smith and others, 2015). Water reaching the bed can increase basal water pressures when the amount of water exceeds the capacity of the subglacial drainage system to drain it, resulting in basal sliding and increased glacier motion (Iken, 1974; Zwally and

others, 2002; Nienow and others, 2017; Pitcher and Smith, 2019). According to Flowers (2015), the effectiveness of the subglacial hydrological system in draining meltwater and maintaining basal water pressure determines the amount of ice movement. However, uncertainties exist regarding the impact of future climate change and associated increases in surface melt on glacier motion. This is because enhanced subglacial water flow can either increase or lessen the sensitivity of glaciers to climate change by either speeding up glacier motion due to greater basal lubrication or reducing motion due to improved efficiency of the subglacial drainage system (Copland and others, 2003b; Van De Wal and others, 2008; Schoof, 2010; Thomson and Copland, 2017).

Several studies have established a correlation between surface ablation and summer velocities. In the 1960s and early 1970s, Iken (1974) provided the initial evidence that basal motion could occur beneath predominantly cold polythermal Arctic glaciers during the ablation season. Through her study on White Glacier on Axel Heiberg Island in the CAA, she confirmed that meltwater could infiltrate to the glacier bed, resulting in increased water pressure and the promotion of basal sliding (Iken, 1974; Flowers, 2015). More recently, Thomson and Copland (2017) expanded on Iken's work by combining her velocity observations from 1968-70 with those of Müller and Iken (1973) spanning 1960-68, and comparing them with more recent observations from 2012-16. Their analysis revealed a substantial reduction of up to 35% in summer velocities in the lower ablation area, accompanied by a 12% increase near the equilibrium line, between the periods of 1960-70 and 2012-16. They established a positive correlation between changes in summer velocities and surface ablation in the higher profile, while a weak negative correlation was observed in the lower profile. These observations suggested that the presence of subglacial drainage systems with varying levels of efficiency, together with long-term reductions in ice thickness, ultimately impacted the velocities (Thomson and Copland, 2017). A similar relationship was found at John Evans Glacier, Ellesmere Island, where the amount and spatiotemporal distribution of meltwater input to the glacier bed from the surface controlled the development of subglacial drainage pathways, affecting variations in short term and seasonal velocities (Copland and others, 2003b; Bingham and others, 2006). Additionally, on the western ablation zone of the GrIS, Van De Wal and others (2008) found that ice velocities can respond to changes

in meltwater input within a week, with velocities increasing up to 30% depending on the rate of ablation.

Despite the apparent correlation between summer velocity fluctuations and the influence of meltwater on the efficiency of subglacial drainage systems, long-term velocity measurements in relation to subglacial hydrology have yielded inconsistent results. In the CAA, Thomson and Copland (2017) discovered an important decrease of 38% in annual velocities on White Glacier between 1960-70 and 2012-16, while Schaffer and others (2017) observed a 12% slowdown per decade on glaciers on Penny Ice Cap over the period of 1985-2011. Similarly, Tedstone and others (2015) observed a 12% slowdown in ice motion on the western GrIS between 1985-94 and 2007-14, despite a 50% increase in meltwater production. These findings imply the presence of a positive feedback loop, wherein heightened meltwater inputs enhance the effectiveness of the subglacial drainage system, leading to reduced glacier velocities (Schoof, 2010). In contrast, Zwally and others (2002) found important interannual variations in ice velocity near the equilibrium zone of the western GrIS, where enhanced surface melting was associated with higher velocities and a greater potential for dynamic thinning at lower elevations. However, Van De Wal and others (2008) showed that no such feedback exists, as the subglacial system adapts to increases in meltwater inputs through time.

1.2 Thesis objectives

In the CAA, mass loss is predominantly driven by surface mass balance (SMB) processes, which reflect the net difference between gains from accumulation (snow and rain) and losses from melt and runoff (Gardner and others, 2011; Lenaerts and others, 2013; Mortimer and others, 2018; Van Wychen and others, 2020). Since 2005, surface mass balance losses have accounted for 90% of the total mass loss in the NCAA (the other ~10% coming from iceberg calving), an equivalent of 29.6 ± 3.0 Gt yr^{-1} (Millan and others, 2017). Given that glaciers in the NCAA are primarily polythermal, they have the potential to develop extensive perennial supraglacial drainage networks. However, few studies have comprehensively examined the temporal evolution of these networks in the CAA, with existing studies such as Lu and others (2020) focusing on large ice caps and shorter time scales. There is also a need to assess spatial differences between drainage networks to better understand internal (e.g. thermal regime) and

external (e.g. climate) controls on supraglacial hydrology to better predict their evolution under a warming climate. Thus, the primary objective of this thesis is to assess and quantify spatiotemporal changes in supraglacial hydrology on Ellesmere Island, the largest island in the NCAA, by:

a) Examining and manually delineating the supraglacial drainage networks of five different glaciers along the island's latitudinal gradient for the period 1959 to 2020.
b) Comparing and contrasting these drainage systems to understand how they evolve and respond in different physical and climatic environments.

These objectives are addressed using remote sensing techniques applied to a range of datasets, including optical satellite imagery, historical aerial photographs, and digital elevation models (DEMs). This allows for the first detailed, long-term quantification of the evolution of supraglacial hydrological networks across the NCAA, which is particularly pertinent given recent increases in surface melt since 2005 (Millan and others, 2017). Analyzing spatial variations in hydrological systems along Ellesmere Island's ~800 km latitudinal gradient also sheds light on differences in system development rates, crucial for understanding the impact of glacial surface temperatures on surface melt and the spatial distribution of these networks.

Chapter 2: Spatiotemporal Changes of Supraglacial Hydrology on Ellesmere Island in Response to Increases in Surface Melt

2.1 Introduction

The Arctic is undergoing rapid warming, with air temperatures rising at a rate four times faster than the global average (Rantanen and others, 2022). This phenomenon, known as Arctic amplification, is particularly pronounced in the Canadian Arctic Archipelago (CAA), which holds 28% of the world's land ice area outside of the ice sheets (Sharp and others, 2014). From 2002 to 2019, the CAA experienced the highest rate of glacier mass loss outside of the ice sheets, averaging 73 ± 9 Gt yr^{-1}, as observed by satellite data from the Gravity Recovery and Climate Experiment (Gardner and others, 2013; Vaughan and others, 2013; Ciracì and others, 2020). During this period, the Northern Canadian Arctic Archipelago (NCAA) saw a greater relative mass loss compared to the Southern Canadian Arctic Archipelago (SCAA), with an average loss approximately 9.4 Gt yr^{-1} higher (Ciracì and others, 2020).

Surface melt is the primary driver of this mass loss, accounting for 90% of the total mass losses in the NCAA since 2005, leading to the formation and expansion of supraglacial hydrological networks (Millan and others, 2017; Lu and others, 2020). Supraglacial meltwater channels play a crucial role in a glacier's hydrological system, influencing surface mass balance (SMB) and forming the primary link between the surface, englacial, and subglacial systems (Pitcher and Smith, 2019). When supraglacial rivers terminate in sinks such as moulins and large crevasses, large volumes of water can transfer to the glacier bed, impacting basal water pressure and the development of subglacial hydrological systems (Lu and others, 2020). A key unresolved question in climate change assessments is whether this increased subglacial water flow will amplify or diminish glaciers' sensitivity to climate change, either by accelerating glacier motion due to enhanced basal lubrication or by reducing motion due to improved efficiency of the subglacial drainage system (Schoof, 2010; Thomson and Copland, 2017).

Recent advancements in remote sensing (Yang and others, 2019; Bash and others, 2022), numerical modeling (King and others, 2016), and field studies (St. Germain and Moorman, 2019) have significantly enhanced our understanding of supraglacial hydrological networks. Despite

these advances, supraglacial systems remain among the least studied hydrological components on Earth (Yang and others, 2019). Recent studies have begun to bridge this gap through the delineation of supraglacial hydrological features which has been facilitated by the availability of high-resolution (e.g., WorldView-2, 0.5 m) (Yang and others, 2015a) to moderate-resolution (e.g., Sentinel-2, 10 m) (Yang and others, 2017; Lu and others, 2020) satellite imagery and digital elevation models (DEMs) such as the ArcticDEM (Rippin and others, 2015; King and others, 2016; Yang and others, 2018; Bash and others, 2022). Mapping is the most direct method to identify these features (Yang and others, 2015b) and contributes to a deeper understanding of the glacial hydrological system as a whole (Chu, 2014; Yang and others, 2019; Bash and others, 2022). Despite these advances and the important climatic changes observed in the CAA, research on supraglacial channels in this region remains limited, with most recent large-scale studies having taken place on the Greenland Ice Sheet (GrIS) (Yang and Smith, 2013; Yang and others, 2015a; King and others, 2016; Yang and others, 2017; Yang and others, 2019; Lu and others, 2020). Studies focusing on glaciers in the CAA have primarily been centered on major ice caps like Barnes and Devon (Wyatt and Sharp, 2015; Yang and others, 2019; Lu and others, 2020). An exception is the recent studies by Bash and others, (2022) and Kochtitzky and others, (2023), which mapped supraglacial drainage networks in the ablation area of Thores Glacier on northern Ellesmere Island. Together, these studies have contributed to the development or refinement of methodological frameworks for supraglacial hydrology mapping (Yang and others, 2019; Bash and others, 2022), have assessed the evolution of the supraglacial drainage system over a single melt season (Lu and others, 2020), or have explored the relationship between surface melt and glacier dynamics for single points in time (Wyatt and Sharp, 2015; Yang and others, 2019).

Long-term studies of supraglacial hydrological networks also remain sparse. While St. Germain and Moorman (2019) made initial strides in addressing this gap in the CAA by studying the evolution of specific streams and rivers on Fountain Glacier, Bylot Island, their research focused on a relatively short period (2010-2017), capturing only a snapshot of their evolution. Although Kochtitzky and others (2023) mapped the development of supraglacial channels over the last ~60 years, their study focused solely on predominant rivers in the ablation area so did not capture fluctuations within the entire supraglacial system. Studies are therefore needed to

capture the multi-decadal evolution of supraglacial hydrological networks across entire glacier basins in the CAA, enhancing our understanding of their spatiotemporal dynamics and changes in a warming climate.

In this study, we employ a combination of optical satellite imagery, digital elevation models (DEMs), and historical air photographs to manually map supraglacial channel networks and assess their multi-decadal evolution across selected glaciers on Ellesmere Island in the NCAA. We quantify their temporal changes over approximately 60 years by analyzing shifts in supraglacial drainage patterns and the composition of different channel types within the drainage system. We also evaluate spatial differences among glaciers to better understand the magnitude of change in supraglacial systems situated in varied environmental settings. This research provides the first multi-decadal quantification of the evolution of supraglacial hydrological networks across the NCAA, contributing novel insights into their response to changes in climate.

2.2 Study Area

Ellesmere Island, Nunavut, is the largest of the Queen Elizabeth Islands (QEI), which collectively form the NCAA (Sharp and others, 2014; Curley and others, 2021). Approximately 40% (~77,516 km²) of its land area is glacierized, with ~53% (~41,222 km²) comprising land-terminating glaciers, while ~47% (~36,294 km²) consists of marine-terminating glaciers (Millan and others, 2017; White and Copland, 2018). The island experiences a pronounced air temperature gradient from south to north and a precipitation gradient extending from southeast to northwest (Koerner, 1979). Precipitation is highest along the coastlines facing Baffin Bay and decreases with elevation and distance inland.

The current study focuses on five glaciers located along the ~830 km latitudinal gradient of Ellesmere Island (Figure 1). These glaciers were selected based on data availability, the presence of a perennial supraglacial system (except for Sydkap Glacier, which was included for comparison), and their geographic distribution to capture a gradient across the island:

1. Sydkap Glacier (76.686°N, 85.461°W) is a large marine terminating glacier with a basin area of ~475 km^2, draining the southern side of Sydkap Ice Cap. It is the only glacier in the study

area which has previously been identified as surge type (Copland and others, 2003a). It lost 36.41 km^2 of ice due to calving between 1959 and 2019 (Smith and others, 2020), resulting in a terminus retreat exceeding 9 km, one of the greatest in the CAA (Copland and others, 2003a).

2. Unnamed 2 Glacier (78.793°N, 76.538°W) is a large land-terminating glacier which drains the northern part of the Prince of Wales Icefield, with a basin size of ~242 km^2 and elevation range from 30 to 1800 m above sea level (a.s.l). Research conducted on nearby glaciers has reported rapid rates of mass loss since the mid-20th century (Bergsma and others, 1984), with rates nearly doubling between 1959-2001 and 2001-19, and the equilibrium line altitude (ELA) rising by 77 m between 1974-1982 and 2014-2019 (Curley and others, 2021).
3. John Evans Glacier (79.650°N, 74.187°W) is a predominantly cold polythermal glacier which covers an area of ~79 km^2 and spans about 15 km, with elevations ranging from ~100 to 1500 m a.s.l. Previous studies have observed a well-developed supraglacial drainage network below the ELA at around 800 m during a melt season lasting about 60 days (Bingham and others, 2006). The surface hydrological network is strongly linked to the subglacial drainage system (Bingham and others, 2005), with marked seasonal variability in glacier dynamics (Copland and others, 2003b; Bingham and others, 2006).
4. Henrietta-Nesmith Glacier (81.857°N, 73.059°W) drains the central eastern region of the Northern Ellesmere Icefield, covering ~1043 km^2 and with elevations ranging from 100 to 2500 m a.s.l. Flowing from near the highest point on Ellesmere Island (Hattersley-Smith, 1961), it contributes substantially to Lake Hazen's hydrological input (Cavaco and others, 2019).
5. Unnamed 1 Glacier (82.998°N, 72.855°W) is the smallest of the studied glaciers, with a basin area of approximately 18 km^2 and elevations ranging from 30 to 980 m a.s.l. This glacier lies southeast of Ward Hunt Island near Canada's northernmost point and has never been previously studied.

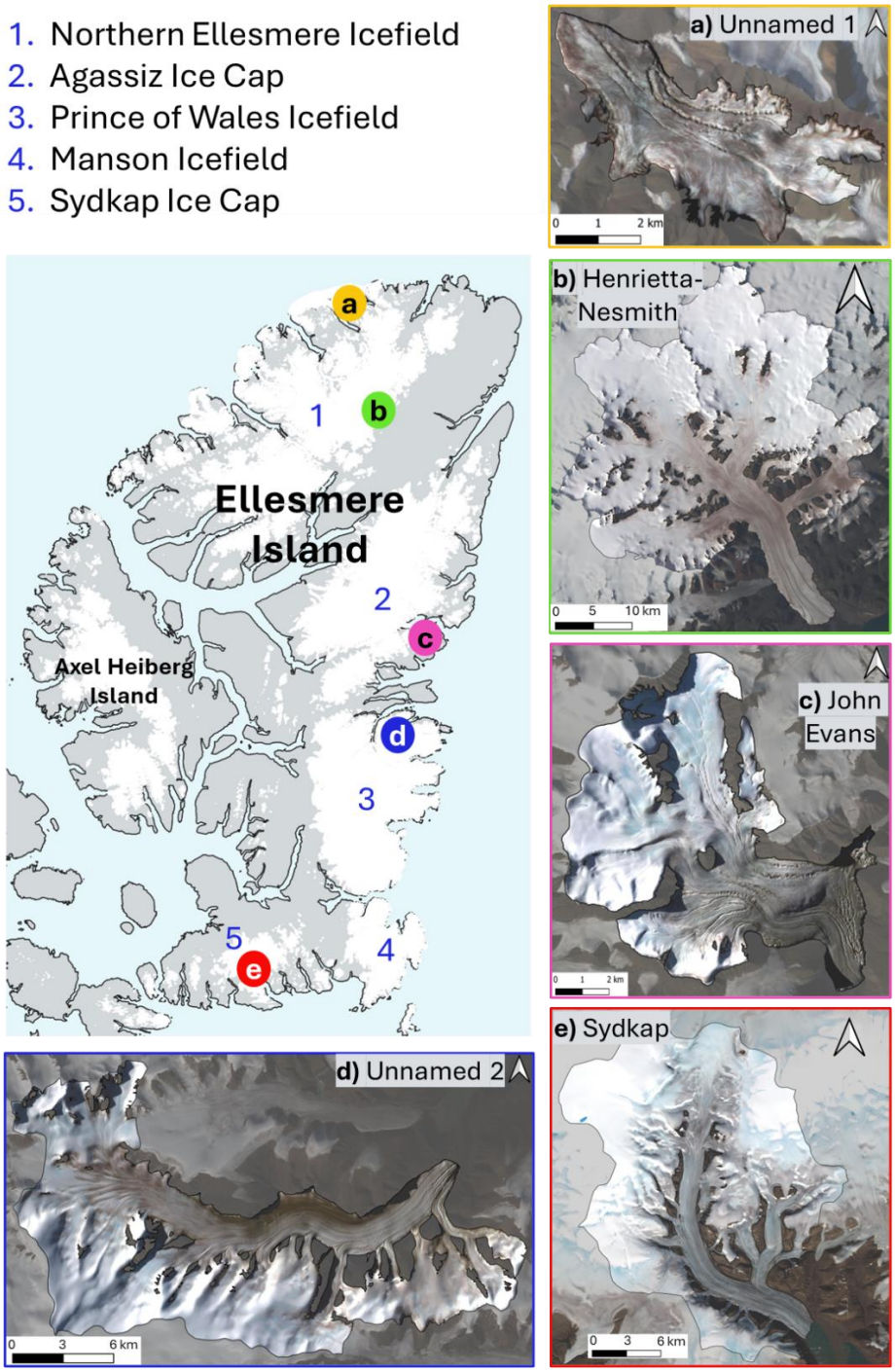

Figure 1. Location of the main icefields and ice caps, as well as the 5 studied glaciers, on Ellesmere Island. Projection: Canada Lambert Conformal Conic (main map), WGS UTM 16N (Sydkap Glacier) and WGS UTM 18N (glaciers Unnamed 2 through Unnamed 1). Data: Statistics Canada, 2016 Census - Provinces/territories – Cartographic Boundary File (2016 Census Boundary files (statcan.gc.ca)). Natural Resources Canada - Lakes, Rivers and Glaciers in Canada – CanVec Series – Hydrographic Features (Lakes, Rivers and Glaciers in Canada - CanVec Series - Hydrographic Features - Open Government Portal).

2.3 Data and Methods

2.3.1 Time Series Analysis

Various contemporary optical satellite images from Sentinel-2 and PlanetScope were compared to ASTER and SPOT images, and historical air photographs, to provide a visual record of temporal and spatial changes in supraglacial hydrology across Ellesmere Island since the late 1950s (Tables 1, 2). Multidecadal time series were created for the five studied glaciers to provide a qualitative analysis of the evolution of their supraglacial drainage networks, with the aim to acquire images every ~10 years, although this was not always possible due to image availability, particularly before 2000.

In addition, the supraglacial drainage networks of the four glaciers north of Sydkap were examined in more detail by manually delineating channels on 3 m resolution PlanetScope images from 2020 following specific criteria (section 2.3.6) (Table 2). Sydkap was omitted from this analysis as no well-defined perennial drainage system has developed on this glacier. Mapping efforts were extended back to 1959 by also delineating channels on ~0.6 m resolution historical air photographs of the four glaciers (Table 1). Channels under ~3 m width (5 pixels in the air photos) were excluded from the final map to match the resolution of PlanetScope images, ensuring consistent quantification over time. Although the channel networks were examined at various scales to better interpret features in the images, all delineation was performed at a scale of 1:2500 (meaning that one pixel in the PlanetScope imagery represents 1.2 mm on the screen) to ensure consistency between glaciers and across years. This scale also facilitated clear differentiation of tones and textures in the imagery (Bash et al., 2022).

Detailed quantitative mapping of supraglacial channels was only undertaken in 1959 and 2020 due to the high resolution of the PlanetScope imagery and historical air photos (hereafter, referred to as 'quantitative analysis'). Sentinel-2, ASTER, and SPOT imagery have a coarser spatial resolution (10+ m), and are therefore only able to capture continuous channels ~10 m wide or greater. Consequently, these images could not be used to accurately quantify changes in the supraglacial systems over time when compared to the detailed 1959 and 2020 maps, but they still provided useful information concerning the evolution of larger channels in intervening years (hereafter, referred to as 'qualitative analysis').

For these analyses, cloud-free images were preferentially acquired in July and August, during minimum annual snow cover when supraglacial drainage systems were fully developed (Tables 1, 2). This was especially important to facilitate their mapping under consistent surface conditions. The only exceptions are the two main historical air photos of John Evans Glacier from June 5, 1959, when no other imagery was available.

2.3.1.1 Equilibrium Line Altitude

Additionally, to better understand the distribution of channels and the factors driving the formation and expansion of supraglacial hydrological systems, the recent ELA was estimated from the average elevation of the snowline in cloud-free, late summer (July to August) Sentinel-2 and PlanetScope satellite imagery spanning 2016 to 2020, using the methodology of Kochtitzky and others (2023) (Table 2). Snowline measurements are used as a proxy for the ELA, which Casey and Kelly (2010) found to be the most accurate method based on their comparison of field and remote sensing data from Devon Ice Cap. We acknowledge that this approach does not account for variations in the superimposed ice zone which can contribute additional mass to the glacier below the snowline. For each year, the snowline was manually delineated for all five glaciers by tracing the boundary between snow-covered and snow-free glacier surfaces in the late summer imagery. Except for Unnamed 1, which only had images available in 2017 and 2020, the ELA on all other glaciers was traced on four to five images. Each polyline was then overlaid on top of a 2 m resolution ArcticDEM (Table 3) from 2020, with elevation values along the lines extracted and the average calculated. A contour line at the average elevation was subsequently drawn across each glacier surface to represent the ~2020 ELA.

The 1960 ELAs over the studied glaciers were estimated using regional reconstructions of the lowest ELA first conducted by Miller and others (1975) and later recreated by Wolken and others (2008). In the original maps, the ELA was estimated by identifying the elevation dividing accumulation and ablation areas, based on the lowest elevation of cirque glaciers or small ice caps across different regions of the QEI, considering changes in contour inflection and orographic effects, and plotting the estimates directly on base maps to minimize positioning errors. More recently, White and Copland (2018) digitized the recreated map of Wolken and others (2008) for

northern Ellesmere Island and overlaid it on a Landsat 8 mosaic from 2015/16. This facilitated our estimate for the smallest glacier, Unnamed 1, located near the northern coast of Ellesmere Island.

2.3.2 Historical Air Photographs

The earliest available imagery of the glaciers was 1959 panchromatic 1:60,000 scale vertical aerial photographs archived at the National Air Photo Library in Ottawa, Canada (Table 1). These images were acquired by the Royal Canadian Air Force and taken from an altitude of 9000 m a.sl. using a Wild RC5A aerial film camera and Aviogon lens (15 AG). The 9 inches by 9 inches (22.9 cm by 22.9 cm) images were scanned at a resolution of 2033 dpi, resulting in a ground resolution of ~0.6 m. Since high-resolution imagery (~0.6 m) was only available for sections of each glacier where channels were present, lower-resolution air photos scanned at 300 dpi with a ground resolution of ~4 m were used to get coverage of entire glacier surfaces for the further analyses described later in the methods.

Table 1. Air photos used for the qualitative (multidecadal time series) and quantitative (channel delineation) assessments of the supraglacial drainage systems on all 5 studied glaciers in 1959.

Glacier	Roll Number	ID	Date (dd-mm-yyyy)	Ground resolution (m)
Sydkap	A16724	0190	13-08-1959	~4
Unnamed 2	A16613	0106	07-07-1959	~0.6
Unnamed 2	A16726	0084	12-08-1959	~0.6
Unnamed 2	A16679	0073	15-07-1959	~0.6
Unnamed 2	A16794	0023	22-08-1959	~0.6
Unnamed 2	A16974	0025	22-08-1959	~4
Unnamed 2	A16679	0072	15-07-1959	~4
John Evans	A16607	0193	05-06-1959	~0.6 and ~4
John Evans	A16607	0192	05-06-1959	~0.6
John Evans	A16616	0059	05-07-1959	~4
Henrietta-Nesmith	A16613	0035	07-07-1959	~0.6
Henrietta-Nesmith	A16679	0155	15-07-1959	~0.6
Henrietta-Nesmith	A16687	0069	28-07-1959	~4
Unnamed 1	A16708	0005	29-07-1959	~0.6

2.3.3 Satellite Imagery

Satellite scenes used in both the qualitative and quantitative analyses were downloaded from various sources (Table 2). SPOT 1-5 imagery covering the period from 1986 to 2015 was

downloaded directly from the Spot World Heritage data site (https://regards.cnes.fr/user/swh/modules/60). Most of the SPOT images were downloaded as L1A products and required slight geometrical corrections. In such cases, the 'Shift' function in ArcGIS Pro's georeferencing menu was used to align the glacier surface area in the SPOT image with the most recent image in the time series, either a PlanetScope or Sentinel-2 image. ASTER images, available since 1999 and acquired from the United States Geological Survey (USGS) EarthExplorer database (https://earthexplorer.usgs.gov/), were used to fill gaps in the time series when SPOT images were not available after 1999. Sentinel-2 and PlanetScope imagery covered the most recent period since 2015, with Sentinel-2 images acquired from the Copernicus Open Access Hub (https://www.copernicus.eu/en) and the PlanetScope imagery downloaded through the Education and Research Program, courtesy of Planet Images (https://www.planet.com/). In addition, two WorldView-2 (WV2) and one WorldView-3 (WV3) image from 2022 covering the surface of Unnamed 2 and Unnamed 1 glaciers, respectively, were acquired through the European Space Agency's Third-Party Missions program and used as validation for the mapping of sinks.

Table 2. Satellite imagery used for qualitative and quantitative time series analyses, including supraglacial channel delineation, sink identification, and delineation of the 2020 ELA.

Glacier	Image ID	Platform	Date (dd-mm-yyyy)	Ground Resolution (m)
Sydkap	20200810_173013_45_2304	PlanetScope	10-08-2020	3
Sydkap	20200810_174130_88_222b	PlanetScope	10-08-2020	3
Sydkap	5 074-138/7 12/08/02 18:28:43 2 J	SPOT-5	02-08-2012	10
Sydkap	S2A_MSIL2A_20160809T190922_N0500_R056_T16XEL_20231001T044540	Sentinel-2	09-08-2016	10
Sydkap	S2A_MSIL2A_20170818T184921_N0500_R113_T16XEL_20230828T114505	Sentinel-2	18-08-2017	10
Sydkap	S2A_MSIL2A_20190814T190921_N0500_R056_T16XEL_20230506T041706	Sentinel-2	14-08-2019	10
Sydkap	S2B_MSIL1C_20200725T183919_N0209_R070_T16XEL_20200725T204817	Sentinel-2	25-07-2020	10
Unnamed 2	S2A_MSIL2A_20160813T184922_N0500_R113_T18XVN_20230928T183909	Sentinel-2	13-08-2016	10
Unnamed 2	S2A_MSIL2A_20170817T191911_N0500_R099_T18XVN_20230826T215252	Sentinel-2	17-08-2017	10
Unnamed 2	S2A_MSIL2A_20180802T191911_N0500_R099_T18XVN_20230802T133144	Sentinel-2	02-08-2018	10
Unnamed 2	S2A_MSIL2A_20190814T190921_N0500_R056_T18XVN_20230506T041706	Sentinel-2	14-08-2019	10

Unnamed 2	20200723_000923_09_2257	PlanetScope	23-07-2020	3
Unnamed 2	20200723_000925_31_2257	PlanetScope	23-07-2020	3
Unnamed 2	S2A_MSIL2A_20200806T182921_N0500_R027_T18XWP_20230507T144903	Sentinel-2	06-08-2020	10
Unnamed 2	22AUG02002430-P2AS016259646030_01_P001	WorldView-2	22-08-2022	0.5
Unnamed 2	22AUG02002419-P2AS-016259646030_01_P002	WorldView-2	22-08-2022	0.5
Unnamed 2	AST_L1T_00307192002182828_20150423085645_16236	Terra/ASTER	19-07-2002	15
Unnamed 2	5 083-137 11/07/13 18:59:45 2 J	SPOT-5	13-07-2011	10
John Evans	1 088-137 87-07-12 19:02:22 2 P	SPOT-1	12-07-1987	20
John Evans	AST_L1T_00307192002182810_20150423085643_1600	Terra/ASTER	19-07-2002	15
John Evans	5 088-137 11/08/03 18:55:19 1 A	SPOT-5	03-08-2011	5
John Evans	S2A_MSIL2A_20160723T191912_N0500_R099_T18XWP_20231007T044659	Sentinel-2	23-07-2016	10
John Evans	S2A_MSIL2A_20170805T183921_N0500_R070_T18XWP_20231001T225130	Sentinel-2	05-08-2017	10
John Evans	S2A_MSIL2A_20180802T191911_N0500_R099_T18XWP_20230802T133144	Sentinel-2	02-08-2018	10
John Evans	S2A_MSIL2A_20190814T190921_N0500_R056_T18XWP_20230506T041706	Sentinel-2	14-08-2019	10
John Evans	20200723_000758_98_105c	PlanetScope	23-07-2020	3
John Evans	20200723_000757_10_105c	PlanetScope	23-07-2020	3
John Evans	S2A_MSIL2A_20200728T193911_N0500_R042_T18XWP_20230324T093756	Sentinel-2	28-07-2020	10
Henrietta-N	S2A_MSIL2A_20160730T205022_N0500_R057_T18XWS_20231006T211410	Sentinel-2	30-07-2016	10
Henrietta-N	S2A_MSIL2A_20180802T210021_N0500_R100_T18XWS_20230719T190339	Sentinel-2	02-08-2018	10
Henrietta-N	S2A_MSIL2A_20190814T205021_N0500_R057_T18XWS_20230504T233540	Sentinel-2	14-08-2019	10
Henrietta-N	S2A_MSIL2A_20200730T201901_N0500_R071_T18XWS_20230327T110228	Sentinel-2	30-07-2020	10
Henrietta-N	20200724_073642_33_1065	PlanetScope	24-07-2020	3
Henrietta-N	20200724_073643_88_1065	PlanetScope	24-07-2020	3
Henrietta-N	20200724_073645_43_1065	PlanetScope	24-07-2020	3
Henrietta-N	20200724_073646_98_1065	PlanetScope	24-07-2020	3
Henrietta-N	20200724_073648_54_1065	PlanetScope	24-07-2020	3
Henrietta-N	20200724_074509_69_106a	PlanetScope	24-07-2020	3
Henrietta-N	20200724_074511_23_106a	PlanetScope	24-07-2020	3
Henrietta-N	20200724_074512_78_106a	PlanetScope	24-07-2020	3
Henrietta-N	20200724_074514_32_106a	PlanetScope	24-07-2020	3
Henrietta-N	20200724_074515_87_106a	PlanetScope	24-07-2020	3
Henrietta-N	20200724_210831_86_105c	PlanetScope	24-07-2020	3
Henrietta-N	20200724_210833_73_105c	PlanetScope	24-07-2020	3

Henrietta-N	S2A_MSIL2A_20200730T201901_N0500_R071_T19XDL_20230327T110228	Sentinel-2	30-07-2020	10
Henrietta-N	AST_L1T_00307292000201838_20150410170513_38964	Terra/ASTER	29-07-2000	15
Henrietta-N	AST_L1T_00308282012193314_20150612110915_77182	Terra/ASTER	28-08-2012	15
Unnamed 1	1 091-124 88-08-08 19:44:22 1 X	SPOT-1	08-08-1988	20
Unnamed 1	AST_L1T_00307142009205316_20150528225353_32576	Terra/ASTER	14-07-2009	15
Unnamed 1	20170729_101731_0f2e	PlanetScope	29-07-2017	3
Unnamed 1	20170729_101732_0f2e	PlanetScope	29-07-2017	3
Unnamed 1	20200723_204401_82_2257	PlanetScope	23-07-2020	3
Unnamed 1	20200723_204404_04_2257	PlanetScope	23-07-2020	3
Unnamed 1	20JUL20221803-P2AS-016259646020_01_P001	WorldView-3	20-07-2022	0.5

2.3.4 Digital Elevation Models (DEMs)

To assist with mapping in shadowed and low contrast regions in satellite imagery, a shaded relief raster (hillshade model) was used as a support. Specifically, strips from ArcticDEM version 4.1 from the Polar Geospatial Center (https://www.pgc.umn.edu/data/arcticdem/) were used for this purpose (Table 3). ArcticDEM is a pan-Arctic 2 m resolution DEM constructed from stereo imagery acquired by the DigitalGlobe satellites, with data available in two formats: raster "strips" and "mosaic tiles". The former is derived from single image pairs, preserving the original time stamp, while the latter is composed of coregistered and blended strips, often from different years. Due to the time-dependent nature of this study, strips from a single date were preferred over mosaics to accurately quantify temporal changes (Table 3). The selected strip dates were aligned closely with the dates of the PlanetScope images for each glacier, which is essential when using both datasets to avoid misclassification of channels with less-well defined banks (Bash and others, 2022).

The hillshade model was generated in QGIS v 3.24 utilizing the Hillshade tool within the GDAL library. To enhance the visibility of depressions a solar altitude angle of 45° was chosen, and the lighting direction was aligned perpendicular to the predominant flow of the glacier given that channels typically align parallel to the glacier flow (Bash and others, 2022). Therefore, an azimuth of 180° was selected for Unnamed 1 and Unnamed 2 glaciers, while an azimuth of 225° was used for John Evans and Henrietta-Nesmith glaciers. The hillshade model was produced without

including shading from adjacent terrain, focusing solely on shading from local relief, providing a grayscale depiction of the vertical relief of the glacier surface.

Although the supraglacial drainage network of Sydkap was not mapped quantitatively, ArcticDEM strips were downloaded to determine the ELA for this glacier, as described above. Details of all the strips used are provided in Table 3 below.

Table 3. ArcticDEM strips used to generate hillshade models and determine the ~2020 equilibrium line altitudes for each examined glacier.

Glacier	Geocell	Strip ID	Date
Sydkap	n76w086	SETSM_s2s041_WV01_20200502_10200100986EB600_1020010095C00200_2m_lsf_seg1	02-05-2020
Sydkap	n76w087	SETSM_s2s041_WV01_20210425_10200100AF293100_10200100B072F300_2m_lsf_seg1	25-04-2021
Sydkap	n76w086	SETSM_s2s041_WV03_20210514_10400100686F1900_10400100687BC100_2m_lsf_seg1	14-05-2021
Unnamed 2	n78w077	SETSM_s2s041_WV02_20200727_10300100AAB0A800_10300100AB6B5500_2m_lsf_seg1	27-07-2020
Unnamed 2	n78w077	SETSM_s2s041_WV03_20200729_104001005D843300_104001005D875F00_2m_lsf_seg1	29-07-2020
Unnamed 2	n78w077	SETSM_s2s041_WV03_20200729_104001005E8E9600_104001005F2B9D00_2m_lsf_seg1	29-07-2020
John Evans	n79w075	SETSM_s2s041_WV02_20200726_10300100A91BD800_10300100A91F7700_2m_lsf_seg6	26-07-2020
Henrietta-Nesmith	n82w074	SETSM_s2s041_WV01_20200713_1020010099DFB800_102001009E34D600_2m_lsf_seg1	13-07-2020
Henrietta-Nesmith	n81w075	SETSM_s2s041_WV01_20200714_10200100964C8700_102001009C699B00_2m_lsf_seg1	14-07-2020
Henrietta-Nesmith	n81w073	SETSM_s2s041_WV02_20200711_10300100A8CCC800_10300100A9BB3E00_2m_lsf_seg1	11-07-2020
Henrietta-Nesmith	n82w073	SETSM_s2s041_WV02_20200711_10300100A91BC200_10300100ABB70600_2m_lsf_seg1	11-07-2020
Henrietta-Nesmith	n82w075	SETSM_s2s041_WV02_20200715_10300100A7AA3900_10300100AA6E3E00_2m_lsf_seg1	15-07-2020
Henrietta-Nesmith	n81w074	SETSM_s2s041_WV02_20200718_10300100A92F5200_10300100A9A91D00_2m_lsf_seg1	18-07-2020
Henrietta-Nesmith	n81w074	SETSM_s2s041_WV02_20200718_10300100AA7A3E00_10300100AB434300_2m_lsf_seg1	18-07-2020
Unnamed 1	n82w074	SETSM_s2s041_WV03_20200720_104001005D6D5100_104001005F210E00_2m_lsf_seg1	20-07-2020

2.3.5 Georeferencing

Manual georeferencing was performed in QGIS for each historical air photo, utilizing the 2020 PlanetScope scenes of each glacier as the master imagery. With the exception of Unnamed 1 Glacier, which was fully covered by a single photo, all other glaciers required 2-6 photos to cover their entire surface. In such cases, the air photo which captured the glacier's terminus was initially georeferenced to its corresponding 2020 PlanetScope image. Subsequently, overlapping sections of the other air photos from that glacier were aligned to the previously georeferenced photo, while non-overlapping sections were directly aligned to the Planet imagery. This method was preferred over individual georeferencing of all photos for a single glacier to their respective Planet image, as it ensured improved alignment at the boundary of overlapping air photos. Photos that required further manipulation to enhance alignment were manually adjusted by using the "Shift" function in ArcGIS Pro, using distinctive surface features such as channels. Processing statistics of the final georeferenced products are provided in Table 4; the mean error metric reflects the average deviation between actual ground control point (GCP) positions, and their positions predicted by the georeferencing transformation.

Table 4. Georeferencing statistics for historical air photos.

Glacier	Image ID	Total GCPs	Transformation	Residual pixel range	Mean Error (m)
Unnamed 2	A16613_106	17	Polynomial 3	1.13 – 23.59	18.61
Unnamed 2	A16726_084	15	Polynomial 3	0.11 – 17.25	13.36
Unnamed 2	A16679_073	17	Polynomial 3	1.64 – 22.41	23.05
Unnamed 2	A16974_023	18	Polynomial 3	3.9 – 18.53	19.36
Unnamed 2	A16974_025	11	Polynomial 1	1.12 – 36.42	24.86
Unnamed 2	A16679_072	14	Polynomial 1	3.13 – 33.89	20.04
John Evans	A16607_193	12	Polynomial 3	0.07 – 11.21	12.23
John Evans	A16607_192	20	Polynomial 3	1.8 – 14.86	10.2
John Evans	A16616_059	14	Polynomial 3	1.81 – 16.24	16.86
Henrietta-Nesmith	A16613_035	14	Polynomial 3	0.3 – 9.79	9.05
Henrietta-Nesmith	A16679_155	22	Polynomial 3	2.93 – 28.46	23.75
Henrietta-Nesmith	A16687_069	18	Polynomial 3	1.5-12.89	10
Unnamed 1	A16708_005	11	Polynomial 3	0.067 – 6.43	8.66

2.3.6 Channel Mapping Criteria

Following the terminology of Bash and others (2023), channels were identified based on their curvilinear shape, smooth texture, and blue/white tones in the multispectral PlanetScope imagery. A curvilinear shape indicates smooth, curved outlines with few sharp angles, which suggests a natural, sinuous flow pattern typical of water channels, as opposed to more angular or irregular shapes that might represent features like crevasses. Channels also exhibited a smooth texture, characterized by homogeneous pixels with a consistent reflectance pattern across the channel length. In hillshade models, they were identified from depressions with contrasting light and dark areas on either side (Bash and others, 2023). While maintaining the same morphology as observed in multispectral imagery, Lampkin and Vanderberg (2014) also note that supraglacial channels exhibit relatively high contrast in reflectance compared to the surrounding ice in panchromatic imagery. In this context, the channels are distinguishable from the surrounding ice and snow due to their darker appearance. In this study, channel continuity also served as a mapping criterion whereby features characterized by repetitive breaks along their total length were excluded as they could not be mapped with high confidence.

Once mapped, the final channel polylines were classified according to a channel classification terminology similar to that of St. Germain and Moorman (2019), categorizing supraglacial streams and rivers into three main classes: surface, incised, and canyons (Figure 2). Surface streams are identified by a valley depth-to-width ratio of less than 1. If a channel lacks a continuous depression along its course in the hillshade model, but remains visible in the Planet image, it is classified as a surface stream (Figure 3). This assessment considers the lack of a clearly identifiable channel depression in the 2 m DEM, indicating a relatively shallow valley, while acknowledging its visibility in the 3 m PlanetScope image, suggesting that the width of the valley exceeds its depth.

Since no hillshade model is available to support the mapping of hydrological systems in 1959, a different approach was used to identify surface streams in the historical air photos. This approach relied on both the elements of image interpretation (Bash and others, 2022) and the notion that channel width and depth are positively correlated (St. Germain and Moorman, 2019). First, the average channel width beyond which continuous depressions are no longer discernible

in the 2020 hillshade model was calculated for all glaciers using the 'Measure Line' tool in QGIS. This average width was found to be ~6 m, or 2 pixels in the PlanetScope images. Channels of this width were then examined in the historical air photos, and those without clearly defined channel banks were classified as surface streams. Well-defined channel banks suggest an incised feature where the valley depth-to-width ratio would likely be more than 1, indicating that the channel is not of surface nature.

In contrast to surface streams, canyons are readily discernible in both satellite imagery and aerial photos due to their substantial size and perennial presence. These are characterized as large deeply incised channels, where flowing water typically occupies only a small percentage of the valley volume (Figure 3). They also have well defined banks, large enough to be considered as walls, which often cast shadows over a portion of their respective channel in satellite imagery. These channels usually form at lower elevations as meltwater flows towards the terminus and becomes more channelized.

All other mapped channels, not classified as canyons or surface streams, were categorized as incised rivers. These channels generally exhibit high and low reflectivity on either of their sides, indicating the presence of well-defined banks, and are clearly observed as continuous features in the hillshade model (Figure 3). They possess deeper valleys than surface streams but are narrower than canyons. All steps involved in the mapping process are summarized in Figure 2.

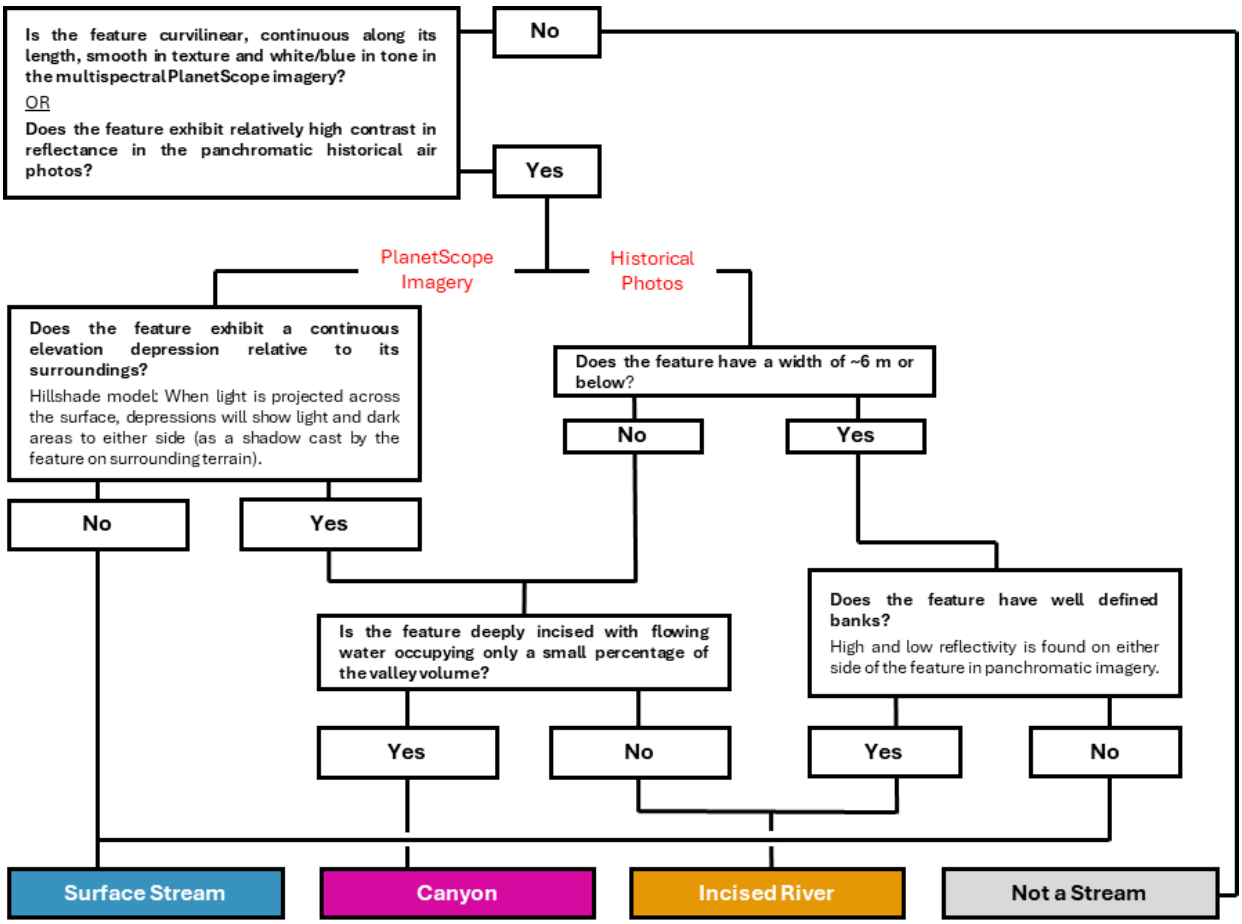

Figure 2. Decision tree for classifying channel model polylines. Sections of the channel network are examined, and channels are classified as surface, incised or canyon channels.

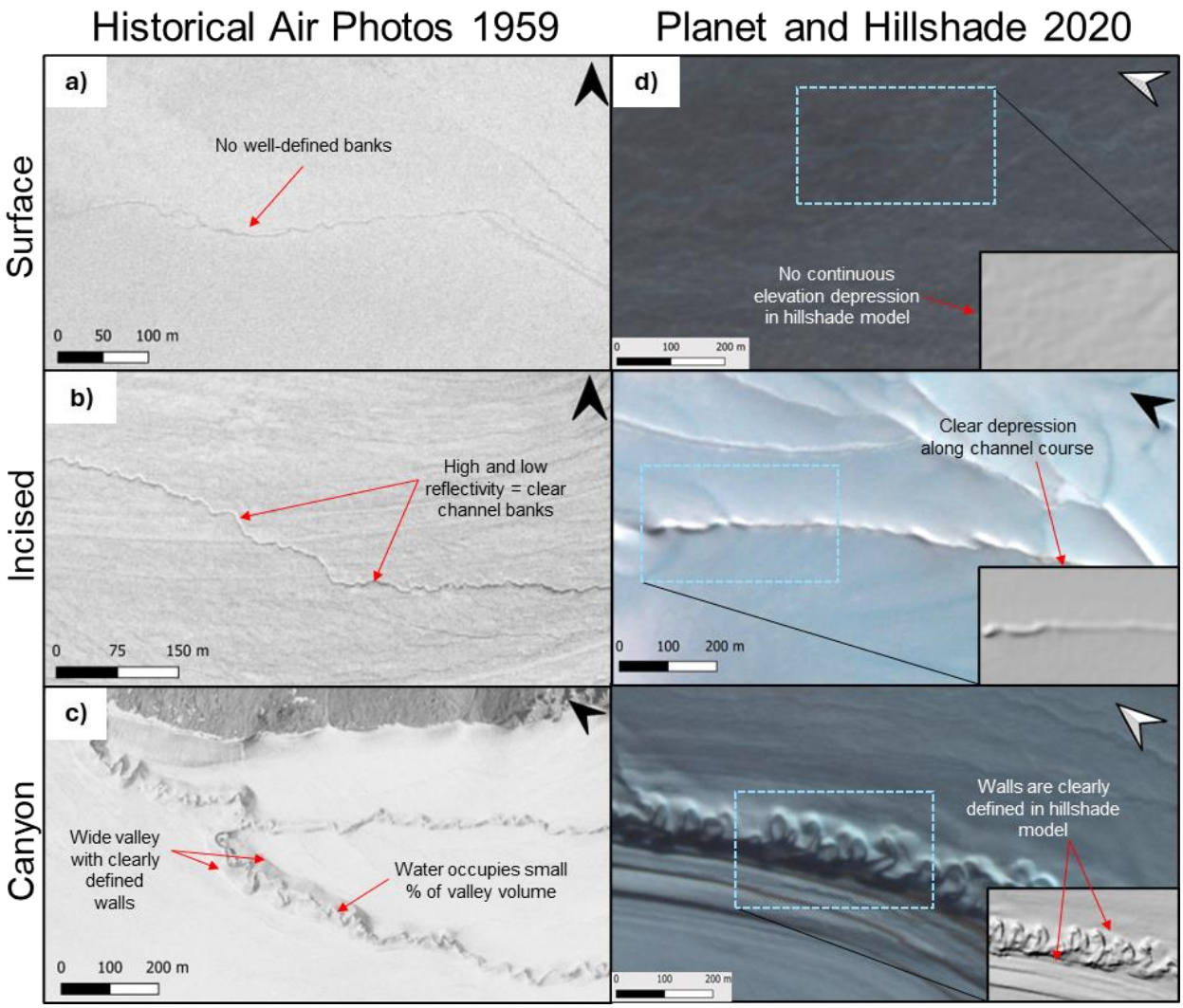

Figure 3. Surface, incised, and canyon channels as they appear in the 1959 historical air photos and 2020 PlanetScope imagery, along with a comparison of the same channels in the hillshade model (inset).

2.3.7 Hydraulic Geometry Quantification

Several components of hydraulic geometry are derived from the final stream polylines: total channel length, proportions of total length for each channel class, sinuosity, and drainage density (D_d). D_d standardizes the distribution of stream networks relative to the area of interest, making it a valuable tool for comparing different supraglacial networks on glaciers with varying surface areas, as well as the abundance of channels at different elevations. Proportions of total length are also valuable, as they highlight the distributions of different channel types without accounting for changes in channel length, enabling comparisons between different years.

The total D_d was computed by dividing the total channel length by the area of the glacier, while the total D_d by channel class was calculated by dividing the total length of channels per class by the total surface area of the glacier. The surface area of each glacier for 2020 was calculated using outlines acquired from the Randolph Glacier Inventory v 7, which were subsequently manually checked and corrected at the glacier margin and drainage divides using the same ArcticDEM strips used to create the hillshade models (Table 3). These strips were clipped to match the extent of each glacier outline, after which elevation polygons were generated at 100 m increments. This process was repeated for the 1959 air photos by also using the 2020 ArcticDEM strips as it was not possible to generate DEMs for every glacier from the photos, and attempts resulted in large data gaps in snow covered regions where images were overexposed. While the 2020 DEMs may not represent the 1959 surface perfectly, they allow for consistency when comparing the maps from each year. D_d by elevation was then computed by dividing the total channel length within each 100 m elevation band by the total area of the respective band, a process which was also replicated for each channel class.

Sinuosity, defined as the ratio of stream length to straight-line distance, was calculated for the canyon rivers on each of the studied glaciers (incised and surface channels were excluded from this analysis due to their narrower stream width and less permanent presence, which made them challenging to consistently map). The straight-line distance was drawn carefully following the centerline of each valley (defined as the distance between the two channel banks/walls) for all canyons in order to follow changes in the channel's direction representing different reaches of the channel. Based on the sinuosity ratios, canyons were classified as straight, sinuous, or meandering, with specific thresholds for each classification (<1.1 for straight, 1.1 - 1.5 for sinuous, and >1.5 for meandering) (Kusratmoko, 2019).

The overall mean sinuosity for each glacier was then computed using a weighted method to ensure that the sinuosity measure accurately reflected the contribution of each canyon relative to its length, providing a more precise representation of the overall stream sinuosity on the glacier. The total stream length (L_{total}) was determined by summing the lengths of all canyon rivers for each glacier. The weighted average sinuosity ($W.S_{\text{total}}$) was then computed using the formula:

$$\frac{\sum_{i=1}^{n}(S_i \times L_i)}{L_{total}} \quad (1)$$

Where S_i is the sinuosity of river i, L_i is the length of river i, and L_{total} is the total length of canyons on the glacier. Using a similar formula, the weighted variance, weighted standard deviation (SD), and weighted skewness were also calculated. Additional statistics were calculated to create a box plot, including the median, quartiles, interquartile range, whiskers, and outliers. The Mann-Whitney U test, which compares two independent samples to assess whether their population distributions differ, was performed on these values to determine if changes between years are significant. This test was chosen because it is a non-parametric test and is suitable for comparing distributions of different sample sizes. The significance level for all statistical analyses in this study is set at alpha 0.05. Together, these metrics provide a clearer understanding of changes in the distribution of sinuosity values and differences among glaciers.

2.3.8 Moulins and Sink Points

Moulins are crucial components of the supraglacial hydrological system, facilitating the transfer of water to the englacial and subglacial systems while altering surface flow paths on the glacier. Their formation usually requires substantial water input at a consistent location, meaning that they are typically connected with active perennial supraglacial channels. These vertical or near-vertical conduits are often found in association with crevasses, faults, and drainage from lakes, where water flow or structural weaknesses can create pathways through the ice (Phillips and others, 2013; Bash and others, 2022).

Similarly, crevasses often interrupt supraglacial drainage pathways when supraglacial channels flow into them. Hydrologically connected crevasses can alter stream pathways, becoming part of the surface drainage network and transporting water along their fracture line (St. Germain and Moorman, 2019). In other scenarios, crevasses can function as depressions, storing water and/or transferring it to the englacial system. They frequently serve as starting points for the formation of moulins as well (Bash and others, 2022).

Due to the challenge of identifying moulins in satellite imagery and aerial photographs, potential moulins and crevasses are both referred to as sink points in this study. Only when absolutely certain of their origin are moulins and crevasses explicitly named as such in the text.

These sink points were manually identified as the abrupt termination of rivers in both the 1959 air photos and the 2020 PlanetScope imagery. Due to the higher spatial resolution of the historical air photos, moulins could often be directly identified as rounded features with a differing tone compared to their surroundings. This was not possible in the PlanetScope imagery. Therefore, manual validation was undertaken on two of the four glaciers with the help of two panchromatic 0.5 m resolution WV2 images, and one WV3 image, covering the ablation area of Unnamed 2 and the entirety of Unnamed 1 Glacier (Table 2).

2.4. Results

Below are the results of both the qualitative and quantitative analyses. The findings are structured to first provide a qualitative overview of the multi-decadal changes in the supraglacial drainage networks across all five studied glaciers (section 2.4.1), followed by a description of current drainage patterns for the four mapped glaciers (section 2.4.2). The evolution of each mapped system is then quantified by comparing the 2020 results with those from 1959 (section 2.4.3).

2.4.1 Multi-Decadal Changes

The time series analysis reveals substantial changes in the supraglacial hydrological networks of the studied glaciers over the past ~60 years, with trends indicating a recent shift towards more established perennial systems. These changes are observed in various aspects such as the number, length, width, incision, and sinuosity of the channels, with some changes seemingly accelerating in the last decade. Additionally, some channels have extended further upglacier during this period.

John Evans Glacier exemplifies many of these changes. For instance, a new perennial river formed in the northern part of the ablation area of the glacier between 1959 and 1987 (Figure 4b and 4c). Channels have also lengthened over time, such as one channel which extended from the upper ablation area to lower elevations, connecting the upper supraglacial system with the system located in the terminus region (dots in Figure 4c and 4f). This channel extended by 0.27 km between 1959 and 1987, barely extended between 1987 and 2002, extended by 0.47 km

between 2002 and 2011, and eventually reached the downstream system sometime between 2011 and 2020. Channel banks also seem to have widened over time, especially on the larger canyon rivers, and larger rivers have increased in importance into the southern portion of the accumulation area, especially since the early 2010s.

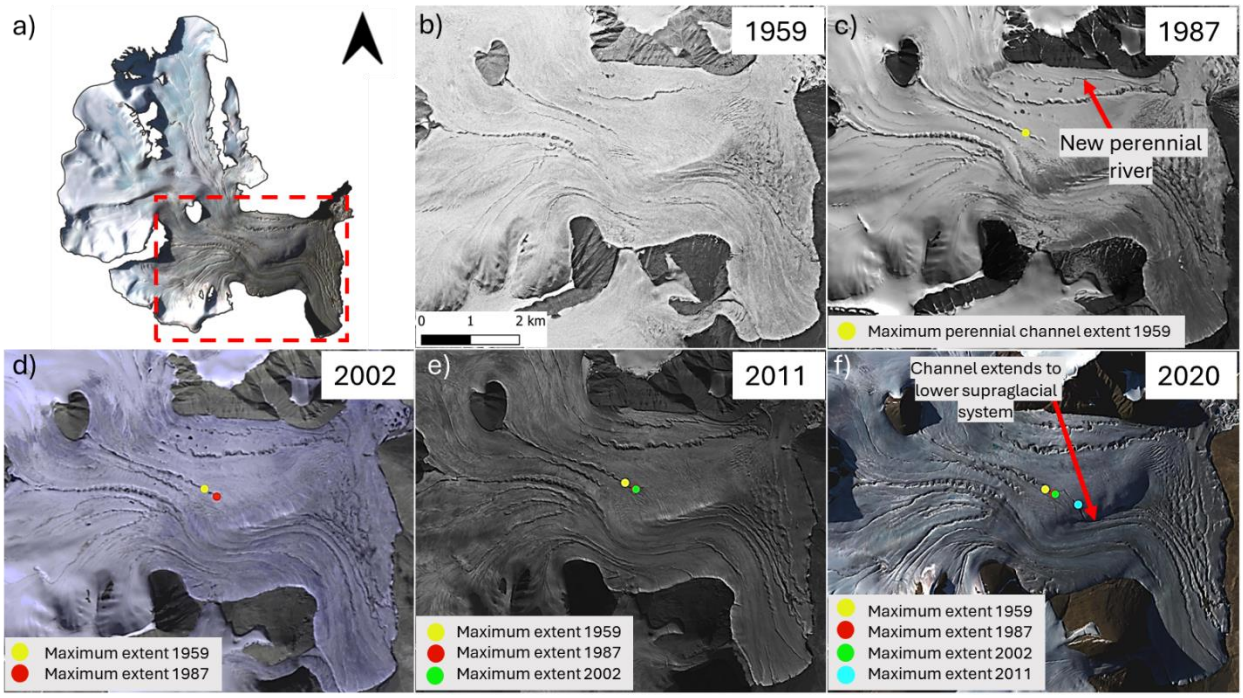

Figure 4. Channel evolution on John Evans Glacier between 1959 and 2020. a) overview of the glacier, with the ablation area shown in parts b-f outlined by the red box. b) ~0.6 m resolution historical air photo, c) 20 m resolution SPOT-1 image, d) 15 m resolution ASTER image, e) 5 m resolution SPOT-5 image, f) 3 m resolution PlanetScope image. Coloured dots show downglacier progression of a channel over time. See Tables 1 and 2 for image dates.

Elsewhere, Unnamed 2 Glacier has undergone marked changes in its supraglacial drainage network over time, particularly in channel sinuosity near its terminus, where larger meanders have formed and eventually cut through their necks, showing signs of important channel dynamism. As a result, channel banks have widened considerably (Appendix, Figure 1-A). On Henrietta-Nesmith Glacier, channel dynamism is also observed within older larger perennial canyons. These large rivers have also extended up glacier and numerous new perennial channels have emerged near and within the terminus region (Appendix, Figure 2-A). In far northern areas, such as on Unnamed 1 Glacier, incision changes have become more prominent across most of the glacier, especially over the past decade (Figure 5).

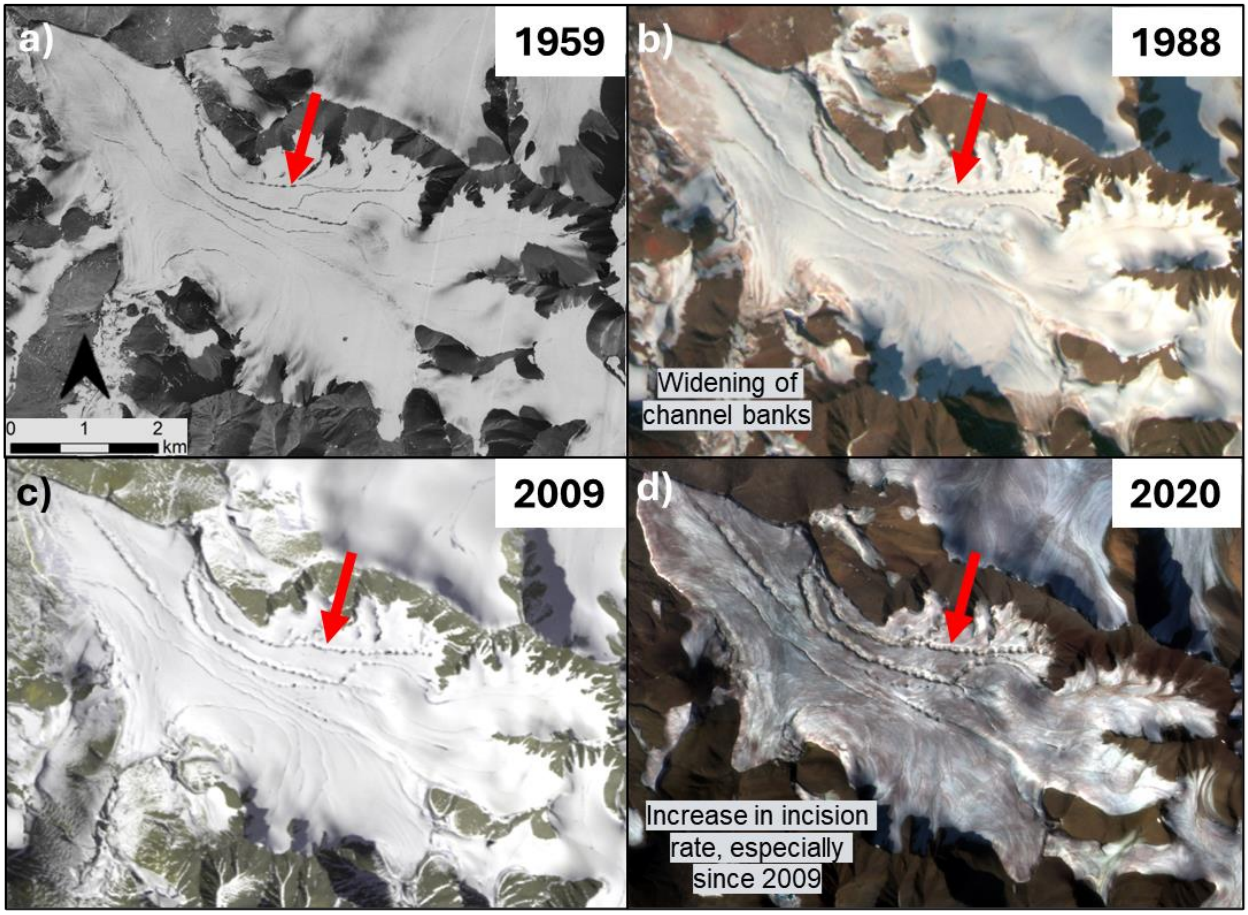

Figure 5. Channel evolution on Unnamed 1 Glacier between 1959 and 2020. a) ~4 m resolution historical air photo, b) 20 m resolution SPOT-1 image, c) 15 m resolution ASTER image, d) 3 m resolution PlanetScope image. The red arrow tracks the evolution of a canyon river which has seen particularly important changes in width and incision between 1959 and 2020, with an increase in incision rate over the last decade. See Tables 1 and 2 for image dates.

In contrast to the other glaciers, the supraglacial hydrology of Sydkap Glacier has exhibited a different temporal evolution. A large crevasse field dominates the terminus area and extends ~7.5 km up glacier, inhibiting the formation of perennial hydrological systems (Figure 6b). Further up glacier, channels have remained poorly defined throughout the study period, indicating that they may change their course frequently (Figure 6c and 6d). Only near the equilibrium line and within the accumulation area are larger channels found, but these disappear relatively quickly as they progress down glacier, potentially terminating in moulins, crevasses or smaller distributed systems (Figure 6d).

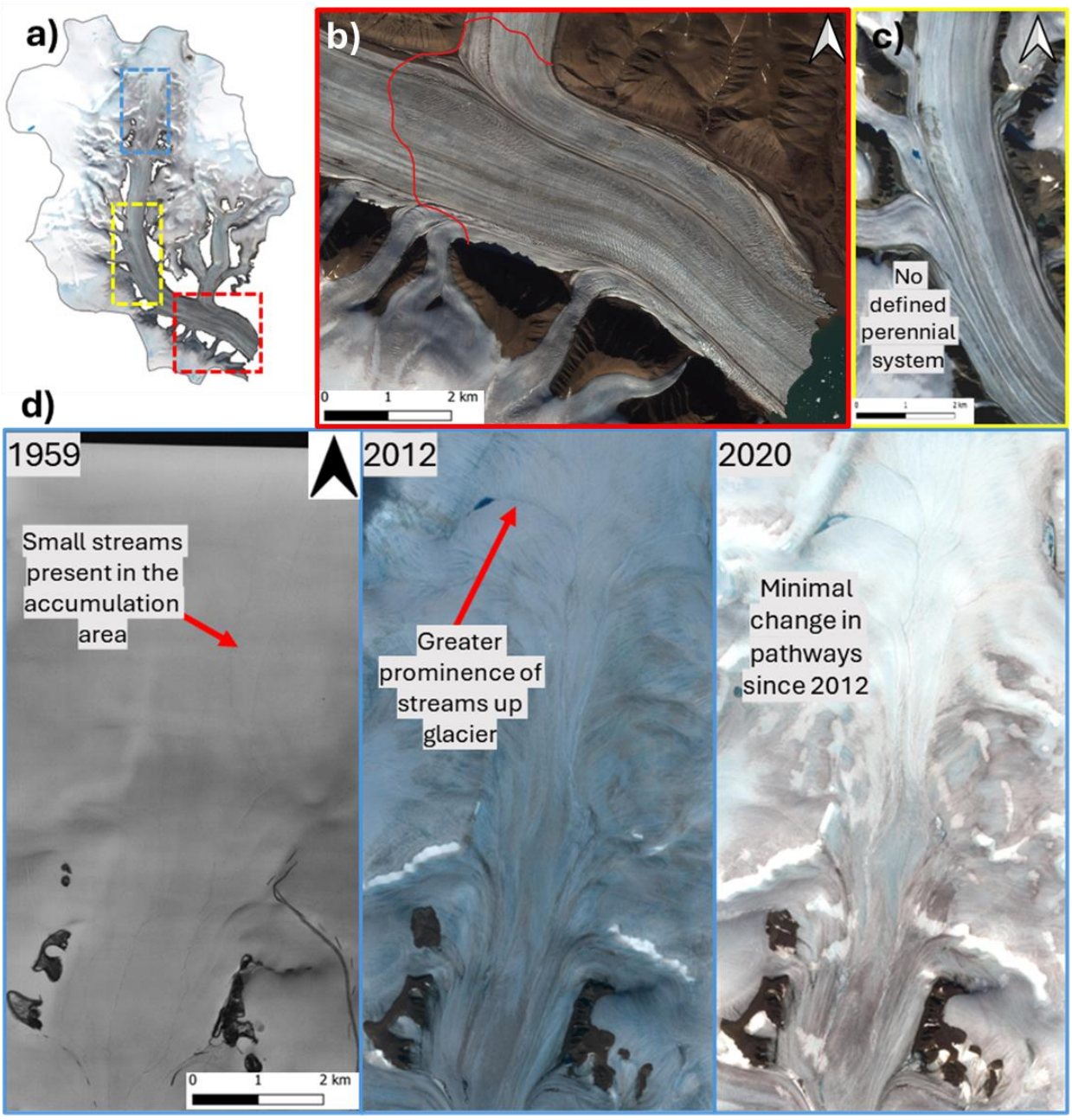

Figure 6. a) PlanetScope image of Sydkap Glacier from August 10, 2020, showing the lack of perennial supraglacial system, b) close up of a) showing the upper limit of the crevasse field (red line), which inhibits the uninterrupted transport of meltwater across the surface for ~7.5 km from the terminus. c) close up of a) showing further up glacier, where even without the presence of crevasses, supraglacial channels are limited. d) Channel evolution into the accumulation area of Sydkap Glacier from 1959 to 2020. 1959) ~4 m resolution historical air photo, 2012) 10 m resolution SPOT-5 image, 2020) 10 m resolution Sentinel-2 image. See Tables 1 and 2 for image dates.

2.4.2 Contemporary Drainage Patterns

The 2020 mapping of the supraglacial hydrological systems of the four selected glaciers (excluding Sydkap Glacier) reveals diverse drainage patterns within each glacier and between different glaciers. In addition, the distribution and abundance of channels of different class also differs from one glacier to another. Below, a description of the contemporary drainage pattern is provided for each mapped glacier, as well as their distribution of sinks. The relative distribution per channel class as a proportion of their total length with elevation is also discussed, along with the D_d per channel class as a function of elevation. While D_d measures channel length per unit area for each elevation band, the proportion of total channel length per class does not account for the size of each band and instead demonstrates the raw contribution of each band to the total length of the channel network. This remains an important indicator of how channel distribution changes over time.

Sydkap Glacier was excluded from this analysis due to its lack of perennial supraglacial rivers that could be consistently identified.

2.4.2.1 Unnamed 2 Glacier

On Unnamed 2 Glacier, a total of 479.95 km of channels were mapped in 2020, corresponding to a total D_d of 1.98 km/km^2, the lowest D_d among all analyzed glaciers (Figure 7a). Of the total channel length, canyons account for 3.8%, while incised rivers and surface streams constitute 52.9% and 42.1%, respectively (Figure 7a). 84.7% of the supraglacial system develops below the ELA, which is positioned at 1045 ± 50 m a.s.l. While 90% of the total canyon length is concentrated near the terminus between the 100 and 200 m bands, incised and surface channels show a more even distribution across most of the ablation area (between the 200 and 900 m bands) (Figure 8d). The highest elevation at which channels were mapped was ~1426 m.

In the westernmost (upper) part of the accumulation area, supraglacial channels are not clearly channelized, instead forming a broad dendritic drainage pattern mostly composed of incised rivers. While a limited number of short, incised channels rapidly terminate in crevasses or sinks in this region, all other channels converge into fewer, more well-defined rivers at ~1030 m, creating a parallel drainage system. Between ~830 m and 950 m, the supraglacial system becomes less channelized again as surface streams become more abundant over incised rivers in the 800

m band (Figure 8h), forming braided networks, with some rivers carrying water off the northern margin of the glacier. Channels that continue down glacier become evenly distributed near 800 m elevation, before terminating in a series of moulins or crevasses forming a line near the 740 m mark (Figure 7b).

In the central region of the glacier, between elevations of 500 and 700 m, supraglacial channels reappear in a parallel system, with some rivers flowing off the northern margin of the glacier while others adopt a semi-rectangular pattern as they flow through a large supraglacial lake. In this section of the ablation area, surface and incised channels alternate in abundance as their D_d progressively increases downglacier (Figure 8h). As water becomes channelized again near the 475 m elevation mark, numerous small surface streams coalesce forming larger parallel rivers with both channels classes eventually reaching their peak D_d in the 300 m band (Figure 8h). Beyond this point, larger rivers develop into highly sinuous canyons towards the glacier terminus where canyon rivers become most abundant (higher D_d) over the other two channel classes in the 100 m band (Figure 8h). These canyon rivers are fed by multiple tributary systems of sub-parallel channels, mostly composed of surface streams (Figure 7c). Channels which do not terminate in moulins or crevasses in the southern portion of the accumulation area eventually join the main supraglacial drainage system along the glacier's main trunk, delivering water from higher elevations toward the glacier terminus.

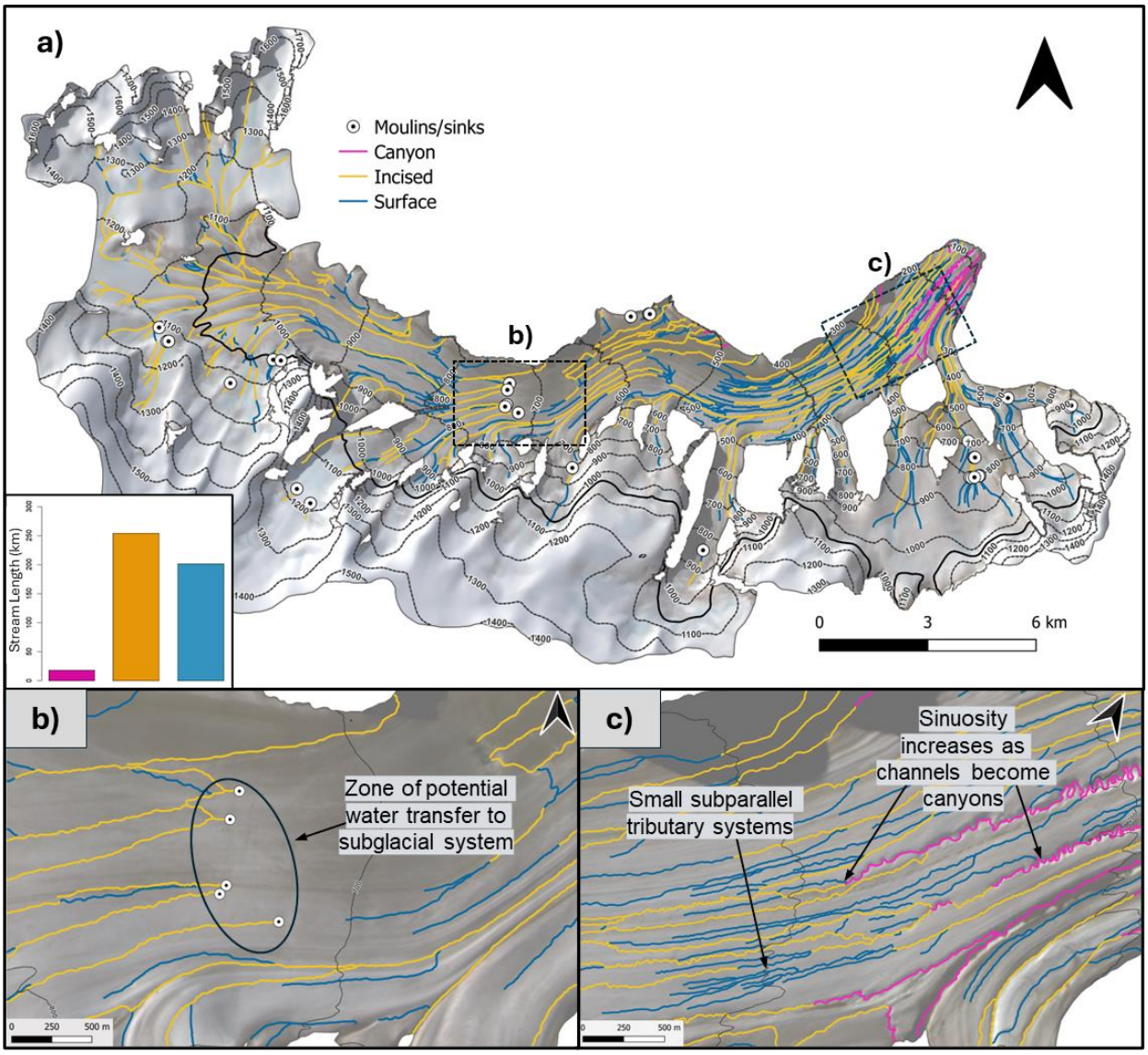

Figure 7. Canyon, incised, and surface channels on Unnamed 2 Glacier, along with moulins and sink areas delineated on PlanetScope images from July 23, 2020. (a) Overall drainage pattern across the entire glacier surface, (b) an area where water may reach the subglacial system, and (c) drainage pattern near the terminus, where smaller sub-parallel streams exist alongside larger rivers and canyons. The solid black line in a) represents the 2020 ELA at 1045 ± 50 m a.s.l. and the inset shows the total stream length (km) for each stream class.

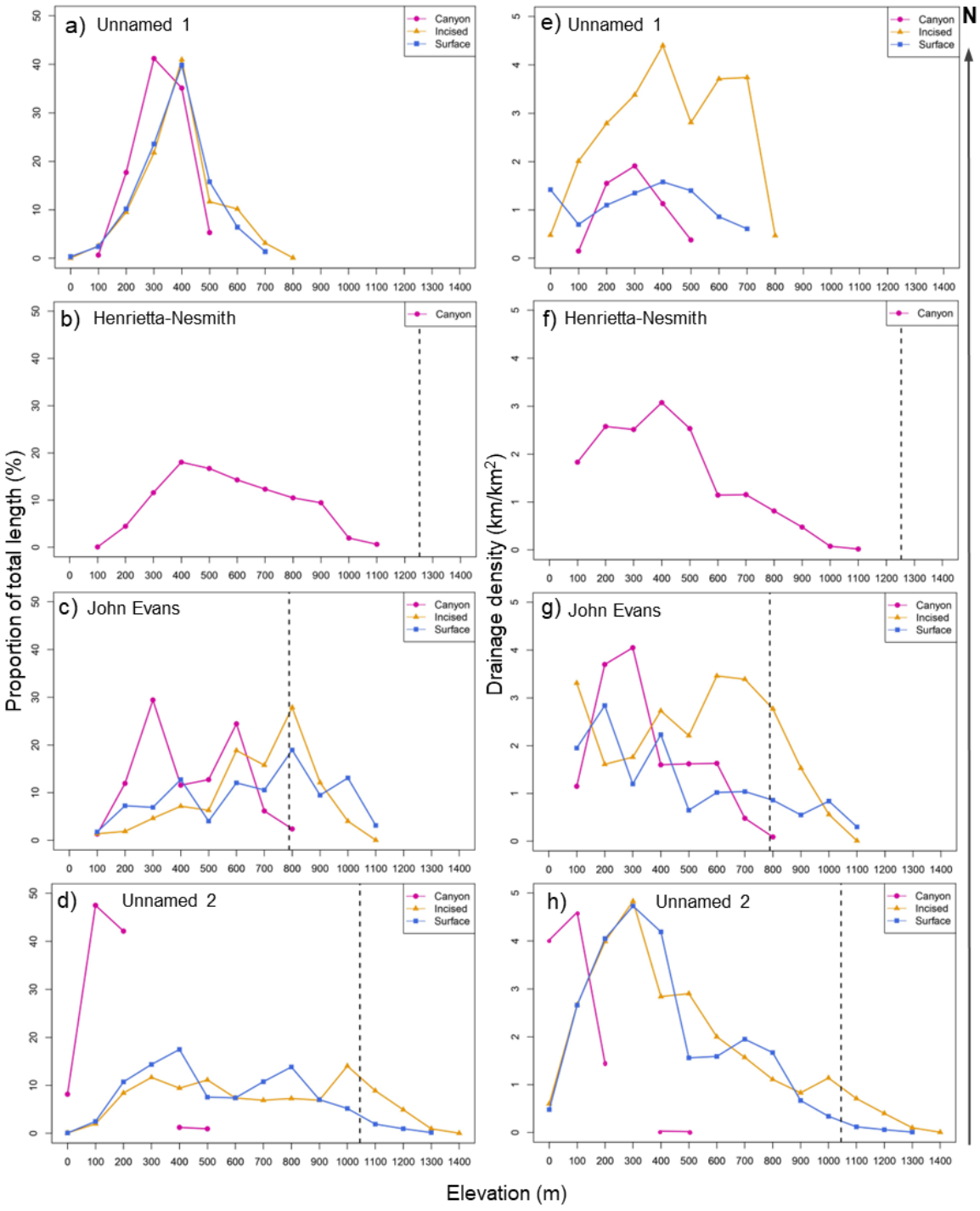

Figure 8. Proportion of total length (%) by class as a function of elevation (a-d) and drainage density (e-h) as a function of elevation for the four studied glaciers in 2020. Graphs are organized by latitude based on the location of each glacier: (a and e) Unnamed 1 (82.998°N); (b and f) Henrietta-Nesmith (81.857°N); (c and g) John Evans (79.650°N); and (d and h) Unnamed 2 (78.793°N). Elevation is capped at 1400 m, which represents the highest elevation band at which channels were mapped. The black dotted line shows the position of the 2020 ELA.

2.4.2.2 John Evans Glacier

A total of 282.72 km of channels were mapped on John Evans Glacier, with streams extending up to ~1184 m in elevation (Figure 9). Incised rivers are the most abundant, representing 54.9% of the total channel length. This is followed by surface and canyon channels, which constitute 25.2% and 19.9% of the total channel length, respectively (Figure 9). Compared to Unnamed 2, a greater proportion of the supraglacial system develops above the ELA positioned at 789 ± 52 m a.s.l., although the majority (62.5%) of the system is still found in the ablation area. Despite having a smaller total channel length compared to Unnamed 2 Glacier, channels on John Evans Glacier are more widespread, extending well into the accumulation area. This widespread distribution, combined with the smaller surface area of the glacier, results in an increased D_d of 3.57 km/km². Unlike Unnamed 2 Glacier, where the majority of canyon length is concentrated near the terminus, on John Evans Glacier 90% of the total canyon length is more widely distributed between the 200 and 600 m elevation bands (Figure 8c). The relative distribution of incised and surface channels shows them increasing upglacier with both channel classes peaking in their total length in the 800 m band (Figure 8c).

In the high-elevation regions of the northern, western, and eastern sectors of the accumulation area, supraglacial channels typically exhibit a broad dendritic pattern (Figure 9), where surface streams dominate in abundance beyond the 900 m band (Figure 8g). In contrast, those in the southernmost part generally follow a more sub-parallel arrangement beginning in the 800 m band and are composed mostly of incised rivers. Despite a few sink regions in the southern accumulation area that inhibit smaller channels from progressing down-glacier, this section, along with the northern and eastern sectors of the accumulation area, remains well integrated into the downstream system. This system is largely composed of incised rivers which coalesce into fewer larger parallel ones, aligning with the general glacier flow direction, with some deepening into canyons between ~760 and 930 m elevation. In contrast, in the higher elevation areas of the central western accumulation area, channels all terminate in sinks before new channels develop near 930 m elevation, creating a disconnect between higher elevation regions and the downstream system.

As elevation approaches 750 m, near the equilibrium line, the number of highly sinuous canyons increases, with some terminating in a series of moulins near 600 m elevation. Although incised rivers remain dominant over canyons at this elevation, canyons dominate in D_d over surface streams (Figure 8g). Smaller incised rivers that continue descending down-glacier become connected with an independent system towards the terminus, primarily consisting of canyons parallel to glacier flow, where canyon D_d sharply increases into the 300 m band. Canyons are most abundant over the other channel classes near the terminus within the 200 and 300 m bands and eventually flow off the glacier's surface near or at the terminus (Figure 8g).

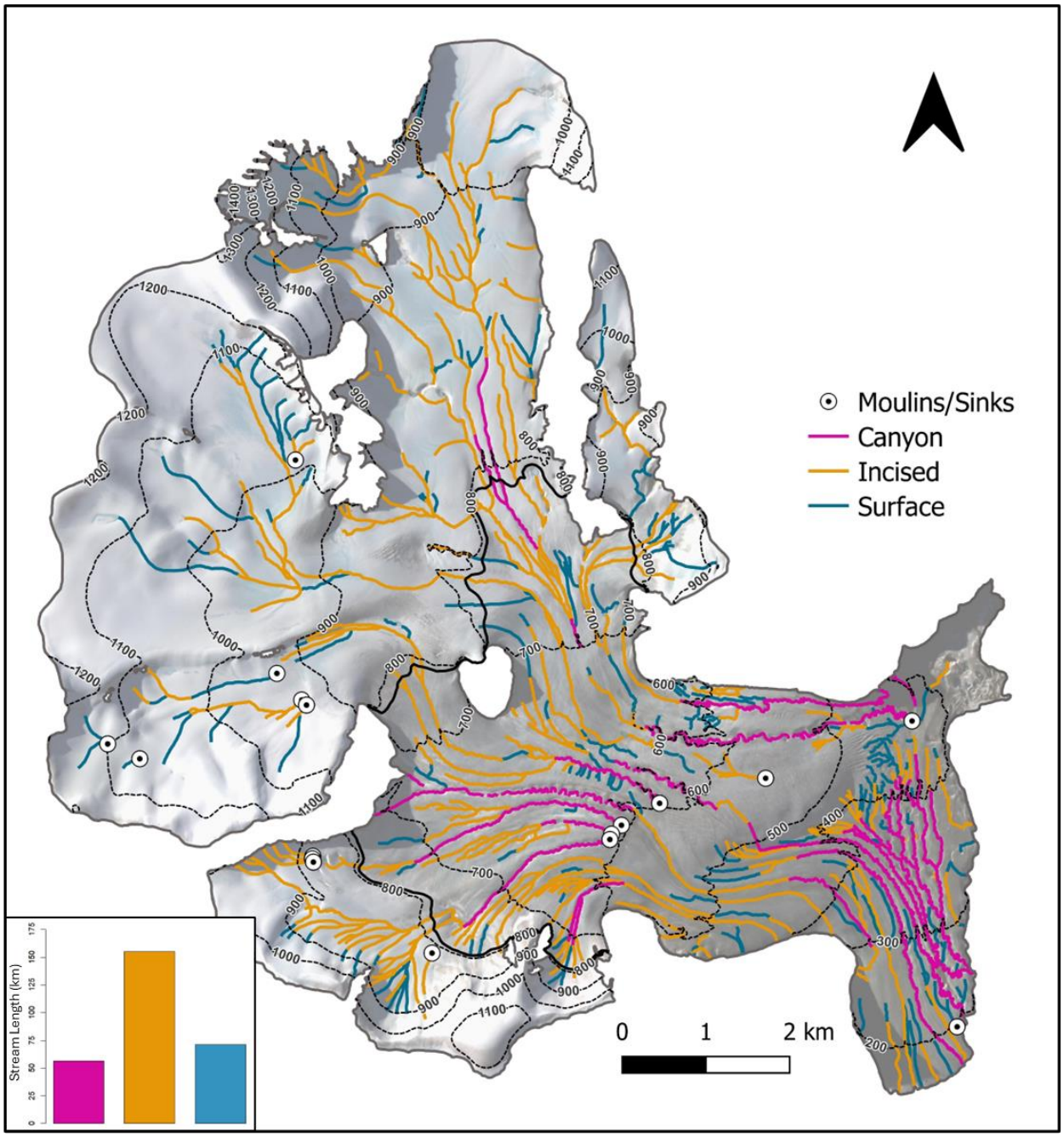

Figure 9. Canyon, incised and surface channels on John Evans Glacier, along with moulins and sink areas delineated on PlanetScope images from July 23, 2020. The solid black line represents the 2020 ELA at 789 ± 52 m a.s.l. and the inset shows the total stream length (km) for each stream class.

2.4.2.3 Henrietta-Nesmith Glacier

Due to time restrictions and the poor quality of some historical air photographs, particularly those taken further up glacier (overexposed), only canyon rivers were mapped in both

1959 and 2020 on Henrietta-Nesmith. Despite this, the highest canyon river length of 127.52 km was mapped on this glacier, the largest glacier in the study area. Similar to the two previously described glaciers, these rivers gain importance further down-glacier below the ELA (1253 ± 77 m a.s.l.) as they form a large parallel system of highly sinuous rivers, with some terminating in sinks near the western glacier margin, while others flow off the glacier surface near or at the terminus (Figure 10). In contrast to the two previous glaciers, canyons on Henrietta-Nesmith Glacier exhibit a more even distribution, increasing steadily from the 100 to 300 m elevation bands before reaching a peak in the 400 m band, which also corresponds to the peak in D_d (Figure 8b and 8f). There is a gradual decrease in the proportion of total length of canyons up to the 900 m band, followed by a sharper decline beyond this point (Figure 8b). D_d values of canyons on this glacier remain higher than those observed on other glaciers above 700 m elevation (Figure 8e-h).

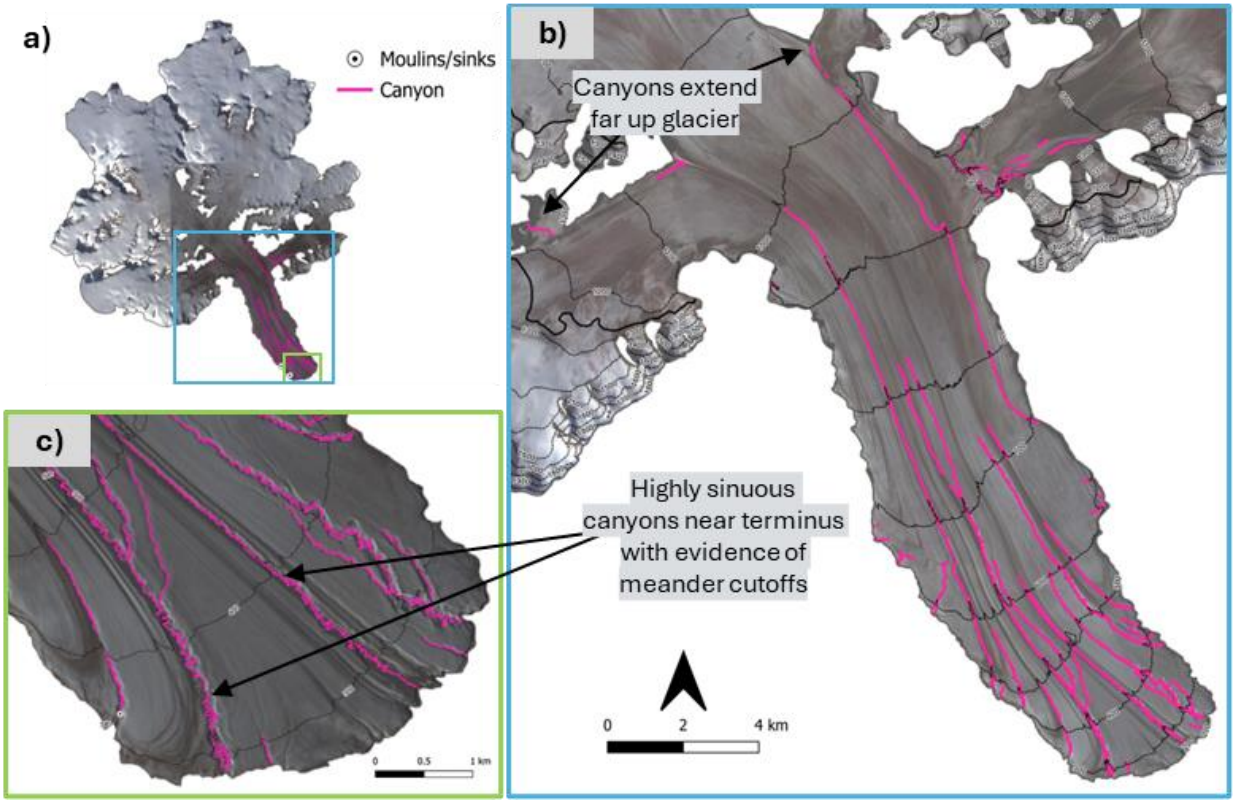

Figure 10. Canyon rivers on Henrietta-Nesmith Glacier along with hydrologically significant moulins/sinks delineated on PlanetScope images from July 24, 2020. (a) Overview of the glacier, (b) drainage pattern of canyon rivers located down glacier, (c) sinuosity patterns of canyons near the glacier terminus, highlighting important channel dynamism through evidence of meander cutoffs. The solid black line in b) represents the 2020 ELA at 1253 ± 77 m a.s.l.

2.4.2.4 Unnamed 1 Glacier

Unnamed 1 Glacier exhibits the highest D_d among all mapped glaciers, reaching 5.84 km/km^2, with extensively developed supraglacial networks covering the majority of its surface area which is now entirely positioned below the ELA (Figure 11). A total channel length of 105.68 km was mapped on this glacier, with channels extending up to ~820 m of elevation. The distribution of channel lengths across different classes relative to the total channel length is similar to Unnamed 2 and John Evans Glacier, with canyons, incised and surface channels representing 17.9%, 60% and 22.1% of the total channel length respectively (Figure 11). While ~75% of the total canyon length is concentrated between the 300 and 400 m bands, and peaking in the 300 m band, ~75% of the total incised and surface lengths are more spread out between the 300 and 500 m bands with peaks in both channel classes in the 400 m band (Figure 18a).

Similar to Unnamed 2 and John Evans Glacier, supraglacial channels at high elevations exhibit a predominantly dendritic pattern (Figure 11). As these channels progress down glacier, smaller rivers transition into sub-parallel configurations before joining larger entrenched rivers, which eventually become canyons flowing parallel to the glacier's direction of flow with the greatest canyon D_d found in the 300 and 400 m bands (Figure 8e). These canyons either flow off the glacier surface at margins in the 200 m band or become less incised, transforming into incised rivers or surface streams with one channel terminating in a moulin at ~167 m elevation near the terminus. While larger channelized incised and canyon rivers adopt a parallel pattern starting at ~450 m elevation, smaller systems, primarily composed of canyon tributaries of incised and surface streams, display dendritic and sub-parallel patterns adjacent to the central system. Similar systems are also observed near the glacier margins in the lower half of the glacier, disconnected from the larger parallel system and not fed by rivers originating at higher elevations. Disconnected systems also form at drainage divides, composed of only surface and incised channels. Unlike the other glaciers, incised rivers dominate across most elevations over the other channel classes even in elevations bands where canyons are most abundant (Figure 8e).

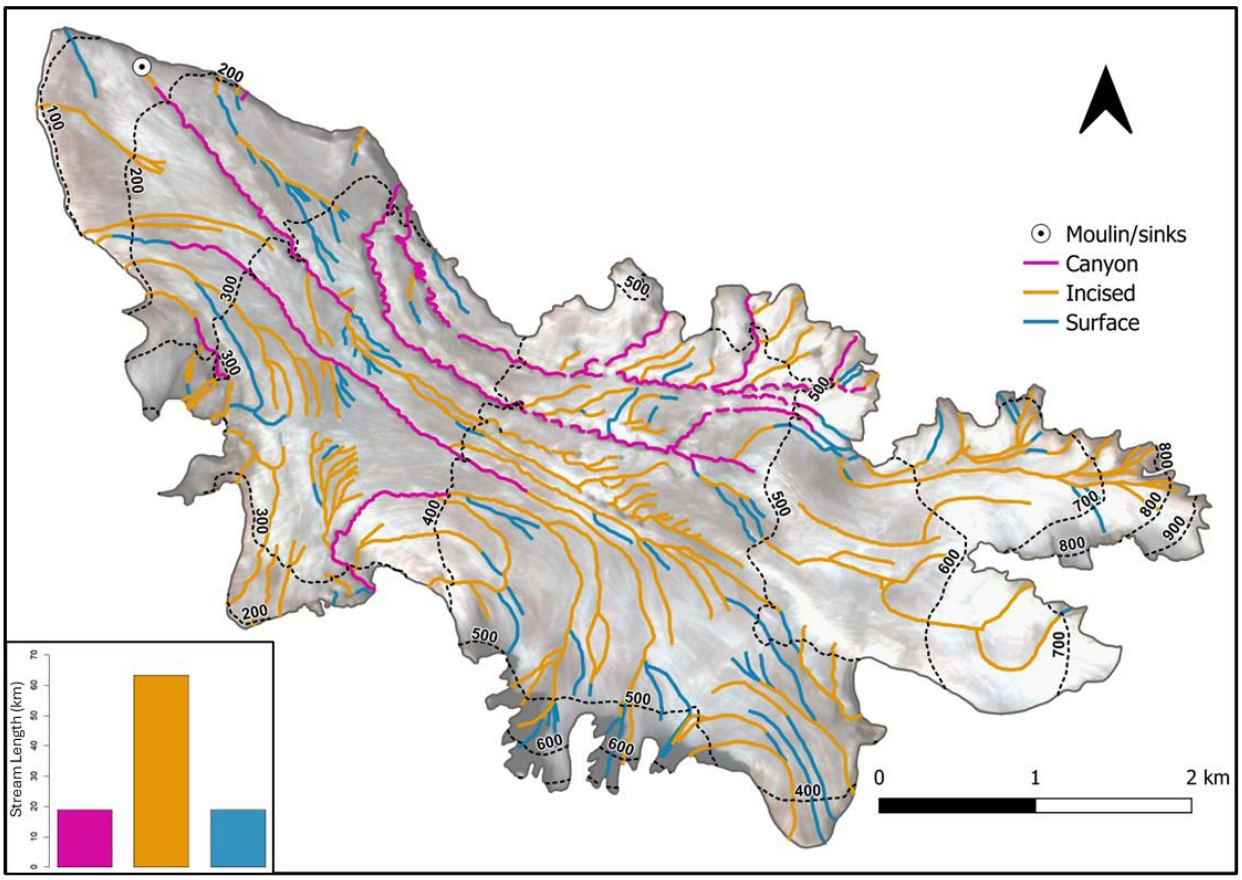

Figure 11. Canyon, incised and surface channels on Unnamed 1 Glacier, along with moulins and sink areas delineated on PlanetScope images from July 23, 2020. No ELA is labelled as the contemporary ELA is above the highest elevation of the glacier. The inset shows the total stream length (km) for each stream class.

2.4.3 Changes in Supraglacial Hydrological Systems Between 1959 and 2020

In this section the evolution of the supraglacial hydrological systems of the four mapped glaciers between 1959 and 2020 is analyzed and quantified by observing changes in overall drainage patterns, the length of supraglacial channels, the distribution of channels with elevation, and D_d by elevation. Over this ~60-year period, both total channel length and total D_d increased on all glaciers. In 1959, Unnamed 2 and John Evans Glacier had total channel lengths of 348.57 km and 203.24 km, respectively, which increased by 37.7% and 39.1% by 2020. While the total channel length of 98.59 km in 1959 also increased on Unnamed 1 Glacier, situated furthest north, the increase was much smaller, increasing by only 7.2%. As a result, D_d increased by 43.9%, 45.7% and 14.4% for these 3 glaciers respectively (Figure 12d).

The relative proportion of each channel class has also changed across all glaciers, wherein canyons and incised rivers have grown in significance as contributors to the total channel length between 1959 and 2020, while the importance of surface streams has diminished (Figure 12a-c). In 1959 surface streams comprised the largest portion of each glacier, contributing 78.3%, 60.3%, and 56.8% to the total length of Unnamed 2, John Evans, and Unnamed 1 glaciers, respectively. By 2020, however, incised rivers had become much more important, with surface streams now accounting for only 42.1%, 25.2%, and 22.1% of the total length for these glaciers. As for canyons, they accounted only for 1.6%, 15.8% and 17% of total length in 1959, respectively, increasing to 3.8%, 19.9% and 17.9% by 2020.

While the overall trend of changing channel types is clear on all three glaciers, the contribution of each stream class to the total length and, consequently, total D_d varies considerably from one glacier to another (Figure 12d). On Unnamed 2 Glacier, the total length of canyons more than tripled from 5.74 km to 18.31 km between 1959 and 2020 (Figure 12a). However, the contribution of canyons to the total length and overall D_d remains small compared to Unnamed 1 Glacier, where canyon contributions are substantially larger despite minimal increases in their length (Figure 12c). Similarly, the length of incised rivers on Unnamed 2 increased by 263%, whereas on Unnamed 1 the increase was 145.5%. Nonetheless, incised rivers remain notably more important to the total channel length and overall D_d on Unnamed 1 Glacier compared to Unnamed 2 Glacier. While the rate of change in total canyon length on John Evans Glacier falls between that of Unnamed 2 and Unnamed 1, canyons have become slightly more important to the total channel length and, consequently, to total D_d on this glacier compared to Unnamed 1 (Figure 12b). Nevertheless, the contribution of all rivers (canyons and incised rivers) remains slightly more prominent on Unnamed 1 Glacier over the study period. Overall, the total D_d has also remained the smallest on Unnamed 2 and the largest on Unnamed 1 (Figure 12d).

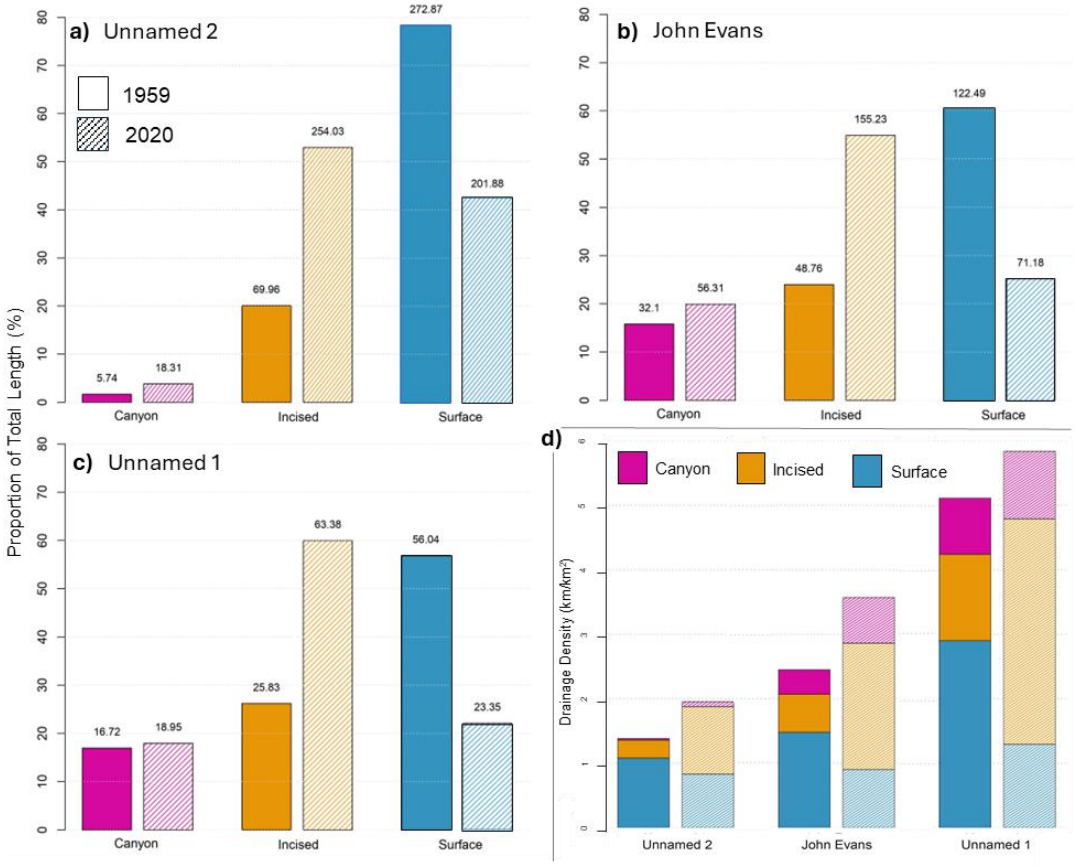

Figure 12. (a-c) Proportion of total channel length (%) in canyon, incised, and surface classes for 1959 and 2020 on: (a) Unnamed 2 Glacier, (b) John Evans Glacier, (c) Unnamed 1 Glacier. Data labels indicate the total length (km) of channels in each class for each year. Additionally, (d) shows the contribution of each class to the total drainage density for each glacier for the years 1959 and 2020.

2.4.3.1 Spatiotemporal Variability of Supraglacial Channels

2.4.3.1.1 Drainage patterns

Since 1959, the dendritic pattern of the western accumulation area of Unnamed 2 Glacier has broadened as channels have expanded further into the accumulation area (Figure 13a). In 1959, this upper system was generally less well connected to the downstream system, with channels terminating in an unchannelized distributed area before becoming channelized again below the ELA (~900 m a.s.l.), near ~800 m elevation. These channels then terminated in a similar system of sinks as observed in 2020. Below this point, fewer channels redeveloped in 1959 than 2020. In the lower half of the glacier, similar to 2020, a large parallel system of rivers formed towards the terminus. However, in 2020, this system extends much further up glacier into the 400

m band than it did in 1959 (Figure 7, Figure 13a). While similar sink locations were present in 1959 and 2020 in the southeastern section of the accumulation area, inhibiting the progression of smaller channels down glacier, new sink locations were present across other sections of the accumulation zone in 2020 as smaller rivers formed at higher elevations. While two sinks were mapped near the terminus of the glacier in 1959, no such sinks were found in 2020.

While John Evans Glacier has become more efficiently drained due to the development of new rivers and the expansion of existing ones, its overall drainage pattern has not changed considerably. Broad dendritic channels still dominate its accumulation area, transitioning to more parallel systems at mid elevations near the ELA (~700 m a.s.l.) and lower elevations toward the terminus (Figures 9, Figure 13b). At lower elevations, between the 100 and 400 m bands, large canyons have become more parallel over time and have increased in their lateral abundance. Although sink regions have remained relatively constant over time, new sinks have developed in the central western accumulation area, much like Unnamed 2 Glacier, with the formation of smaller channels at higher elevations. The central sink zone, located near 600 m, has also evolved with the formation of new moulins at the endpoints of new canyons and the migration of one existing moulin down glacier. Additionally, sinks present on the southern margin of the main glacier trunk and near the terminus in 2020 were not identified in 1959.

Canyon rivers on Henrietta-Nesmith Glacier already had a well-established parallel pattern near the terminus in 1959 (Figure 13c). However, they were much less extensive in 1959 than 2020, with most not extending beyond the terminus region. No sinks were identified in 1959, with all rivers directly flowing off the glacier surface, while in 2020, two sinks were found (Figure 10).

Compared to the other glaciers, Unnamed 1 seems to have experienced the greatest channelization over time, despite little evolution in its total channel length, with channels becoming far more prominent beyond the 1960 ELA position of ~400 m a.s.l. In 1959, the central portion of the glacier was dominated by many subdendritic and subparallel tributary surface channels to larger rivers and canyons (Figure 13d). By 2020 some of these surface channels had merged, becoming more well-channelized and slightly longer rivers, with mostly subparallel and parallel arrangements (Figure 11). Unlike the other glaciers, the singular sink mapped in 1959 was also the only one mapped in 2020 (Figure 11, Figure 13d).

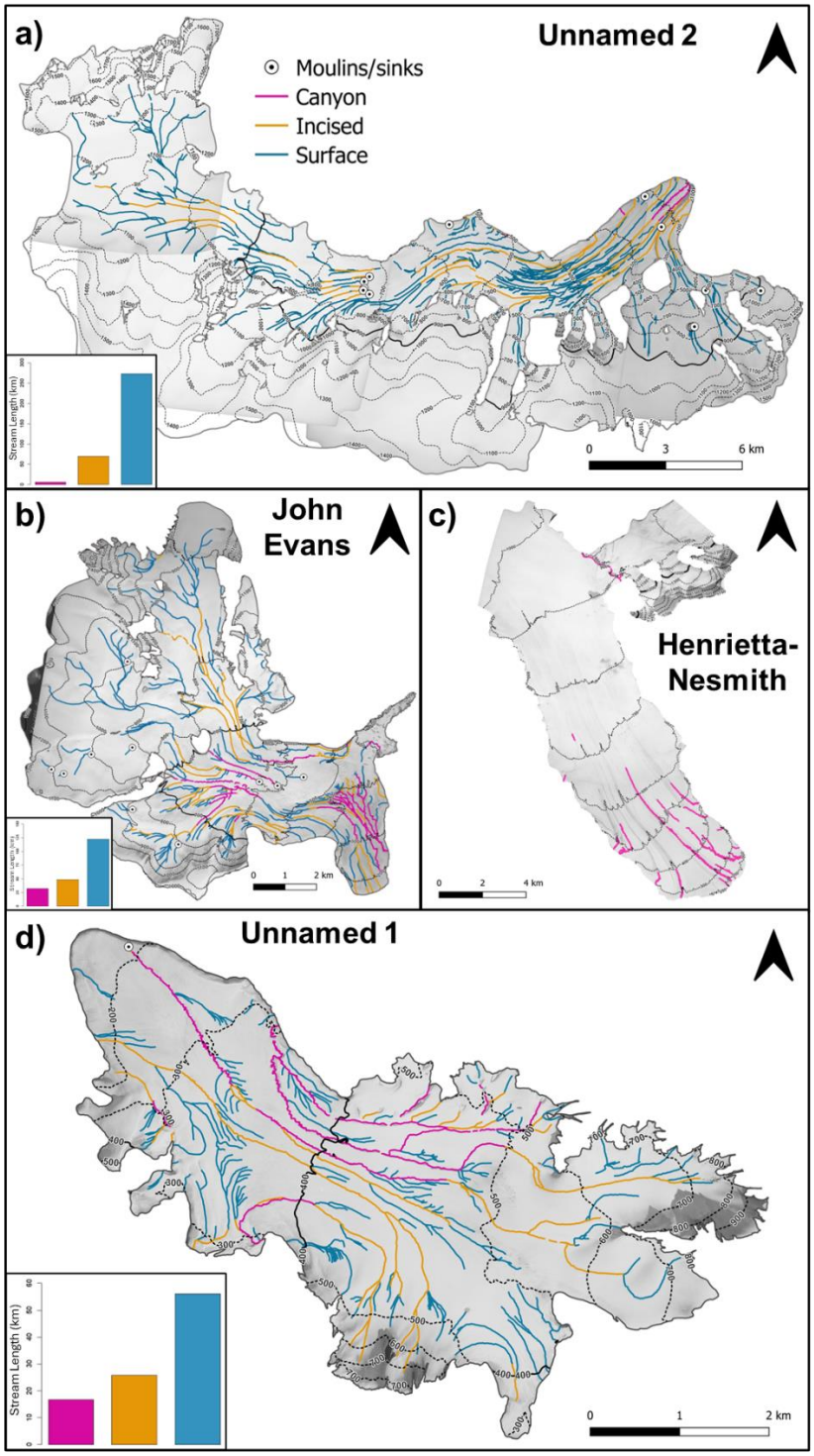

Figure 13. Canyon, incised and surface channels along with moulins and sink areas on (a) Unnamed 1, (b) John Evans and (d) Unnamed 2 Glacier delineated on historical air photographs from 1959. (c) Shows canyons delineated on Henrietta-Nesmith Glacier. Solid black line represents the 1960 ELA estimated from the reconstruction of Miller and others (1975). The ELA is positioned at 900 m a.s.l. on Unnamed 2, 700 m a.s.l. on John Evans, 1200 m a.s.l. on Henrietta-Nesmith and 400 m a.s.l. on Unnamed 1. The insets show the total stream length (km) for each stream class.

2.4.3.1.2 Changes in total drainage density

The changes in the different supraglacial hydrological systems were quantified by comparing the total D_d on each glacier in 1959 and 2020 (Figure 14). Over this period, D_d increased at all elevations on both John Evans Glaciers and Unnamed 2, with a particularly large increase in the first 300 m of elevation from the terminus (Figure 14b and 14c). On both glaciers, D_d increased the most in the 200 m elevation band, by 55.7% on John Evans and 114.5% on Unnamed 2. However, the peak D_d shifted from the 600 m band to the 200 m band on John Evans and from the 300 m band to the 100 m band on Unnamed 2. Despite this, channels now extend further into the accumulation areas of each glacier, with channels reaching the 1400 m band on Unnamed 2 where they were previously absent in 1959.

The D_d pattern on Unnamed 1 shows a more complex evolution (Figure 14a). D_d on this glacier increased in all bands, except for the 300 m band. In contrast to the other two glaciers, D_d increased substantially beyond the 1959 ELA, particularly in the 700 m elevation band, where it rose by 103.4%. The peak D_d also shifted, but this time up glacier from the 300 to the 400 m band and increasing only slightly from 6.97 to 7.12 km/km^2.

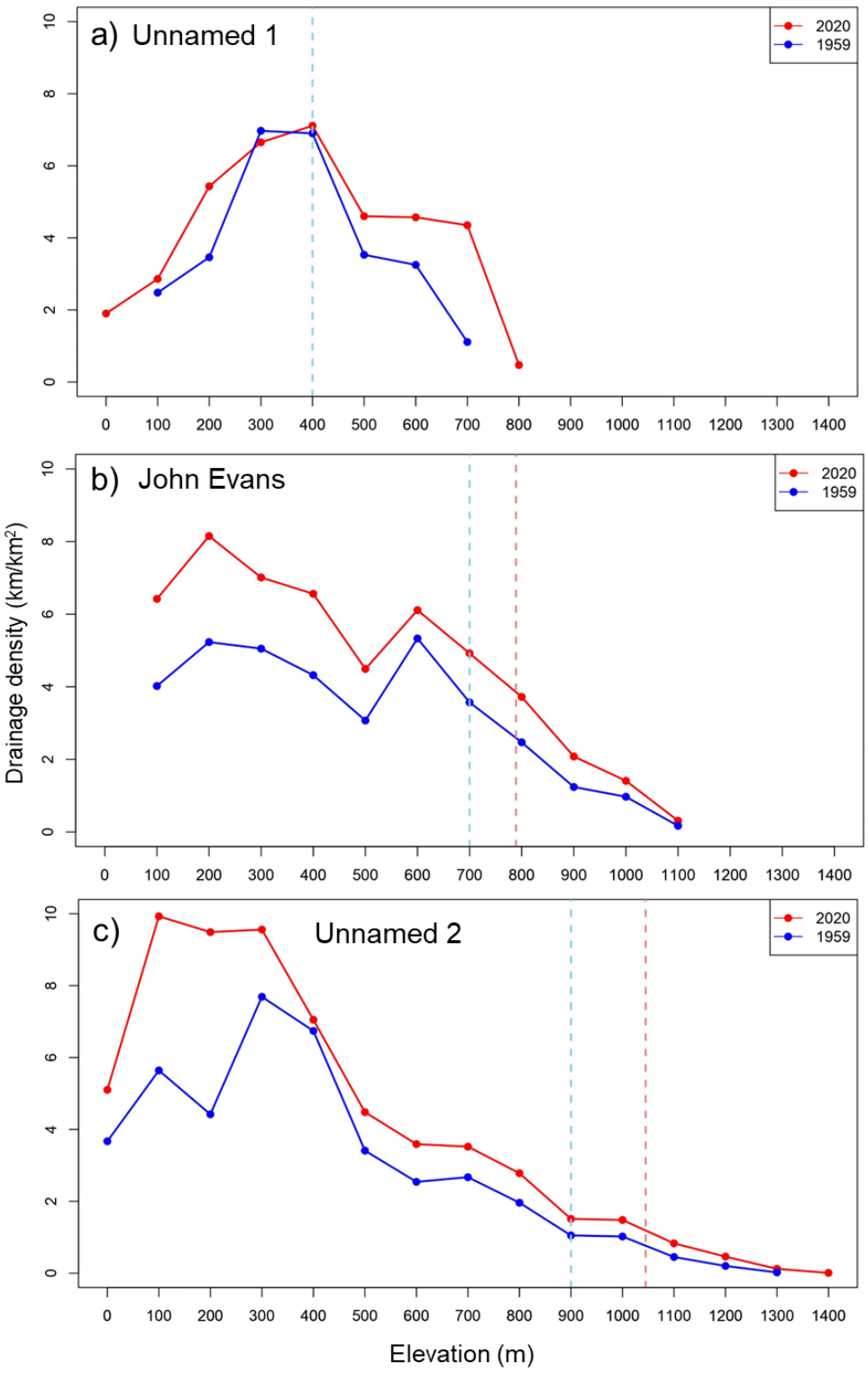

Figure 14. Total drainage density (D_d) by elevation band for 1959 (blue line) and 2020 (red line) for glaciers a) Unnamed 1, b) John Evans and c) Unnamed 2. ELAs for 1960 and 2020 are shown as the dotted light blue and pink lines, respectively. No ELA is shown for Unnamed 1 in 2020 as it is now above the highest elevation of the glacier.

2.4.3.2.3 Relative distribution and abundance changes by channel class

Unnamed 2 Glacier

Not only is there an observed change in the overall D_d pattern over time, but changes in the relative distribution and abundance per channel class are also evident. Since 1959, the relative distribution of canyons on Unnamed 2 Glacier has shifted (Figure 8d, Figure 15d). The majority of the total canyon length, previously concentrated in the 100 m band (68.53%), is now more evenly distributed between the 100 and 200 m bands. Canyon D_d has increased across elevations from the 0 to the 400 m band, and they are now observed up to the 500 m band where they were previously absent (Figure 8h, Figure 15h). This has been accompanied by a notable shift in peak canyon D_d from the 0 to 100 m band between 1959 and 2020. While canyons were most abundant among other channel types only in the 0 m band in 1959, they are now most abundant in the 100 m band as well, whereas in 1959, incised rivers dominated (Figure 8h, Figure 15h).

Similarly, the proportion of the total length of incised rivers has also increased at higher elevations. In 1959, the greatest proportion of incised rivers on Unnamed 2 Glacier was found in the 300 m band (Figure 15d). Since then, the proportion of incised rivers in the 300 m band has declined, stabilizing more between the 600 and 800 m bands (Figure 8d). This shift has led to a notable increase in the abundance of incised rivers (D_d) relative to other channel classes at higher elevations, with important rates of increase observed between the 800 m and 1100 m bands and the extension of rivers upglacier beyond the 1100 m band, where they were previously absent (Figure 8h, Figure 15h).

John Evans Glacier

A similar trend is observed on John Evans Glacier. Although peak canyon length is still found in the 300 m band, the proportion of total canyon length has decreased in both this band and the 600 m band as canyon length has increased at other elevations (Figure 8c, Figure 15c). Additionally, canyon D_d has increased across all elevations between the 100 and 700 m bands, including the 800 m band where canyons were previously absent (Figure 8g, Figure 15g). In 1959, canyons exceeded other classes in abundance only in the 300 m band, but now they are also more abundant in the 200 m band and surpass surface streams in the 500 and 600 m bands (Figure 8g, Figure 15g).

Similarly, there has been a shift in the distribution of incised river length to higher elevations on John Evans Glacier with rivers extending into the 1100 m band, compared to their maximum extent in the 900 m band in 1959. Previously, the total length of incised rivers was concentrated in the 600 m band, but it is now predominantly found in the 800 m band (Figure 8c, Figure 15c). Overall, there has been an increase in the proportion of total river length at higher elevations compared to 1959, with a particularly notable rise in the 900 m band. Additionally, the D_d of incised rivers has doubled or nearly doubled between elevation bands of 400 and 900 m, making them the most abundant type over other classes at those elevations (Figure 8g, Figure 15g). In the upper accumulation area, D_d increased most substantially in the 700 m band, where the ELA rose from 700 m a.s.l. in 1960 to 789 ± 52 m a.s.l. in 2020. This shift has been accompanied by substantial increases in D_d observed in the initial elevation bands of the accumulation area.

Henrietta-Nesmith Glacier

A similar pattern for canyon rivers is also observed at Henrietta-Nesmith, where canyons only extended as far up glacier as the 800 m band in 1959, compared to the 1100 m band in 2020, with D_d values increasing at all elevations and the peak value shifting from the 200 m to the 400 m band (Figure 8b and 8f, Figure 15b and 15f).

Unnamed 1 Glacier

On Unnamed 1 Glacier, there were fewer changes in canyon length between 1959 and 2020, with the total length being relatively similarly distributed between the 200 and 400 m bands (Figure 8a, Figure 15a). However, the peak percentage of canyons has shifted from the 400 m band to the 300 m band over the 60-year period, accompanied by a slight decrease in canyon D_d in the 400 m band (Figure 8a and 8e, Figure 15a and 15e). Nonetheless, canyon D_d has increased at all other elevations, with a marked increase of almost 3-fold in the 500 m band.

Similarly, the proportion of total incised channel length from the 0 to 400 m elevation bands has remained relatively stable over the study period. However, there has been a decrease in the 500 m band, followed by increases further upglacier in the 600 and 700 m bands and reaching the 800 m band where rivers were previously absent (Figure 8a, Figure 15a). In contrast, the D_d of incised rivers has more than doubled across the majority of the glacier surface between

the 100 to 800 m elevation bands, with substantial increases observed in bands beyond the 1960 ELA and the most important increase in the 700 m band (Figure 8e, Figure 15e).

In contrast to these two channel classes, the distribution of surface streams on all glaciers has not changed much between 1959 and 2020 (Figure 8a-d, Figure 15a-d). However, D_d has decreased for surface streams in almost every band across all glaciers over the study period (Figure 8e-h, Figure 15e-h).

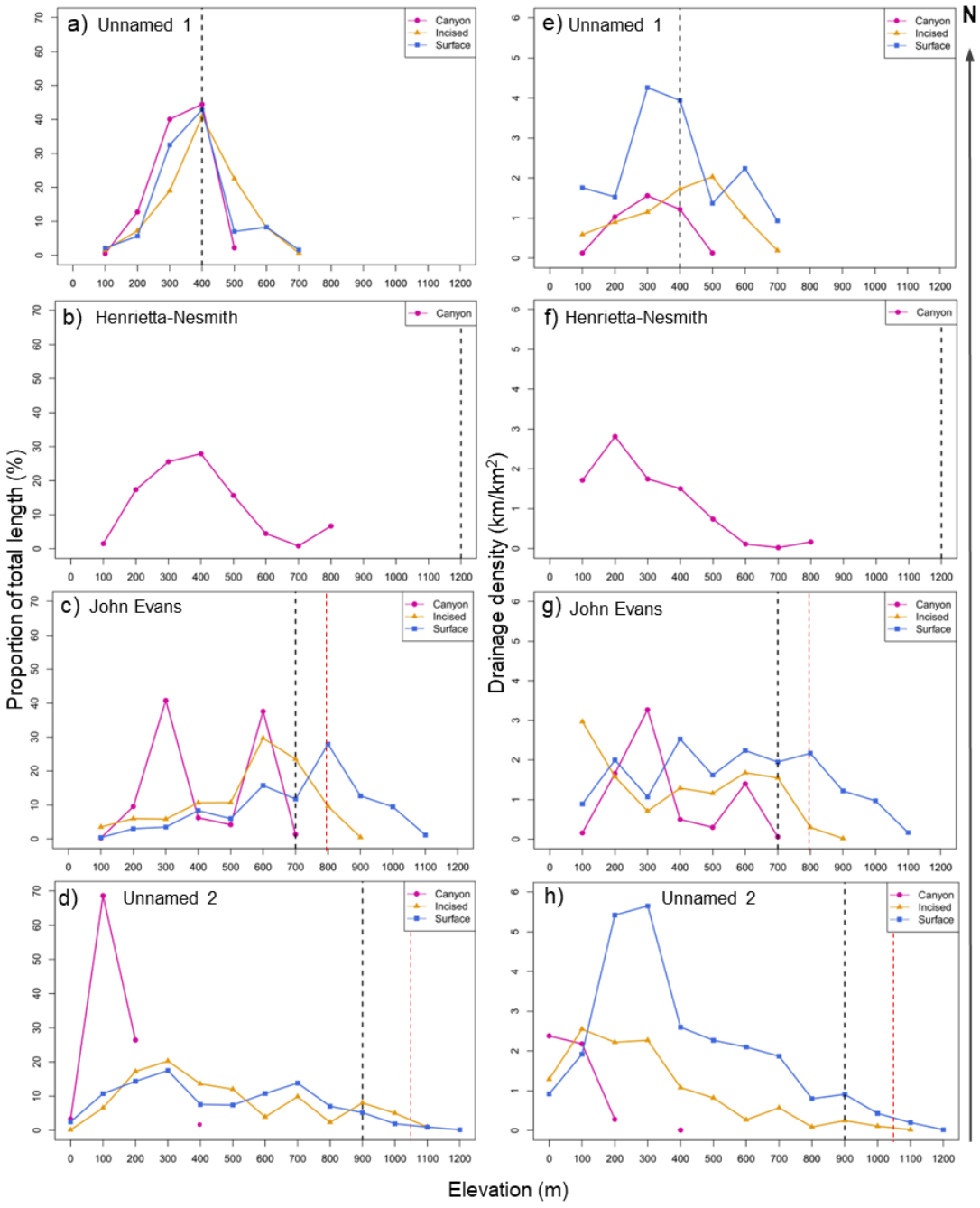

Figure 15. Proportion of total length (%) by class as a function of elevation (a-d) and drainage density (e-h) as a function of elevation for the four studied glaciers in 1959. Graphs are organized by latitude based on the location of each glacier: (a and e) Unnamed 1 (82.998°N); (b and f) Henrietta-Nesmith (81.857°N); (c and g) John Evans (79.650°N); and (d and h) Unnamed 2 (78.793°N). Elevation is capped at 1400 m, which represents the highest elevation band at which channels were mapped. The black and red dotted lines show the position of the 1960 and 2020 ELAs, respectively. No ELA is shown for Unnamed 1 in 2020 as it is now above the highest elevation of the glacier and no ELA is shown for Henrietta-Nesmith in 2020, as it is located further upglacier.

2.4.3.2 Changes in Sinuosity

The sinuosity statistics for the four mapped glaciers reveal varied temporal and spatial patterns of canyon meandering in 1959 and 2020 (Figure 16, Table 5). Channel distribution by sinuosity level differs markedly among the glaciers. By 2020, Unnamed 2 Glacier had 87.6% of its canyons classified as sinuous or meandering, with a notable inclination towards meandering channels. John Evans Glacier displayed 72% of its canyon length as sinuous channels, while meandering and straight channels made up the remainder, distributed relatively evenly. Henrietta-Nesmith Glacier mirrored Unnamed 2's pattern, with 96.6% of its canyons being sinuous or meandering, strongly favoring meandering channels. In contrast, Unnamed 1 Glacier's total canyon length was comprised of 88.3% sinuous and straight channels, with a slight predominance of sinuous channels.

Since 1959, the proportion of channel types has shifted across the glaciers. On Unnamed 2 Glacier, the combined contribution of meandering and sinuous channels has decreased by 10.6%, with a 4.8% drop in meandering channels. Conversely, John Evans Glacier saw a slight increase in sinuous channels and a nearly fourfold rise in meandering channels. On Henrietta-Nesmith Glacier, the overall contribution of sinuous and meandering channels increased by 7.6%, although meandering channels alone fell by 11.9%. On Unnamed 1 the percentage of straight and sinuous channels decreased by 8.2% as meandering channels became more prevalent, yet the proportion of straight channels increased by 8.1%.

These observed patterns generally align well with the sinuosity statistics. In 1959, median sinuosity values were generally higher for most glaciers, except for John Evans, compared to 2020 (Figure 16). This is particularly evident on Unnamed 1 Glacier, where the median, interquartile range, and a single outlier from 1959 show substantially higher sinuosity values than those recorded in 2020 (Figure 16). Despite the overall decrease, some glaciers exhibit considerable variability in sinuosity, with multiple outliers in both years indicating sporadic instances of higher sinuosity (Figure 16). This variability is especially notable for glaciers other than Unnamed 1, where the number of outliers increased, and maximum values rose for Unnamed 2 and John Evans. Consistent with standard deviation values, interquartile ranges for 1959 tend to be larger for northern glaciers (Henrietta-Nesmith, Unnamed 1), while southern glaciers (Unnamed 2, John

Evans) show increased variability in 2020, indicating a trend towards greater variability in the south and reduced variability in the north (Table 5). Despite these observations, p-values do not yield statistically significant results when comparing the distributions of sinuosity values in 1959 and 2020 (Table 5).

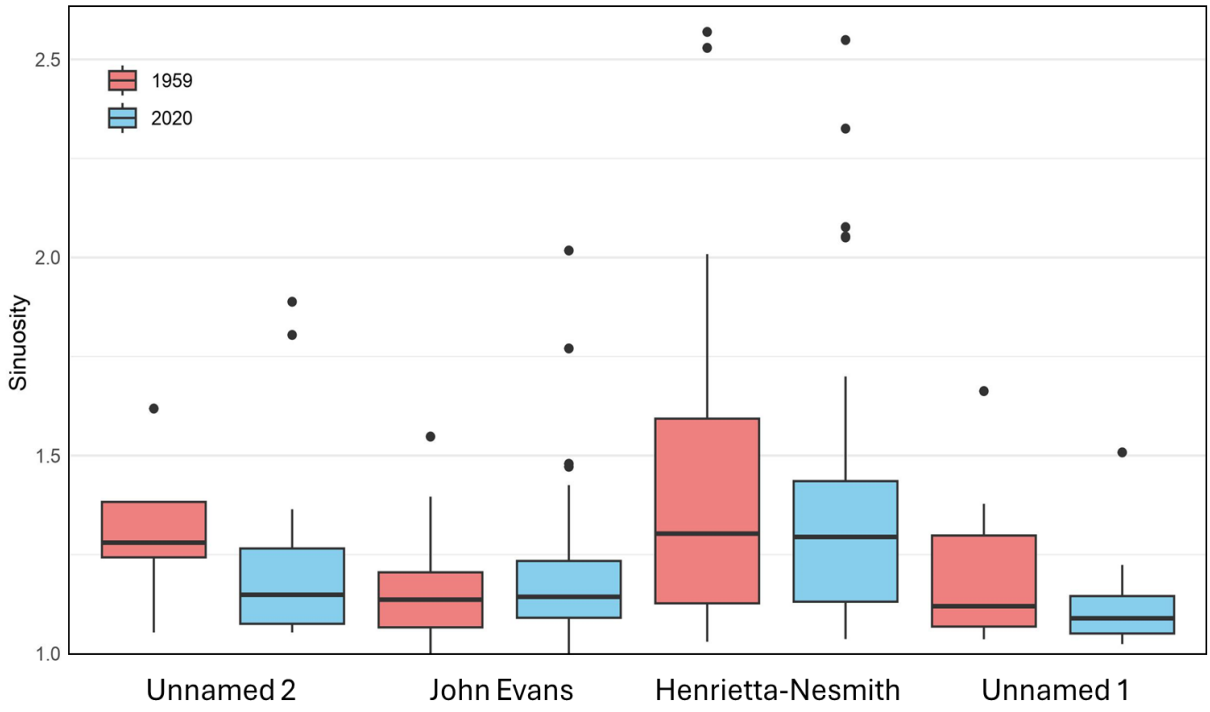

Figure 16. Box plot showing the sinuosity statistics for Unnamed 2 Glacier, John Evans Glacier, Henrietta-Nesmith Glacier, and Unnamed 1 Glacier for the years 1959 and 2020. The box plot includes the median, interquartile range, and outliers, illustrating the distribution and variation in sinuosity values for each glacier across the two time periods.

Table 5. Sinuosity statistics for the four mapped glaciers for 1959 and 2020 with 'weighted' abbreviated as 'W'. The p-values from the Mann-Whitney U test, which compares the distributions of sinuosity values between these years, are also included.

Statistics	Unnamed 2		John Evans		Henrietta-Nesmith		Unnamed 1	
	1959	2020	1959	2020	1959	2020	1959	2020
W.Avg	1.50	1.52	1.18	1.31	1.61	1.40	1.20	1.17
W.SD	0.15	0.35	0.11	0.24	0.44	0.33	0.15	0.14
Min	1.05	1.05	1.00	1.00	1.03	1.04	1.04	1.02
Max	1.62	1.89	1.55	2.02	2.57	2.55	1.66	1.51
Med	1.28	1.15	1.14	1.14	1.30	1.29	1.12	1.09
W.Skew	-0.31	-0.02	0.20	0.15	0.13	0.16	0.25	0.37
MWU Test	0.44		0.39		0.57		0.21	

2.5 Discussion

The qualitative and quantitative analyses indicate the development of an increasingly well-developed perennial supraglacial hydrological system across all mapped glaciers between 1959 and 2020. In the following section the results are consolidated and contextualized to better understand this observed trend through a discussion of the possible mechanisms influencing each glacier, including a comparison with other studies. This includes a discussion of the drivers behind these changes, primarily related to alterations in surface melt patterns. The section concludes with future predictions, followed by a discussion of the limitations and assessment of the mapping framework.

2.5.1 Development of Supraglacial Drainage Systems

2.5.1.1 Drainage Patterns

On all mapped glaciers, the supraglacial hydrological systems exhibit a generally consistent drainage pattern. Dendritic networks are commonly found at higher elevations, where glacier surfaces widen into their accumulation zones, and variations in surface relief become more pronounced. As these networks flow down the main glacier trunk they become subparallel, indicating fewer variations in surface relief (Karlstrom and Yang, 2016; Yang and others, 2019). Towards the terminus, the networks become more parallel, and larger rivers and highly sinuous canyons begin to form as surface meltwater becomes more channelized. Numerous studies (Karlstrom and Yang, 2016; Crozier and others, 2018; Ignéczi and others, 2018; Yang and others, 2019; Lu and others, 2020) suggest that such differences in surface drainage patterns are influenced by the transferability of variations at the glacier bed to the surface, such as basal roughness and slipperiness. Rougher beds with more friction create complex surface topographies, particularly in accumulation areas, while smoother, slipperier beds lead to more streamlined ice flow and simpler surface patterns, as observed further down the glaciers. Several studies on polythermal glaciers in the NCAA, such as on White Glacier on Axel Heiberg Island and John Evans Glacier, report this pattern of enhanced glacier velocities in the ablation area resulting from basal sliding (Blatter, 1987; Copland and others, 2003c; Thomson and Copland, 2017).

Maps of supraglacial drainage patterns in the NCAA are limited, with recent studies focusing mainly on the large Devon Ice Cap (Yang and others, 2019; Lu and others, 2020), to the

south of our study area on Ellesmere Island. For instance, Lu and others (2020) found similar drainage patterns to those observed in the current study, with supraglacial channels at high elevations displaying broad, dendritic patterns that evolved into more organized, channelized, subparallel configurations as they flowed to lower elevations, eventually forming regularly spaced, parallel mainstems within outlet glacier trunks. Consistent with our findings, and with those of other studies on polythermal glaciers in the NCAA, SCAA, Greenland, and Svalbard (Rippin and others, 2015; St. Germain and Moorman 2016; St. Germain and Moorman, 2019; Yang and others, 2019; Lu and others, 2020), sinuosity was notably high within the main stems and increased towards lower elevations, particularly near the glacier terminus. Charlton (2007) notes that natural rivers generally adjust their slope—typically decreasing it—by increasing their sinuosity. On Fountain Glacier, Bylot Island, St. Germain and Moorman (2019) studied seven different supraglacial channels and found that all flowed relatively straight until reaching the sloped terminus, where lateral meanders developed at rates of 0.2 to 1.9 m a^{-1}, depending on channel size.

While our study did not specifically investigate meander growth, the overall sinuosity values for canyon rivers show no significant changes between 1959 and 2020 (Table 5). This lack of significant change is likely due to the high channel dynamism of these glaciers, where continuous bank erosion due to melting causes the closest points of a meander bend to connect. Consequently, the water no longer follows the more tortuous meander path, forming a straighter channel (Rippin and others, 2015). Over time, new meanders form as channels adjust their slope, effectively restarting the process (St. Germain and Moorman, 2019). This suggests that channels across different glaciers are at varying stages of their evolution, which is particularly important when considering the development of new perennial channels, such as those observed in the time series for Henrietta-Nesmith Glacier (Appendix, Figure 2-A). In addition, St. Germain and Moorman (2019) show that canyon sinuosity is highly correlated to factors such as slope and watershed area which affects discharge, meaning that different canyons will develop meanders at different rates.

While considerable channel dynamism was observed in canyon rivers across all glaciers, notable meander cutoffs documented in the multidecadal time series for Unnamed 2 and

Henrietta-Nesmith glaciers suggest greater dynamism on these glaciers (Appendix, Figures 1-A and 2-A). Despite insignificant changes indicated by the Mann-Whitney U test, overall trends in sinuosity values over the study period suggest reduced variability towards lower sinuosity values in far northern areas, such as Unnamed 1 Glacier, indicating increased channelization and stability within the supraglacial system there (Table 5). The low number of meander cutoffs observed in the image time series of this glacier further suggests stability over time (Figure 5). On John Evans Glacier, the evolution from less permanent rivers to more permanent ones, which incised over time, may indicate a tendency towards more meandering channels in recent years (Figure 4). This transition, observed in the time series, suggests that many rivers evolved into their canyonized state over the study period, taking more time to develop into meandering canyons.

2.5.1.2 Changes in Drainage Density

While drainage patterns are largely similar across the different glaciers, the total channel length and thus the total D_d varied substantially from one glacier to another, with the highest D_d on the northernmost glacier (Unnamed 1) and the lowest on the southernmost glacier (Unnamed 2) for both 1959 and 2020 (Figure 12d). Additionally, supraglacial channels were widespread across the entirety of Unnamed 1 Glacier which now only consists of an ablation area, compared to the other glaciers, which still have large accumulation areas.

As noted by Rippin and others (2015), glaciers with extensive cold ice content are less dynamic, exhibiting smoother surfaces with few crevasses, thereby limiting the access of surface meltwater to englacial and subglacial locations. Consequently, supraglacial channels tend to be widespread on these ice masses, draining water from a wide area (Irvine-Fynn and others, 2011; Ryser and others, 2013; Rippin and others, 2015). Bash and others (2022) compared their channel maps for Nàłùdäy Glacier in the Yukon to those for Thores Glacier on Northern Ellesmere Island, finding that distinct supraglacial channels were 98% more common on Thores Glacier, where the ice is believed to be entirely frozen to the bed (Kochtitzky and others, 2023). This suggests a more widespread distribution of channels on the northern glacier, mirroring the patterns observed in the current study.

Over the study period, overall drainage patterns have remained largely similar, but the density of channels has increased. This change is primarily driven by the rise in total channel

length rather than the decrease in surface area on Unnamed 2 and John Evans glaciers, contributing to 86.7% and 85.7% of the total increase in D_d, respectively. On both glaciers, total D_d increased across all elevation bands. This is consistent with Lu and others' (2020) findings that supraglacial rivers extended further up-glacier during a melt season as the snowline retreated to higher elevations. While these authors examined this effect over a single melt season, their results suggest that substantial changes at higher elevations are possible when temperatures and corresponding meltwater production rates are sufficiently high.

Although changes at higher elevations were observed, we noted even greater rates of change further down-glacier on Unnamed 2 and John Evans glaciers, driven by a dramatic increase in canyon D_d in the terminus region where canyons have become more prominent compared to incised and surface channels (Figure 14b and 14c).

In contrast to the other glaciers, the reduction in surface area on Unnamed 1 Glacier has a slightly greater impact on the overall D_d, contributing 50.7% to the increase. This suggests that changes in the supraglacial hydrological system are generally less pronounced on Unnamed 1 compared to the other glaciers. Similarly, little evidence for significant changes in the extent and distribution of distinctive supraglacial channels between 1959 and 2019 was found on the nearby Thores Glacier (Kochtitzky and others, 2023).

Additionally, we found slightly higher D_d in the 300 m elevation band on Unnamed 1 in 1959 than in 2020 (Figure 14a). This difference is likely due to clusters of subdendritic and subparallel surface streams in the glacier's central portion in 1959, which had largely dissipated by 2020, evolving into more channelized, subparallel, and parallel configurations dominated by incised rivers (Figure 11, Figure 13a). Changes in D_d with elevation suggest greater rates of change at higher elevations on Unnamed 1 compared to the other two glaciers, likely due to the already dense system of incised rivers and canyons established in 1959 at lower elevations (Figure 14). This pre-existing density facilitated faster rates of change further up-glacier, especially for incised rivers, as the ELA retreated, and the entire glacier surface became part of the ablation area.

The observed changes in D_d across these glaciers are primarily driven by the increased presence of canyon and incised channels. On Unnamed 2 through Henrietta-Nesmith glaciers, canyons have extended further up glacier, while incised rivers have expanded further into

accumulation zones on all glaciers studied (Figure 8, Figure 15). Although the total D_d on John Evans and Unnamed 2 glaciers did not increase as much at higher elevations compared to their lower ablation area, substantial changes within individual channel classes, particularly incised channels, are notable. The most substantial alterations are evident near and within the elevation band that transitioned from the accumulation area to the ablation area, reflecting the rise in the ELA since 1960 which has risen by as little as ~53 m on Henrietta-Nesmith to more than 580 m on Unnamed 1 (Figure 8e-h, Figure 15e-h). This transition zone ultimately became subject to higher melt rates, leading to increased meltwater availability and enhanced erosion facilitating the development of new rivers.

2.5.1.3 Changes in Channel Types

Not only has the D_d changed across the different glaciers but the supraglacial drainage systems of all glaciers, except Sydkap, have evolved towards more perennial characteristics, as observed through notable changes to the composition of channel types (Figure 12a-c). The dominance of incised channels and the increased contribution of canyons to the total channel length suggest a greater incision of the supraglacial drainage system, where water is more likely to occupy channels perennially. Although only canyon rivers were mapped on Henrietta-Nesmith, this glacier experienced an important increase in total canyon length over the study period which is indicative of a shift towards a more established perennial system, especially at higher elevations. In the context of this study, the transition to a more perennial system may have occurred through two main processes: 1) gradual progression from surface streams to incised rivers and from incised rivers to canyons, and/or 2) the formation of new rivers and/or the extension of old ones. Due to the substantial increase in total channel length on both Unnamed 2 and John Evans glaciers, we suggest that both processes are at play on these glaciers, while the former appears to be more dominant on Unnamed 1 due to the minimal change in total channel length there. Important multi-decadal changes in incision observed in the time series also suggest this (Figure 5).

Apart from the current study, only St. Germain and Moorman (2019) have examined the development of various channel types in the CAA. Their findings, similar to those of Knighton (1981) in Norway and Marston (1983) in Alaska, indicate that discharge and surface slope are

crucial factors in the formation of supraglacial canyons. They observed that higher discharge rates and steeper glacier gradients are directly proportional to faster incision rates. In the present analysis, the formation of new canyons often occurs in locations of previously incised rivers, suggesting a natural progression from incised rivers to canyons rather than the formation of new, independent ones. Thus, the combination of a suitable glacier gradient and high discharge over the study period likely facilitated important erosion via melting of the stream bed and banks within incised rivers. This process ultimately led to canyon formation as the water became confined within the valley walls, unable to overflow the banks and change course (St. Germain and Moorman, 2019). This natural progression is clearly observed in the multi-decadal time series, where the evolution of larger rivers can be tracked through time (Figures 4 and 5, Appendix Figures 1 and 2-A).

Although observed in some cases, particularly further up the glaciers and into their accumulation area, the natural progression from surface to incised streams appears to be less important. Instead, the extension of old rivers, the development of new ones, and the merging of multiple channels into one, seem to be more important. Due to the shallow valleys of surface streams, water often overflows their banks, allowing them to be redirected from year to year (St. Germain and Moorman, 2029). As a result, many surface streams most likely continued to change their course until fluvial conditions – such as slope and discharge– were optimal for the formation of incised rivers.

The substantial reorganization of channel types across the different glaciers entails shifts in channel locations across their surfaces. This trend is evident across all mapped glaciers, where the proportion of total canyon length has decreased at lower elevations in response to increases further up glacier (Figure 8a-d, Figure 15a-d). Similarly, the distribution of incised rivers on Unnamed 2, John Evans and Unnamed 1 has also changed with decreases in their relative total length at lower elevations and increases further up glacier. These changes highlight a clear trend: although canyons and incised rivers continue to be important at lower elevations, they have become increasingly widespread across the glacier surface. This expansion at higher elevations aligns with the rise in D_d indicating a growing prominence of these features across the glacier.

2.5.1.4 Amount and Rate of Change

While changes to the supraglacial system over time are apparent on all studied glaciers, the amount and rate of change are not consistent across all of them. The rate of change in each stream class and their contribution to the total length and total D_d generally follow a gradient from greatest on Unnamed 2 in the south to least on Unnamed 1 in the north, with the exception of canyons on John Evans in 2020 (Figure 12a-d). Combined, changes in the rate and contribution of each stream class show that canyons and incised rivers now dominate 77.8% of the total D_d on Unnamed 1, while they account for smaller percentages on John Evans and Unnamed 2 (Figure 12a-c). Although surface streams were dominant on all glaciers in 1959, the proportion of incised and canyon channels was still larger on Unnamed 1 at 43% compared to John Evans and Unnamed 2, at 39.8% and 21.7%, respectively.

Although incised and surface channels were not mapped on Henrietta-Nesmith, canyons on this glacier show substantially lower total canyon D_d than any other glacier for both 1959 and 2020. We attribute this to the extremely large accumulation area on Henrietta-Nesmith (~849 km^2), which covers a significant portion of the glacier's surface and limits the area available for supraglacial channel development. When changes within only the ablation area are considered for all glaciers, the total canyon D_d fits well with the observed gradient for both 1959 and 2020.

These changes suggest generally higher rates of incision on Unnamed 1 compared to the other glaciers. This conclusion is supported by several lines of evidence: (1) the absence of crevasses enabling the formation of an extensive supraglacial system; (2) the qualitative assessment of the multi-decadal time series which reveals that incision has been an important driver of change on Unnamed 1, particularly over the last decade; (3) the formation of numerous cut-and-closure channels within canyon rivers throughout the study period (Figure 17); and (4) the abandonment of a canyon river due to the formation of a chain of incised supraglacial lakes (Figure 17).

Gulley (2009) explored the formation of cut-and-closure channels on a polythermal glacier in Svalbard and found that such conduits are more likely to form in uncrevassed sections of glaciers where channel contributing areas are large and where meltwater is not transferred to the glacier's other hydrological systems. Additionally, roof blockage appears to be climatically

controlled, with snow and ice bridges more likely to survive the following melt season if surface ablation rates are small, such as on glaciers in far northern areas like those in the NCAA (Noël and others, 2018) (Figure 18a). While cut-and-closure conduits were not exclusive to Unnamed 1 and were also largely present in the northern ablation area of John Evans Glacier, the combination of such factors with other evidence suggests that incision rates remain greater on Unnamed 1. In particular, the formation of a chain of supraglacial lakes in the middle of Unnamed 1, where a canyon river used to flow, suggests that the process of incision might have been so extensive in some areas that the river could no longer sustain itself and became disconnected entirely (Figure 17).

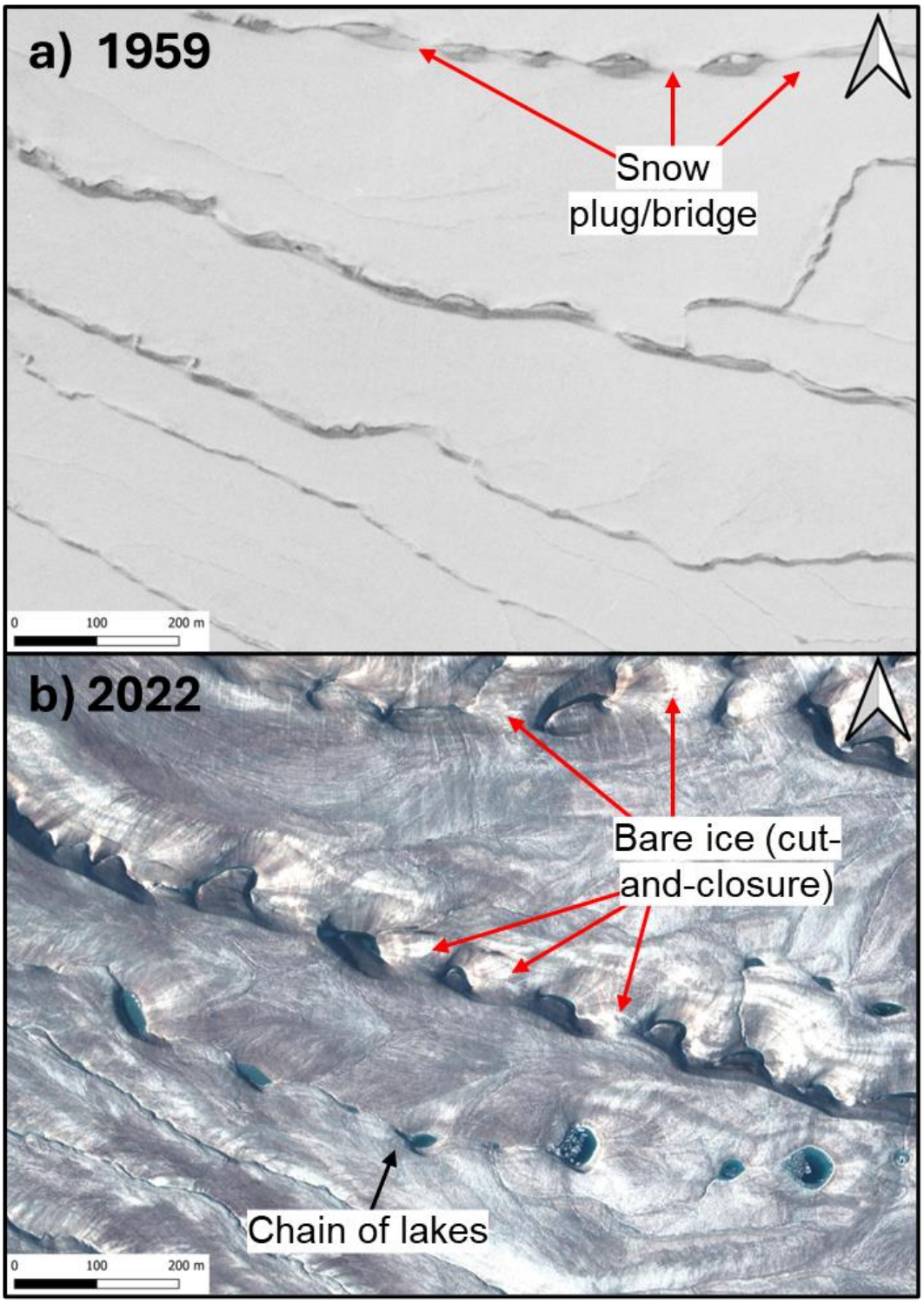

Figure 17. Evolution of cut-and-closure channels and the formation of supraglacial lakes on Unnamed 1 Glacier from 1959 to 2022 a) ~0.6 m resolution historical air photo showing the location of snow plugs within the channel and b) 0.5 m pansharpened WorldView 3 image of the same location showing that snow plugs have become bare ice, forming cut-and-closure channels, and the presence of a lake chain in place of an old channel. See Tables 1 and 2 for image dates.

2.5.1.5 Changes in Sink Distribution

Changes to the number of hydrologically significant sinks between glaciers and over the study period are also evident across the studied glaciers, particularly at higher elevations. On Unnamed 2 Glacier a notable sink field was identified in the upper ablation area in both years, suggesting potential transfer of supraglacial meltwater to the glacier bed, which may influence glacier velocity patterns (Figure 7a, Figure 13d). Wyatt and Sharp (2015) observed that velocity variability on Devon Ice Cap was often higher near sink-point locations, likely due to enhanced basal sliding or bed deformation in these areas.

Similarly, on John Evans Glacier, we confirmed the presence of sinks in the two moulin fields described by Bingham and others (2003): one over a large ridge in the central ablation zone, and another in the lower western accumulation area. Furthermore, we identified additional and new sink formations further into the western and southern accumulation areas, which were not previously documented (Figure 9, Figure 13c). Previous research shows that these moulin fields are associated with intra-seasonal and intra-annual flow dynamics on this polythermal glacier, underscoring its sensitivity to variations in surface meltwater input (Bingham and others, 2003). Bingham and others (2003) also suggest that hydrological coupling between the upper and lower sink fields during late summer can increase mid-glacier velocities. The appearance of new sinks in the western accumulation area of Unnamed 2 Glacier since 1959—located further up-glacier from the prominent sink field in the ablation zone—might indicate a similar pattern of increased velocities, while also suggesting a well-developed subglacial drainage system, as observed on White Glacier at a similar latitude on Axel Heiberg Island (Thomson and Copland, 2017, 2018). Confirming such patterns on these glaciers, however, is beyond the scope of the current study.

In contrast, glaciers located further north show fewer hydrologically significant sinks, with only one identified on Unnamed 1 Glacier in both 1959 and 2020 (Figures 11, Figure 13a). Bash and others (2022) mapped hydrologically significant moulins on Nàłùdäy Glacier in the Yukon and compared them to Thores Glacier on Northern Ellesmere Island, discovering numerous moulins on the former but none on the latter. Similarly, Yang and others (2019) reported that moulins are largely absent in northwest Greenland, whereas they are crucial to the supraglacial drainage systems in southwestern Greenland. The absence of moulins in northwest Greenland has been

attributed to the region's colder, thicker, and less permeable ice, combined with slower flow rates and lower strain rates compared to those observed further south. Many of these factors may also be important on Unnamed 1 Glacier, as Kochtitzky and others (2023) found that nearby Thores Glacier was slow moving and cold-based, with modelled basal temperatures of -7°C to -12°C. These factors may also be relevant to Henrietta-Nesmith Glacier, where only two sink points near the terminus developed over the study period (Figures 10, Figure 13b). The actual number of sinks on this glacier may be underestimated, as our mapping focused solely on canyons in the terminus region. Nevertheless, since sinks in the ablation area typically form at the endpoints of mainstems and crevassing seems to be limited across the glacier surface, our observations still provide a rough estimate of the sink density on this glacier. Consistent with other observations, these findings indicate stronger hydrological coupling between the supraglacial and subglacial drainage systems on glaciers located further south compared to those further north.

2.5.2 Surface Melt Patterns

2.5.2.1 Surface Mass Balance

To better understand the drivers behind the changes observed in various supraglacial systems, we utilized the daily modeled SMB dataset for the NCAA from Noël and others (2018), updated to cover the period from 1959 to 2019. SMB measurements were obtained by summing individual daily components (precipitation, melt, runoff, refreezing, sublimation, and drifting snow erosion), which were extracted and statistically downscaled from the original 11 km resolution regional climate model (RACMO) version 2.3 to a finer 1 km resolution. This downscaling allows for a more detailed evaluation of SMB patterns across smaller glacier surfaces. To address elevation and albedo biases that impact surface melt and runoff, Noël and others (2018) corrected these components using the Canadian Digital Elevation Model, glacier outlines from the Randolph Glacier Inventory 5.0, and bare ice albedo data from the MODerate-resolution Imaging Spectroradiometer (MODIS). A significant correlation with altitude was necessary to correct for elevation bias in components such as runoff, melt, and sublimation. Conversely, snow drift erosion and total precipitation, including both solid and liquid forms, as well as snowfall, exhibited no systematic elevation correlation. Consequently, these components were bilinearly interpolated to match the 1 km glacier outlines without elevation adjustment. In situ stake SMB

measurements collected from 198 sites across the northern CAA between 1959 and 2010 were utilized to validate and refine the model outputs.

In this study, the present-day ELA was used to divide the glaciers into their ablation and accumulation areas. The present-day ELA was chosen over its 1960 counterpart so that melt rates are not overestimated in the accumulation area. The specific surface mass balance (SSMB) for both the ablation and accumulation area on each glacier was calculated by summing all SMB measurements within each area separately and then dividing by the respective surface area. This approach was chosen over calculating the SSMB for the entire glacier basin because glaciers such as Sydkap, Unnamed 2, and Henrietta-Nesmith have extensive accumulation areas, whereas glaciers like Unnamed 1 now have their entire surface within the ablation zone.

Modeled monthly SSMB for the ablation areas of the five studied glaciers reveals significant trends in mass losses since the mid-1960s ($p<0.05$) (Figure 18a-e, Table 6a). These losses in SMB are primarily associated with the melt season, which typically occurs from June to August in the CAA. Since the mid-1960s, snowfall (i.e., SMB gains) in the ablation areas of the five studied glaciers have shown generally low variability (Figure 18), with significant decreases observed only on Sydkap and Henrietta-Nesmith (Table 6a).

When the gains and losses are summed to compute the net annual SMB, all glaciers have exhibited a significant negative trend with substantial increases in losses since the start of the 21st century (Figure 18a-e, Table 6a). Between the periods 1964-1999 and 2000-2019, losses increased between 50% to 119% across all studied glaciers, with maximum values occurring after 2010, except for John Evans, which reached its peak losses in 2008 (Figure 18c and Table 7). Medrzycka and others (2023) observed a similar trend on Bowman Glacier on northern Ellesmere Island, where losses more than doubled from 1958-1999 to 2000-2019, reaching a maximum in 2011 and a decadal average for 2010-2019 higher than the 2000-2019 mean.

Given the small or insignificant trends in snowfall over the ablation area of the studied glaciers, the overall decline in net annual SMB is primarily attributable to heightened summer melt. This suggests a substantial increase in surface meltwater production across the glaciers' ablation areas, although the amount and rate of melt varies between glaciers, somewhat following a latitudinal gradient. The highest losses and rate of change are observed on Sydkap

(furthest south), while the smallest are on Unnamed 1 (furthest north) (Figure 18a-e, Table 7). Between 1964 and 2019, the cumulative value for summer losses amounted to -50.3 m w.e./km^2 on Sydkap, while it was only -15.92 m w.e./km² on Unnamed 1 (Figure 18a and 18e). Similarly, the slope of the linear regression for summer losses suggests faster rates of change on Sydkap than on Unnamed 1 (Table 6a).

These changes are consistent with the observed alterations in the supraglacial systems of the studied glaciers. In the far northern regions, the lower surface melt rates and generally slower rates of change in losses since the mid-1960s contribute to the long-term stability of the substantial supraglacial drainage system (Rippin and others, 2015), as observed on Unnamed 1. On the other hand, the greater surface melt production and higher melt rates observed in recent decades further south, such as on Unnamed 2 and John Evans, have accelerated the development of supraglacial systems over the past ~60 years. Enhanced surface melt rates on John Evans are likely contributing to the greater importance of canyons to the total channel length compared to Unnamed 1 and greater overall D_d than Unnamed 2.

In situ incision measurements for supraglacial channels in the CAA are sparse. However, recent data from St. Germain and Moorman (2019) on Bylot Island report incision rates ranging from 0.06 m a^{-1} to 0.25 m a^{-1} for surface and incised channels during the period from 2010 to 2017, and reaching between 0.3 m a^{-1} and 2.5 m a^{-1} in canyon rivers. Converting the average summer losses on Sydkap Glacier for the period 2010-2019 from water equivalent to ice equivalent, using a density of 850 ± 60 kg/m³ (Huss, 2013), yields an annual summer ablation estimate of 1.09 m of ice for this period in the ablation area. Combined with the heavy crevassing which does not foster an environment for the formation of channels further down glacier, the surface ablation on Sydkap far exceeds the incision rates measured for surface and incised channels on Bylot Island, most likely limiting the formation of channels there beyond the crevasse field.

In the accumulation area, both mass gains (except for Unnamed 2) and losses show a significant ($p<0.05$) negative trend from 1964-2019, with losses increasing at a notably faster rate than gains (Figure 18f-l, Table 6b). This pattern, similar to that observed in the ablation area, suggests that changes in the supraglacial hydrological systems at higher elevations are primarily

driven by increased surface melt production. Between periods 1964-99 and 2000-19, losses have more than doubled for Sydkap and John Evans glaciers, more than tripled for Unnamed 2 Glacier, and increased by 10.5-fold on Henrietta-Nesmith Glacier (Table 7). This accelerated rate of change is consistent with the observed elevation-dependent warming across the glaciated regions of the QEI since the start of the 21st century, where the linear rate of change of clear-sky mean summer land surface temperature (°C a^{-1}) has been 40% greater at elevations above 1000 m and 76.9% greater at elevations above 1400 m (Mortimer and others, 2016).

The recent trends of increased losses combined with a slight but significant decrease in gains in the accumulation areas are contributing to an overall decline in cumulative mass balance. This suggests a future reduction in the accumulation area ratio as ablation zones shift to higher elevations and replace previous accumulation zones.

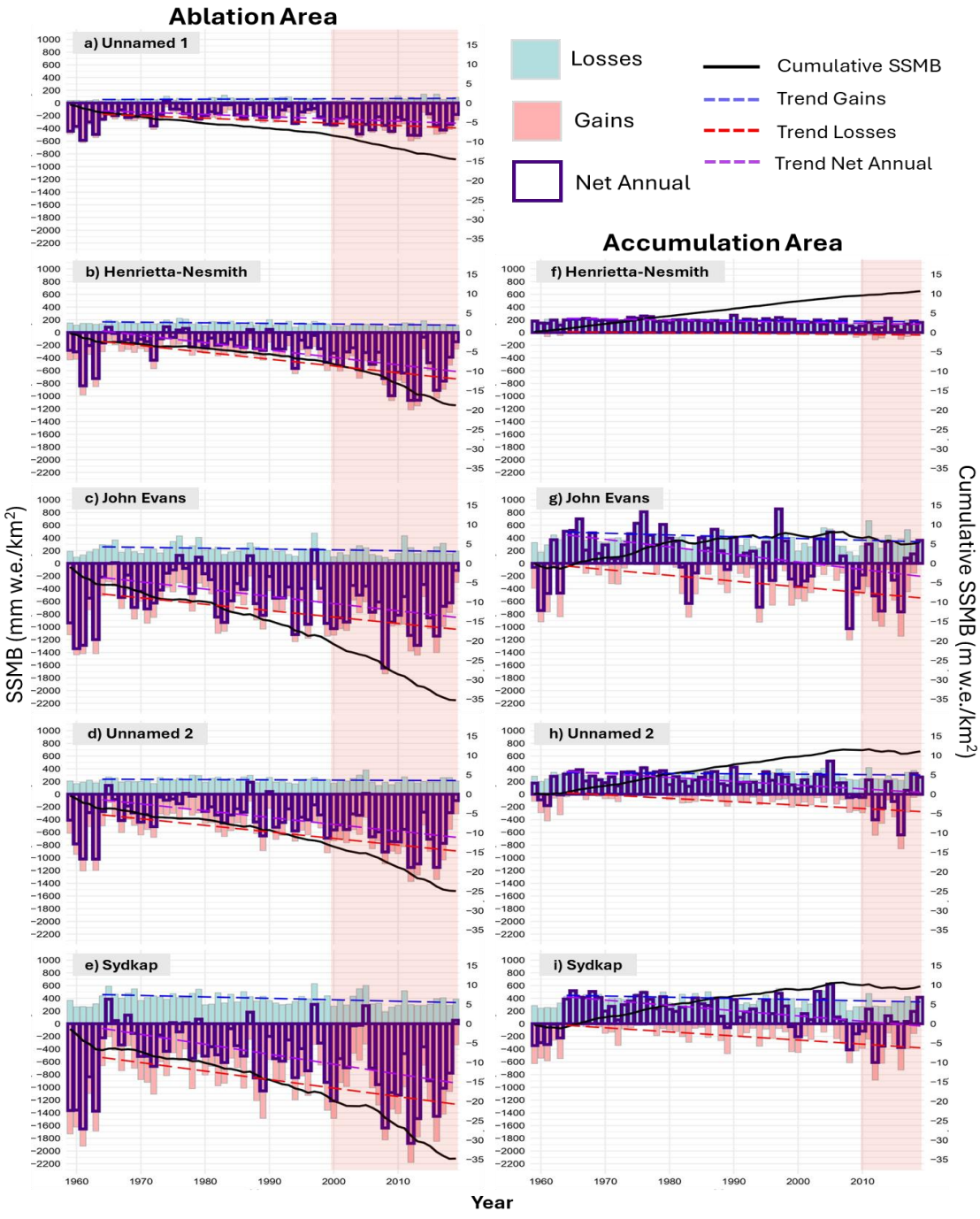

Figure 18. Annual Surface Mass Balance (SMB) components for the ablation (a-e) and accumulation (f-i) areas of the five studied glaciers from 1959 to 2019: Gains (blue), losses (pink), and net annual (purple outline), with trendlines from 1964 depicted in dark blue (gains), red (losses), and violet (net annual). Cumulative net SMB (black solid line) is shown on the secondary axis. SMB components for Unnamed 1 are not shown as this glacier's surface is now fully within the ablation zone. SMB values were derived from the regional climate model RACMO2.3 downscaled to 1 km resolution, and specific glacier values were computed by summing all raster values within the glacier area and dividing by the glacier's surface area.

Table 6. Rate of change (slope, θ) and significance values (p) for gains, losses and net annual SMB over the period 1964-2019 across the ablation (a) and accumulation (b) areas of the five studied glaciers, derived from the regional climate model RACMO2.3. Unnamed 1 was excluded from the accumulation area analysis as its surface area is now completely within the ablation zone.

Glacier	Gains		Losses		Net annual	
a) Ablation	θ	p	θ	p	θ	p
Unnamed 1	0.34	0.1	-3.88	4.1×10^{-5}	-3.54	0.0006
Henrietta-Nesmith	-0.94	0.0002	-10.67	$4.\times10^{-8}$	-11.61	2.6×10^{-8}
John Evans	-1.32	0.06	-10.06	0.00021	-11.39	0.0002
Unnamed 2	-0.4	0.2	-10.31	1.1×10^{-6}	-10.71	3.8×10^{-6}
Sydkap	-2.28	0.002	-13.35	0.0001	-15.63	5.7×10^{-5}
b) Accumulation						
Henrietta-Nesmith	-0.77	0.002	-0.92	$6.62\text{x}10^{-6}$	-1.69	$7.24\text{x}10^{-6}$
John Evans	-2.74	0.02	-9.09	0.0003	-11.82	0.0003
Unnamed 2	-0.67	0.2	-5.35	$8.3\text{x}10^{-6}$	-6.01	0.0001
Sydkap	-1.87	0.008	-6.43	$2.3\text{x}10^{-5}$	-8.31	$3\text{X}10^{-5}$

Table 7. Average losses (mm w.e./km^2/yr) used as a proxy of surface melt across the ablation (Ab) and accumulation (Ac) areas of the five studied glaciers over the 1959–2019 period, derived from the regional climate model RACMO2.3.

Year	Unnamed 1		Henrietta-Nesmith		John Evans		Unnamed 2		Sydkap	
	Ab	Ac	Ab	Ac	Ab	Ac	Ab	Ac	Ab	Ac
1960s	-337	N/A	-408	-12.5	-817	-299	-631	-128	-939	-208
1970s	-232	N/A	-267	-2.49	-549	-100	-407	-38	-720	-112
1980s	-215	N/A	-319	-3.84	-708	-288	-535	-89	-857	-180
1990s	-226	N/A	-365	-5.19	-746	-293	-581	-95	-837	-175
2000s	-388	N/A	-591	-18.8	-952	-403	-734	-142	-1021	-260
2010s	-386	N/A	-746	-50.3	-976	-516	-902	-325	-1288	-389
1964-99 average	-227	N/A	-305	-3.28	-644	-200	-491	-66	-756	-134
2000-19 average	-387	N/A	-668	-34.5	-964	-459	-818	-233	-1155	-324

2.5.2.2 Glacier Hypsometry and Changes in Equilibrium Line Altitude

The increasing rate of ice loss in the accumulation areas of the studied glaciers underscores their vulnerability and the potential for the expansion of the supraglacial channel network at higher elevations. Since 1959, this expansion has been evidenced by the development of incised rivers in regions that were previously part of the accumulation zone but have since

retreated. Even relatively minor changes in the ELA can shift large portions of glaciers from the accumulation zone to the ablation zone, facilitating the observed growth of the supraglacial channel networks.

Since 1960, the ELA has increased across all mapped glaciers, although there is considerable variability among them. On northern Ellesmere Island, the ELA has risen above the highest point of Unnamed 1 Glacier (>580 m), effectively removing its accumulation zone (Figure 19a). In 1959, this glacier had an accumulation area ratio (AAR) of 0.61. Since the bulk of the ice on this glacier is concentrated at lower to mid elevations (especially in the 400 m band), a 100 m rise above the 1960 ELA would have decreased the AAR to 0.28 (Figure 19a). According to Dyurgerov and others (2009), glaciers with balanced mass budgets typically have an AAR between 0.40 and 0.80. This suggests that Unnamed 1 would have been out of balance with the climate shortly after 1960, indicating a heightened vulnerability to further climatic changes and rapidly expanding the supraglacial system at higher elevations.

For Henrietta-Nesmith Glacier, the ELA increased by approximately 53 m between 1960 and 2020, increasing the AAR to 0.81 (Figure 19b). This observation, along with the increase for Unnamed 1, do not align with the previous estimate suggested by White and Copland (2018), which projected an ELA increase of approximately 100-300 m across northern Ellesmere Island between 1999 and 2015. Specifically, Henrietta-Nesmith Glacier falls below this estimate, highlighting the substantial variability in ELA changes among different glaciers.

Further south, the ELA on John Evans Glacier and Unnamed 2 Glacier has increased by approximately 89 and 145 m, respectively, since 1960 (Figure 19c and 19d). These changes have led to decreases in their AAR of 12.5% and 20.2%, respectively. Notably, these increases are lower than the average ELA change rate of 8 ± 2 m per year reported by Curley and others (2021) for eight smaller glaciers (areas between 0.88 and 26.46 km^2) at Alexandra Fiord, ~5-20 km east of Unnamed 2 Glacier, between 1974 and 2019. This degree of variability between different ice bodies with different sizes and hypsometries on Ellesmere Island highlights the importance of local studies of glacier change.

Given the variability in ELA among different glaciers, making separate projections for each glacier appears more appropriate than relying on regional estimates. If the ELA continues to rise

at the observed rates for these glaciers, the AAR—without considering reductions in glacier area—would be approximately 0.38 for Unnamed 2 Glacier, 0.46 for John Evans and 0.78 for Henrietta-Nesmith Glacier by 2080 (Figure 19b-d). Due to the large amount of ice concentrated between 1000-1200 m elevation on Unnamed 2 this rise in ELA would make this glacier out of balance with future climate conditions, resulting in accelerated rates of mass loss (Figure 20a). Unnamed 1 Glacier would continue to retreat, following trends observed in smaller glaciers and ice caps on Ellesmere Island with their surfaces below regional ELAs (Serreze and others, 2017; Medrzycka and others, 2023). Meanwhile, the proportion of the supraglacial hydrological system in the ablation areas of John Evans Glacier and Unnamed 2 Glacier would likely increase from 62.5% to 80.1% and from 82.7% to 94.6%, respectively with pronounced changes occurring near the ELA. Given the recent acceleration in the rate of change in SMB since the early 21st century, these estimates are likely conservative.

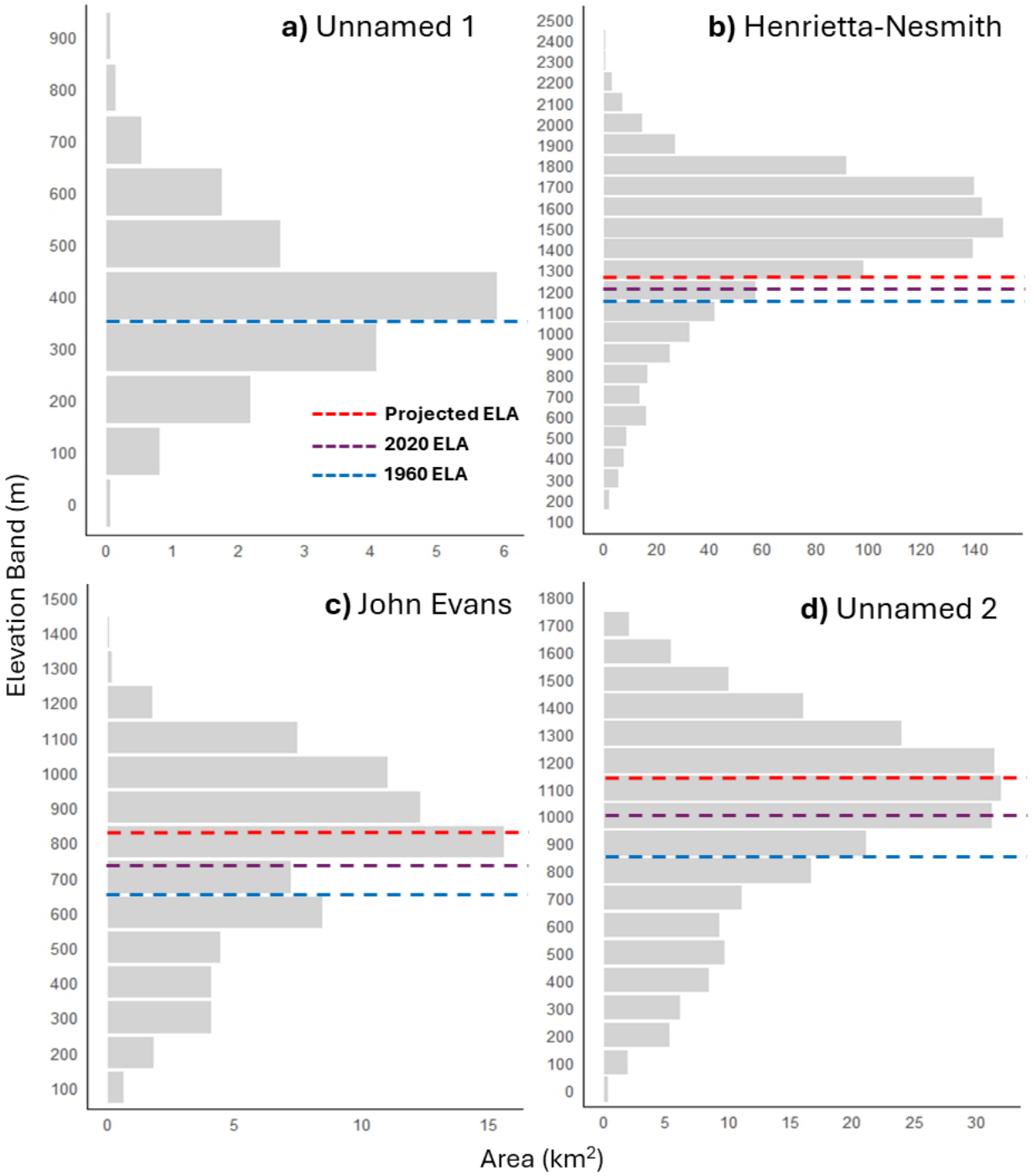

Figure 19. Glacier hypsometry for glaciers: a) Unnamed 1, b) Henrietta-Nesmith, c) John Evans and d) Unnamed 2. The ELA for each glacier in 1960 and 2020 is shown as the blue and purple dashed lines respectively, while the predicted ELA for ~2080 is shown as the red dashed line. Only the 1960 ELA was included for Unnamed 1 as the highest point on this glacier is now below the regional ELA.

2.5.3 Mapping Framework Assessment and Limitations

While recent studies of supraglacial hydrological networks have focused on mapping supraglacial hydrological features (Yang and Smith, 2013; Yang and others, 2015a; Yang and others, 2015b; King and others, 2016; Yang and others, 2017; Yang and others, 2018; Yang and others, 2019; Lu and others, 2020, Bash and others, 2022; Rawlins and others, 2023), no single method has been universally accepted as the best approach. The choice of methodology typically depends on the study's specific objectives and context. In this study, we employed a manual approach to map supraglacial channels and sink points. While this method can introduce user bias (King and others, 2016; Bash and others, 2022), it remains the standard for evaluating semi-automated and fully automated techniques (Yang and Smith, 2013; King and others, 2016; Lu and others, 2020; Bash and others, 2022), currently making it the most reliable approach.

Given the scale of the glaciers examined (basin level), the manual method was deemed the most appropriate for our needs. The validity of doing this can be evaluated by comparing our manually mapped channels from John Evans Glacier to outputs from the widely used 'channel model', a DEM-based hydrologic approach that utilizes the D8 flow routing algorithm available in various GIS software (e.g., ArcGIS, QGIS) (Yang and others, 2015b; King and others, 2016; Yang and others, 2018; Bash and others, 2022). This approach provides a theoretical representation of flow pathways, which may not necessarily correspond to actual streams and rivers. Although the stream model effectively captures the overall drainage pattern, the resolution of the ArcticDEM is insufficient for detecting most surface streams on John Evans Glacier due to their shallow valleys (Appendix, Figure 3-A). Even in large-scale studies such as those on the GrIS, the stream model underestimates first-order channels so that these smaller channels were only matched at 65% (King and others, 2016). Similar to Lu and others (2020), the model also tends to overestimate high elevation channels, following larger depressions that are not necessarily active channels (Appendix, Figure 3-A). Additionally, the model does not account for sinks, as these are filled during the model-building phase, so moulins/sinks still need to be identified manually (Appendix, Figure 3-A).

These limitations render this approach unsuitable for our analysis as changes cannot be appropriately quantified over time. Bash and others (2022) proposed a Normalized Difference

Water Index for ice ($NDWI_{ice}$) model to detect smaller channels not captured by the DEM, but in testing we found that this model performed poorly in low-contrast areas, making visual inspection of imagery a more reliable method for identifying surface channels. Similarly, the index-based $NDWI_{ice}$ method suggested by Yang and others (2019) was found to underestimate the total length of channels by 13% on the GrIS (Lu and others, 2020). In addition, such methods complicate comparisons between different datasets, such as between panchromatic air photos and PlanetScope multispectral images, due to the inability to calculate band ratios for panchromatic imagery.

Our validation of sink identification using different WorldView imagery showed that sinks identified in PlanetScope images aligned well with those in WorldView images, despite a two-year difference in acquisition time between them (2020 vs 2022; Table 2). Channels further up-glacier that appeared to abruptly end in the PlanetScope imagery often transitioned into distributed systems. While these distributed systems were visible in the PlanetScope imagery, their discontinuous nature prevented them from being accurately mapped. Consequently, channels that seem to terminate abruptly but lack mapped sinks at their endpoints are often a result of this issue.

Based on the above evaluations and available data, the manual mapping framework developed in this study proved to be the most reliable and consistent method for quantifying supraglacial drainage networks over time. However, this approach has inherent limitations, particularly due to the subjectivity involved in image interpretation. To address this, we provided clear definitions and examples for each step of the mapping process. We also acknowledge that using different datasets for 1959 (panchromatic aerial photos) and 2020 (multispectral imagery), along with differing methodologies (due to the lack of topographic data in 1959), may affect the comparability of the results between these years. For instance, the panchromatic aerial photos have a bit depth of 8, while the multispectral PlanetScope images have a bit depth of 16 per channel (band). The higher bit depth of the multispectral images allows for a broader range of detail and color compared to the panchromatic photos, thereby improving the accuracy of feature detection and mapping. Additionally, the framework relies on high-resolution optical data, which

is not available for the period between 1959 and 2020, limiting the ability to perform repetitive, multidecadal quantitative analyses.

2.6 Summary and Conclusion

In this study we examined and quantified supraglacial drainage patterns for five different glaciers on Ellesmere Island using remote sensing methods, providing the first comprehensive spatiotemporal assessment of changes in supraglacial hydrology in the NCAA.

Drainage patterns across different glacier basins are similar, influenced by variations in surface topography that affect channelization and sinuosity. Substantial increases in D_d have occurred across most glacier surfaces between 1959 and 2020, primarily driven by the expansion of perennial incised and canyon rivers, particularly at higher elevations, and the increase in channel density. As a result, long-term changes in the supraglacial systems show a reorganization of channel types across the glacier surfaces towards present day, with incised rivers becoming the most dominant and canyons contributing more to the total channel length. The expansion of incised rivers is especially important in areas corresponding to the retreat of the ELA, such as the entire upper half of Unnamed 1 Glacier on far northern Ellesmere Island. Unnamed 1 has also experienced increased channelization of its already established perennial system, with sinuous canyons showing an overall trend toward straighter channels and numerous small surface streams consolidating into fewer larger rivers. Compared to Unnamed 1, canyon development has been more pronounced in the lower ablation areas of Unnamed 2 and John Evans glaciers.

The limited number of sinks, absence of crevasses, formation of numerous cut-and-closure channels, and deeply incised supraglacial lakes on Unnamed 1 Glacier suggests the presence of extensive cold ice near the glacier surface. This results in an extensive supraglacial drainage system with high D_d, dominated by the high abundance of canyon and incised rivers. Similarly, low moulin count, limited crevasses, and high canyon D_d on Henrietta-Nesmith Glacier suggest a similar cold ice pattern in the ablation area, consistent with modelling of glacier temperatures elsewhere on northern Ellesmere Island (Kochtitzky and others, 2023). On more southerly glaciers on Ellesmere Island, extensive moulin fields suggest better connectivity between supraglacial and subglacial systems, affecting the development of the subglacial

drainage system and glacier velocity and resulting in basal and internal temperatures which can reach the pressure melting point, as previously shown on John Evans Glacier (Bingham and others, 2008; Wohlleben and others, 2011).

The lack of significant change in sinuosity on the studied glaciers, combined with evidence of channel dynamism, such as meander cutoffs on Unnamed 2, indicates that canyons are at different stages of evolution. The wide range of sinuosity values also suggests that other hydraulic factors, such as surface slope and watershed area (affecting discharge), play an important role in meander development and overall sinuosity (St. Germain and Moorman, 2019). This was also observed further north on Henrietta-Nesmith Glacier, where the larger glacier surface area likely results in greater watershed areas for canyons, increasing discharge and dynamism compared to the smaller Unnamed 1 Glacier.

The above findings are consistent with modelled increases in surface melt production across the different glaciers, which are generally higher for glaciers further south and lower for glaciers further north (Noël and others, 2018). Specifically, when combined with greater ice velocities and extensive crevasse fields, higher surface melt production on Sydkap Glacier likely contributes to the lack of a perennial surface hydrological system, in contrast to the well-developed system on Unnamed 1. In addition, compared to Unnamed 1, other glaciers show greater rates of mass loss since the mid-1960s, indicating greater stability on glaciers in far northern areas, such as Unnamed 1. However, losses have accelerated since the start of the 21st century, with high melt rates in the last decade likely influencing the greater rates of change recently observed in the multi-decadal time series for all mapped glaciers. The ELA on each glacier will likely continue to rise in the future as the climate continues to warm, making glaciers such as Unnamed 2, which have the bulk of their ice at mid elevations, vulnerable to enhanced melt across a larger surface area, likely expanding the supraglacial system.

These findings suggest the importance of surface melt as a primary control on the development of supraglacial hydrological systems on glaciers on Ellesmere Island. Specifically, the negative SMB trend is mainly driven by summer losses, implying greater surface melt production over the study period. High rates of melt increase runoff on glaciers further south, leading to the rapid expansion and dynamic nature of supraglacial systems on glaciers such as Unnamed 2 and

John Evans (Lu and others, 2020). In contrast, lower melt rates in far northern areas have facilitated the stability of the supraglacial network on Unnamed 1, with changes mostly resulting from incision (Rippin and others, 2015). In the future, the supraglacial drainage systems of glaciers Unnamed 2, John Evans, and Henrietta-Nesmith will likely continue to expand as climate change in the CAA continues to enhance surface melt. Although NCAA glaciers can still buffer most of the melt in their accumulation areas due to the presence of perennial firn (Noël and others, 2018), trends observed on glaciers such as John Evans, which has 37.5% of its supraglacial system within the accumulation area, indicate a shift toward enhanced melt and associated runoff at higher elevations. While the supraglacial system on Unnamed 1 is likely to continue expanding at higher elevations, the pattern of glacier retreat, as observed in its important reduction in area over the study period, will lead to the eventual disappearance of this small glacier, similar to the complete loss of other small glaciers and ice caps with AARs of 0 already observed on northern Ellesmere Island (Serreze and others, 2017; White and Copland, 2018; Medrzycka and others, 2023).

Although this thesis has made considerable advancements in understanding the long-term development of different supraglacial systems, it did not explicitly relate the observed changes and differences across the glaciers to climatic variations that may affect their environmental settings and patterns of change. This is especially important considering the latitudinal gradient in temperature across Ellesmere Island as well as the glaciers' position relative to the coast and overall elevation gradient, which may also affect temperature and patterns of precipitation (Koerner, 1979). Future studies should aim to interpret these changes by correlating them with climatic data, including temperature and precipitation patterns. This approach will deepen our understanding of the variations between systems and their potential responses to future climate changes.

References

Arnold, N., Willis, I., Sharp, M., Richards, K., and Lawson, W. A. (1996). A distributed surface energy-balance model for a small valley glacier. I. Development and testing for Haut Glacier d'Arolla, Valais, Switzerland. *Journal of Glaciology*, *42*(140), 77–89. https://doi.org/10.1017/s0022143000030549

Bash, E. A., Shellian, C., Dow, C. F., Mcdermid, G., Kochtitzky, W. H., Medrzycka, D., and Copland, L. (2022). A semi-automated, GIS-based framework for the mapping of supraglacial hydrology. *Journal of Glaciology*, 1–15. https://doi.org/10.1017/jog.2022.92

Benn, D.I. and Evans, D.J.A. (2010). *Glaciers and Glaciations* (2nd ed). London: Hodder Education.

Bennett, M. and Glasser, N. (2009). *Glacial Geology; Ice sheets and Landforms* (2nd ed): Chichester, UK; Hoboken, NJ: Wiley-Blackwell.

Bergsma, B., Svoboda, J., and Freedman, B. (1984). Entombed Plant Communities Released by a Retreating Glacier at Central Ellesmere Island, Canada. *Arctic*, *37*(1). https://doi.org/10.14430/arctic2162

Bingham, R.G., Hubbard, A.L., Nienow, P.W. and Sharp, M.J. (2008). An investigation into the mechanisms controlling seasonal speed-up events at a High Arctic glacier. J. *Geophys. Res., 113*(F2), F02006. https://doi.org/10.1029/2007JF000832

Bingham, R. G., Nienow, P. W., and Sharp, M. J. (2003). Intra-annual and intra-seasonal flow dynamics of a High Arctic polythermal valley glacier. *Annals of Glaciology*, *37*, 181–188. https://doi.org/10.3189/172756403781815762

Bingham, R., Nienow, P., Sharp, M., and Boon, S. (2005). Subglacial drainage processes at a High Arctic polythermal valley glacier. *Journal of Glaciology*, *51*(172), 15–24. https://doi.org/10.3189/172756505781829520

Bingham, R., Nienow, P., Sharp, M., and Copland, L. (2006). Hydrology and dynamics of a polythermal (mostly cold) High Arctic glacier. *Earth Surface Processes and Landforms*, *31*(12), 1463–1479. https://doi.org/10.1002/esp.1374

Blatter, H. (1987). On the Thermal Regime of an Arctic Valley Glacier: A Study of White Glacier, Axel Heiberg Island, N.W.T., Canada. *Journal of Glaciology*, *33*(114), 200–211. https://doi.org/10.1017/s0022143000008704

Casey, J. A., and Kelly, R. E. (2010). Estimating the equilibrium line of Devon Ice Cap, Nunavut, from RADARSAT-1 ScanSAR wide imagery. *Canadian Journal of Remote Sensing*, *36*(sup1), S41–S55. https://doi.org/10.5589/m10-013

Cavaco, M., St Louis, V. L., Engel, K., St Pierre, K. A., Schiff, S. L., Stibal, M., and Neufeld, J. D. (2019). Freshwater microbial community diversity in a rapidly changing High Arctic watershed. *FEMS Microbiology Ecology*, *95*(11). https://doi.org/10.1093/femsec/fiz161

Charlton, R. (2007). Fundamentals of fluvial Geomorphology. In *Routledge eBooks*. https://doi.org/10.4324/9780203371084

Chu, V. W. (2014). Greenland ice sheet hydrology. *Progress in Physical Geography, 38*(1), 19–54. https://doi.org/10.1177/0309133313507075

Ciracì, E., Velicogna, I., and Swenson, S. (2020). Continuity of the Mass Loss of the World's Glaciers and Ice Caps from the GRACE and GRACE Follow-On Missions. *Geophysical Research Letters, 47*(9). https://doi.org/10.1029/2019gl086926

Copland, L., Sharp, M., and Dowdeswell, J. A. (2003a). The distribution and flow characteristics of surge-type glaciers in the Canadian High Arctic. *Annals of Glaciology, 36*, 73–81. https://doi.org/10.3189/172756403781816301

Copland, L., Sharp, M., and Nienow, P. (2003b). Links between short-term velocity variations and the subglacial hydrology of a predominantly cold polythermal glacier. *Journal of Glaciology, 49*(166), 337–348. https://doi.org/10.3189/172756503781830656

Copland, L., Sharp, M. J., Nienow, P., & Bingham, R. G. (2003). The distribution of basal motion beneath a High Arctic polythermal glacier. *Journal of Glaciology, 49*(166), 407–414. https://doi.org/10.3189/172756503781830511

Crozier, J., Karlstrom, L., and Yang, K. (2018). Basal control of supraglacial meltwater catchments on the Greenland Ice Sheet. *The Cryosphere, 12*(10), 3383–3407. https://doi.org/10.5194/tc-12-3383-2018

Cuffey K, Paterson WSB. 2010. *The Physics of Glaciers*. Burlington, MA: Elsevier. 4th ed.

Curley, A., Kochtitzky, W. H., Edwards, B., and Copland, L. (2021). Glacier changes over the past 144 years at Alexandra Fiord, Ellesmere Island, Canada. *Journal of Glaciology*, *67*(263), 511–522. https://doi.org/10.1017/jog.2021.4

Dozier, J. (1974). Channel adjustment in supraglacial streams. *Icefield Ranges Research Project Scientific Results, 4*, 189–199.

Dyurgerov, M., Meier, M. F., & Bahr, D. B. (2009). A new index of glacier area change: a tool for glacier monitoring. *Journal of Glaciology/Journal of Glaciology*, *55*(192), 710–716. https://doi.org/10.3189/002214309789471030

Flowers, G. E. (2015). Modelling water flow under glaciers and ice sheets. *Proceedings of the Royal Society A: Mathematical, Physical and Engineering Sciences, 471*(2176), 20140907. https://doi.org/10.1098/rspa.2014.0907

Fountain, A. G., and Walder, J. S. (1998). Water flow through temperate glaciers. *Reviews of Geophysics, 36*(3), 299–328. https://doi.org/10.1029/97rg03579

Ferguson, R. I. (1973). Sinuosity of supraglacial streams. *The Geological Society of America Bulletin/Geological Society of America Bulletin*, *84*(1), 251. https://doi.org/10.1130/0016-7606(1973)84

Gardner, A. S., Moholdt, G., Cogley, J. G., Wouters, B., Arendt, A., Wahr, J., Berthier, E., Hock, R., Pfeffer, W. T., Kaser, G., Ligtenberg, S. R. M., Bolch, T., Sharp, M., Hagen, J. O., Van Den Broeke, M. R., and Paul, F. (2013). A Reconciled Estimate of Glacier Contributions to Sea Level Rise: 2003 to 2009. *Science, 340*(6134), 852–857. https://doi.org/10.1126/science.1234532

Gardner, A. S., Moholdt, G., Wouters, B., Wolken, G. J., Burgess, D. S., Sharp, M., Cogley, J. G., Braun, C., and Labine, C. (2011). Sharply increased mass loss from glaciers and ice caps in the Canadian Arctic Archipelago. *Nature, 473*(7347), 357–360. https://doi.org/10.1038/nature10089

Kusratmoko, E., Wibowo, A., and Kurnia, A. A. (2019). Changes in the value of sinuosity index in Komering River Channel, Province South Sumatera years 1990 - 2016. *IOP Conference Series Earth and Environmental Science*, *338*(1), 012024. https://doi.org/10.1088/1755-1315/338/1/012024

Gulley, J. L., Benn, D. I., Muller, D. R., and Luckman, A. (2009). A cut-and-closure origin for englacial conduits in uncrevassed regions of polythermal glaciers. *Journal of Glaciology, 55*(189), 66–80. https://doi.org/10.3189/002214309788608930

Hattersley-Smith, G. (1961). THE ICE COVER OF NORTHERN ELLESMERE ISLAND. *Annals of the New York Academy of Sciences*, *95*(1), 282–289. https://doi.org/10.1111/j.1749-6632.1961.tb50039.x

Hock, R. (2005). Glacier melt: a review of processes and their modelling. *Progress in Physical Geography, 29(*3), 362–391. https://doi.org/10.1191/0309133305pp453ra

Huss, M. (2013). Density assumptions for converting geodetic glacier volume change to mass change. *The Cryosphere*, *7*(3), 877–887. https://doi.org/10.5194/tc-7-877-2013

Ignéczi, Á., Sole, A. J., Livingstone, S. J., Ng, F. S. L., & Yang, K. (2018). Greenland Ice sheet surface topography and drainage structure controlled by the transfer of basal variability. *Frontiers in Earth Science*, *6*. https://doi.org/10.3389/feart.2018.00101

Iken, A (1974) Velocity fluctuations of an arctic valley glacier, A study of the White Glacier, Axel Heiberg Island, Canadian Arctic Archipelago. *Axel Heiberg Island Research Reports, Glaciology, No. 5*, 123. McGill University, Montreal.

Irvine-Fynn, T., Hodson, A., Moorman, B. J., Vatne, G., and Hubbard, A. (2011). POLYTHERMAL GLACIER HYDROLOGY: A REVIEW. *Reviews of Geophysics, 49*(4). https://doi.org/10.1029/2010rg000350

Isenko, E., Naruse, R., & Mavlyudov, B. (2005). Water temperature in englacial and supraglacial channels: Change along the flow and contribution to ice melting on the channel wall. *Cold Regions Science and Technology*, *42*(1), 53–62. https://doi.org/10.1016/j.coldregions.2004.12.003

Karlstrom, L., and Yang, K. (2016). Fluvial supraglacial landscape evolution on the Greenland Ice Sheet. *Geophysical Research Letters*, *43*(6), 2683–2692. https://doi.org/10.1002/2016gl067697

Karlstrom, L., Gajjar, P., and Manga, M. (2013). Meander formation in supraglacial streams. *Journal of Geophysical Research: Earth Surface, 118*(3), 1897–1907. https://doi.org/10.1002/jgrf.20135

King, L., Hassan, M. A., Yang, K., and Flowers, G. E. (2016). Flow Routing for Delineating Supraglacial Meltwater Channel Networks. *Remote Sensing, 8*(12), 988. https://doi.org/10.3390/rs8120988

Knighton, A. D. (1981). Channel Form and Flow Characteristics of Supraglacial Streams, Austre Okstindbreen, Norway. *Arctic and Alpine Research*, *13*(3), 295. https://doi.org/10.2307/1551036

Kochtitzky, W., Copland, L., Wohlleben, T., Iqaluk, P., Girard, C., Vincent, W. F., and Culley, A. I. (2023). Slow change since the Little Ice Age at a far northern glacier with the potential for system reorganization: Thores Glacier, northern Ellesmere Island, Canada. *Arctic Science*, *9*(2), 451–464. https://doi.org/10.1139/as-2022-0012

Koerner, R. M. (1979). Accumulation, Ablation, and Oxygen Isotope Variations on the Queen Elizabeth Islands Ice Caps, Canada. *Journal of Glaciology*, *22*(86), 25–41. https://doi.org/10.1017/s0022143000014039

Lampkin, D. J., and VanderBerg, J. (2014). Supraglacial melt channel networks in the Jakobshavn Isbrae region during the 2007 melt season. *Hydrol. Process. 24*(28), 6038–6053. https://doi.org/10.1002/hyp.10085

Lenaerts, J. T. M., Van Angelen, J. H., Van Den Broeke, M. R., Gardner, A. S., Wouters, B., and Van Meijgaard, E. (2013). Irreversible mass loss of Canadian Arctic Archipelago glaciers. *Geophysical Research Letters, 40*(5), 870–874. https://doi.org/10.1002/grl.50214

Lu, Y., Yang, K., Lu, X., Smith, L. C., Sole, A., Clark, C. D., Fettweis, X., and Li, M. (2020). Diverse supraglacial drainage patterns on the Devon ice Cap, Arctic Canada. *Journal of Maps, 16*(2), 834–846. https://doi.org/10.1080/17445647.2020.1838353

Mantelli, E., Camporeale, C., and Ridolfi, L. (2015). Supraglacial channel inception: Modeling and processes. *Water Resources Research*, *51*(9), 7044–7063. https://doi.org/10.1002/2015wr017075

Marston, R. C. (1983). Supraglacial Stream Dynamics on the Juneau Icefield. *Annals of the Association of American Geographers*, *73*(4), 597–608. https://doi.org/10.1111/j.1467-8306.1983.tb01861.x

Medrzycka, D., Copland, L., and Noël, B. (2023). Rapid demise and committed loss of Bowman Glacier, northern Ellesmere Island, Arctic Canada. *Journal of Glaciology*, *69*(276), 997–1010. https://doi.org/10.1017/jog.2022.119

Millan, R., Mouginot, J., and Rignot, E. (2017). Mass budget of the glaciers and ice caps of the Queen Elizabeth Islands, Canada, from 1991 to 2015. *Environmental Research Letters, 12*(2), 024016. https://doi.org/10.1088/1748-9326/aa5b04

Miller, G. H., Bradley, R. S., and Andrews, J. T. (1975). The glaciation level and lowest equilibrium line altitude in the High Canadian Arctic: Maps and Climatic interpretation. *Arctic and Alpine Research*, *7*(2), 155. https://doi.org/10.2307/1550318

Mortimer, C., and Sharp, M. (2018). Spatiotemporal variability of Canadian High Arctic glacier surface albedo from MODIS data, 2001–2016. *The Cryosphere*, *12*(2), 701–720. https://doi.org/10.5194/tc-12-701-2018

Mortimer, C., Sharp, M., and Wouters, B. (2016). Glacier surface temperatures in the Canadian High Arctic, 2000–15. *Journal of Glaciology, 62*(235), 963–975. https://doi.org/10.1017/jog.2016.80

Müller, D. (2007). Incision and closure processes of meltwater channels on the glacier Longyearbreen, Spitbergen, M.S. thesis, 118 pp., Tech. Univ. Braunschweig/Univ. Cent., Svalbard, Norway.

Müller, F., and Iken, A. (1973) Velocity fluctuations and water regime of Arctic valley glaciers. *Symposium on the Hydrology of Glaciers, Cambridge, de l'Association Internationale d'Hydrologie Scientifique*, 165–182.

Nienow, P., Sole, A., Slater, D., and Cowton, T. (2017). Recent Advances in Our Understanding of the Role of Meltwater in the Greenland Ice Sheet System. *Current Climate Change Reports*, *3*(4), 330–344. https://doi.org/10.1007/s40641-017-0083-9

Noël, B., van de Berg, W. J., Lhermitte, S., Wouters, B., Schaffer, N., and van den Broeke, M. R. (2018). Six decades of glacial mass loss in the Canadian Arctic Archipelago. *Journal of Geophysical Research: Earth Surface, 123*, 1430–1449. https://doi.org/10.1029/2017JF004304

Pellicciotti, F., Brock, B., Strasser, U., Burlando, P., Funk, M., and Corripio, J. G. (2005). An enhanced temperature-index glacier melt model including the shortwave radiation balance: development and testing for Haut Glacier d'Arolla, Switzerland. *Journal of Glaciology, 51*(175), 573–587. https://doi.org/10.3189/172756505781829124

Phillips, E., Finlayson, A., and Jones, L. (2013). Fracturing, block faulting, and moulin development associated with progressive collapse and retreat of a maritime glacier: Falljökull, SE Iceland. *Journal of Geophysical Research. Earth Surface*, *118*(3), 1545–1561. https://doi.org/10.1002/jgrf.20116

Pitcher, L. H., and Smith, L. C. (2019). Supraglacial Streams and Rivers. *Annual Review of Earth and Planetary Sciences, 47*(1), 421–452. https://doi.org/10.1146/annurev-earth-053018-060212

Rantanen, M., Karpechko, A. Y., Lipponen, A., Nordling, K., Hyvärinen, O., Ruosteenoja, K., Vihma, T., and Laaksonen, A. (2022). The Arctic has warmed nearly four times faster

than the globe since 1979. *Communications Earth and Environment, 3*(1). https://doi.org/10.1038/s43247-022-00498-3

Rawlins, L. D., Rippin, D. M., Sole, A. J., Livingstone, S. J., and Yang, K. (2023) Seasonal evolution of the supraglacial drainage network at Humboldt Glacier, North Greenland, between 2016 and 2020, *The Cryosphere Discuss*. [preprint], https://doi.org/10.5194/tc-2023-23, in review, 2023.

Rippin, D. M., Pomfret, A., and King, N. (2015). High resolution mapping of supra-glacial drainage pathways reveals link between micro-channel drainage density, surface roughness and surface reflectance. *Earth Surface Processes and Landforms, 40*(10), 1279–1290. https://doi.org/10.1002/esp.3719

Ryser, C., Lüthi, M., Blindow, N., Suckro, S., Funk, M., and Bauder, A. (2013). Cold ice in the ablation zone: Its relation to glacier hydrology and ice water content. *Journal of Geophysical Research. Earth Surface*, *118*(2), 693–705. https://doi.org/10.1029/2012jf002526

Schaffer, N., Copland, L., and Zdanowicz, C. (2017). Ice velocity changes on Penny Ice Cap, Baffin Island, since the 1950s. *Journal of Glaciology/Journal of Glaciology*, *63*(240), 716–730. https://doi.org/10.1017/jog.2017.40

Schoof, C. (2010). Ice-sheet acceleration driven by melt supply variability. *Nature, 468*(7325), 803–806. https://doi.org/10.1038/nature09618

Serreze, M. C., Raup, B., Braun, C., Hardy, D. R., and Bradley, R. S. (2017). Rapid wastage of the Hazen Plateau ice caps, northeastern Ellesmere Island, Nunavut, Canada. *The Cryosphere*, *11*(1), 169–177. https://doi.org/10.5194/tc-11-169-2017

Sharp, M., Burgess, D.O., Cawkwell, F., Copland, L., Davis, J.A., Dowdeswell, E.K., Dowdeswell, J.A., Gardner, A.S., Mair, D., Wang, L., Williamson, S.N., Wolken, G. J. and Wyatt, F. (2014): Remote sensing of recent glacier changes in the Canadian Arctic. In: Kargel, J.S., Leonard, G.J., Bishop, M.P., Kääb, A. and Raup, B.H. (eds). *Global Land Ice Measurements from Space*, Ch. 9, pp. 205-228. Praxis-Springer. doi: 10.1007/978-3-540-79818-7_9.

Smith, C. N. G., Kochtitzky, W. H., Edwards, B. S., Copland, L., Ruff, I., Bresnahan, W., Noonan, P. K., Felknor-Edwards, K., and Aoid, H. (2020). 2020 Dickinson Hackweek: Sixty-year record of ice area loss from the marine terminating Sydkap Glacier, southern Ellesmere Island, Nunavut, Canada. *AGU Fall Meeting Abstracts*, *2020*. https://ui.adsabs.harvard.edu/abs/2020AGUFMC038.0004S/abstract

Smith, L. C., Andrews, L. J., Pitcher, L. H., Overstreet, B. T., Rennermalm, A. K., Cooper, M. E., Cooley, S., Ryan, J. C., Miège, C., Kershner, C., and Simpson, C. S. (2021). Supraglacial River Forcing of Subglacial Water Storage and Diurnal Ice Sheet Motion. *Geophysical Research Letters, 48*(7). https://doi.org/10.1029/2020gl091418

Smith, L. C., Chu, V. W., Yang, K., Gleason, C. J., Pitcher, L. H., Rennermalm, A. K., Legleiter, C. J., Behar, A., Overstreet, B. T., Moustafa, S., Tedesco, M., Forster, R. K., LeWinter, A. L., Finnegan, D. J., Sheng, Y., and Balog, J. (2015). Efficient meltwater drainage through supraglacial streams and rivers on the southwest Greenland ice sheet. *Proceedings of the National Academy of Sciences*, *112*(4), 1001–1006. https://doi.org/10.1073/pnas.1413024112

St. Germain, S. L., and Moorman, B. J. (2019). Long-term observations of supraglacial streams on an Arctic glacier. *Journal of Glaciology, 65*(254), 900–911. https://doi.org/10.1017/jog.2019.60

St. Germain, S. L., and Moorman, B. J. (2016). The development of a pulsating supraglacial stream. *Annals of Glaciology, 57*(72), 31–38. https://doi.org/10.1017/aog.2016.16

Tedstone, A. J., Nienow, P., Gourmelen, N., Dehecq, A., Goldberg, D. E., and Hanna, E. (2015). Decadal slowdown of a land-terminating sector of the Greenland Ice Sheet despite warming. *Nature*, *526*(7575), 692–695. https://doi.org/10.1038/nature15722

Thomson, L. and Copland, L. (2018). Changing contribution of peak velocity events to annual velocities following a multi-decadal slowdown at White Glacier. *Annals of Glaciology*, 58(75pt2), 145-154. https://doi.org/10.1017/aog.2017.46

Thomson, L., and Copland, L. (2017). Multi-decadal reduction in glacier velocities and mechanisms driving deceleration at polythermal White Glacier, Arctic Canada. *Journal of Glaciology, 63*(239), 450–463. https://doi.org/10.1017/jog.2017.3

Van De Wal, R. S. W., Boot, W., Van Den Broeke, M. R., Smeets, C. J. P. P., Reijmer, C., Donker, J., and Oerlemans, J. (2008). Large and Rapid Melt-Induced Velocity Changes in the Ablation Zone of the Greenland Ice Sheet. *Science, 321*(5885), 111–113. https://doi.org/10.1126/science.1158540

Van Wychen, W., Copland, L., Burgess, D. (2020). Ice Masses of the Eastern Canadian Arctic Archipelago. In: Slaymaker, O., Catto, N. (eds) *Landscapes and Landforms of Eastern Canada. World Geomorphological Landscapes* (p.297-314). Springer, Cham. https://doi.org/10.1007/978-3-030-35137-3_13

Vaughan, D.G., J.C. Comiso, I. Allison, J. Carrasco, G. Kaser, R. Kwok, P. Mote, T. Murray, F. Paul, J. Ren, E. Rignot, O. Solomina, K. Steffen and T. Zhang, 2013: Observations: Cryosphere. In: *Climate Change 2013: The Physical Science Basis. Contribution of Working Group I to the Fifth Assessment Report of the Intergovernmental Panel on Climate Change* [Stocker, T.F., D. Qin, G.-K. Plattner, M. Tignor, S.K. Allen, J. Boschung, A. Nauels, Y. Xia, V. Bex and P.M. Midgley (eds.)]. Cambridge University Press, Cambridge, United Kingdom and New York, NY, USA.

White, A. A., and Copland, L. (2018). Area change of glaciers across Northern Ellesmere Island, Nunavut, between ~1999 and ~2015. *Journal of Glaciology*, *64*(246), 609–623. https://doi.org/10.1017/jog.2018.49

Wohlleben, T., Sharp, M., & Bush, A. (2009). Factors influencing the basal temperatures of a High Arctic polythermal glacier. *Annals of Glaciology*, *50*(52), 9–16. https://doi.org/10.3189/172756409789624210

Williamson, S., Copland, L., Thomson, L., and Burgess, D. S. (2020a). Comparing simple albedo scaling methods for estimating Arctic glacier mass balance. *Remote Sensing of Environment*, *246*, 111858. https://doi.org/10.1016/j.rse.2020.111858

Wolken, G. J., England, J. H., and Dyke, A. S. (2008). Changes in late-Neoglacial perennial snow/ice extent and equilibrium-line altitudes in the Queen Elizabeth Islands, Arctic Canada. *The Holocene*, *18*(4), 615–627. https://doi.org/10.1177/0959683608089215

Wyatt, F., and Sharp, M. (2015). Linking surface hydrology to flow regimes and patterns of velocity variability on Devon Ice Cap, Nunavut. *Journal of Glaciology, 61*(226), 387–399. https://doi.org/10.3189/2015jog14j109

Yang, K., Karlstrom, L., Smith, L. C., and Li, M. (2017). Automated High-Resolution Satellite Image Registration Using Supraglacial Rivers on the Greenland Ice Sheet. *IEEE Journal of Selected Topics in Applied Earth Observations and Remote Sensing, 10(*3), 845–856. https://doi.org/10.1109/jstars.2016.2617822

Yang, K., Li, M., Liu, Y., Cheng, L., Huang, Q., and Chen, Y. (2015a). River Detection in Remotely Sensed Imagery Using Gabor Filtering and Path Opening. *Remote Sensing,* 7(7), 8779–8802. https://doi.org/10.3390/rs70708779

Yang, K., Smith, L. C., Chu, V. W., Gleason, C. J., and Li, M. (2015b). A Caution on the Use of Surface Digital Elevation Models to Simulate Supraglacial Hydrology of the Greenland Ice Sheet. *IEEE Journal of Selected Topics in Applied Earth Observations and Remote Sensing, 8*(11), 5212–5224. https://doi.org/10.1109/jstars.2015.2483483

Yang, K., Smith, L. C., Karlstrom, L., Cooper, M. E., Tedesco, M., Van As, D., Cheng, X., Chen, Z., and Li, M. (2018). A new surface meltwater routing model for use on the Greenland Ice Sheet surface. *The Cryosphere*, *12*(12), 3791–3811. https://doi.org/10.5194/tc-12-3791-2018

Yang, K., Smith, L. C., Sole, A., Clark, C. D., Cheng, X., Chen, Z., and Li, M. (2019). Supraglacial rivers on the northwest Greenland Ice Sheet, Devon Ice Cap, and Barnes Ice Cap mapped using Sentinel-2 imagery. *International Journal of Applied Earth Observation and Geoinformation, 78*, 1–13. https://doi.org/10.1016/j.jag.2019.01.008

Yang, K., and Smith, L. C. (2013). Supraglacial Streams on the Greenland Ice Sheet Delineated from Combined Spectral–Shape Information in High-Resolution Satellite Imagery. *IEEE Geoscience and Remote Sensing Letters, 10*(4), 801–805. https://doi.org/10.1109/lgrs.2012.2224316

Zwally, H. J., Abdalati, W., Herring, T. A., Larson, K. M., Saba, J. L., and Steffen, K. (2002). Surface Melt-Induced Acceleration of Greenland Ice-Sheet Flow. *Science*, *297*(5579), 218–222. https://doi.org/10.1126/science.1072708

Appendix

Qualitative time series analysis of Unnamed 2 and Henrietta-Nesmith glaciers discussed in section 2.4.1.

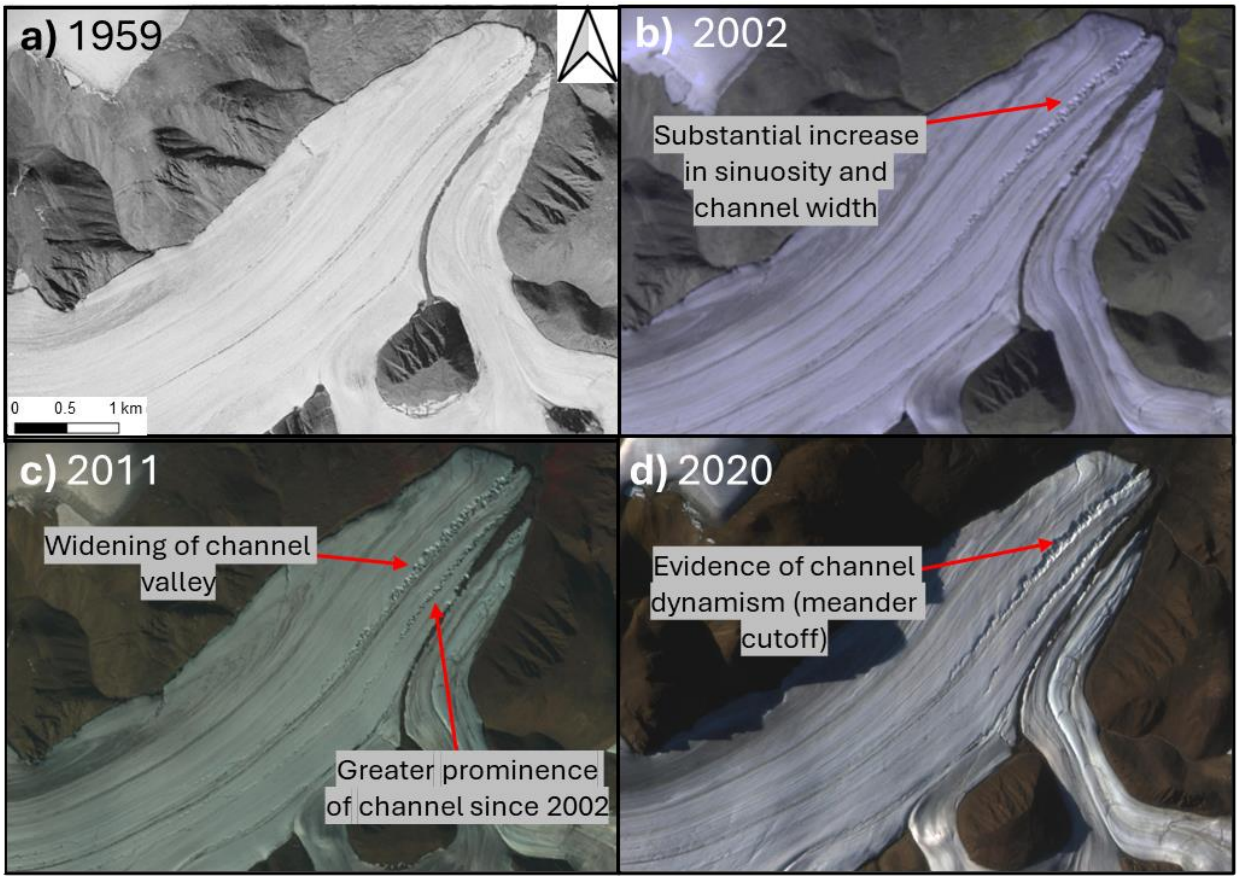

Figure 1-A. Channel evolution on Unnamed 2 Glacier between 1959 and 2020. a) ~0.6 m resolution historical air photo, b) 15 m resolution ASTER image, c) 10 m resolution SPOT-5 image, d) 3 m resolution PlanetScope image. The red arrows track the evolution of canyon rivers showing their increase in sinuosity, width and dynamism. See Tables 1 and 2 for image dates.

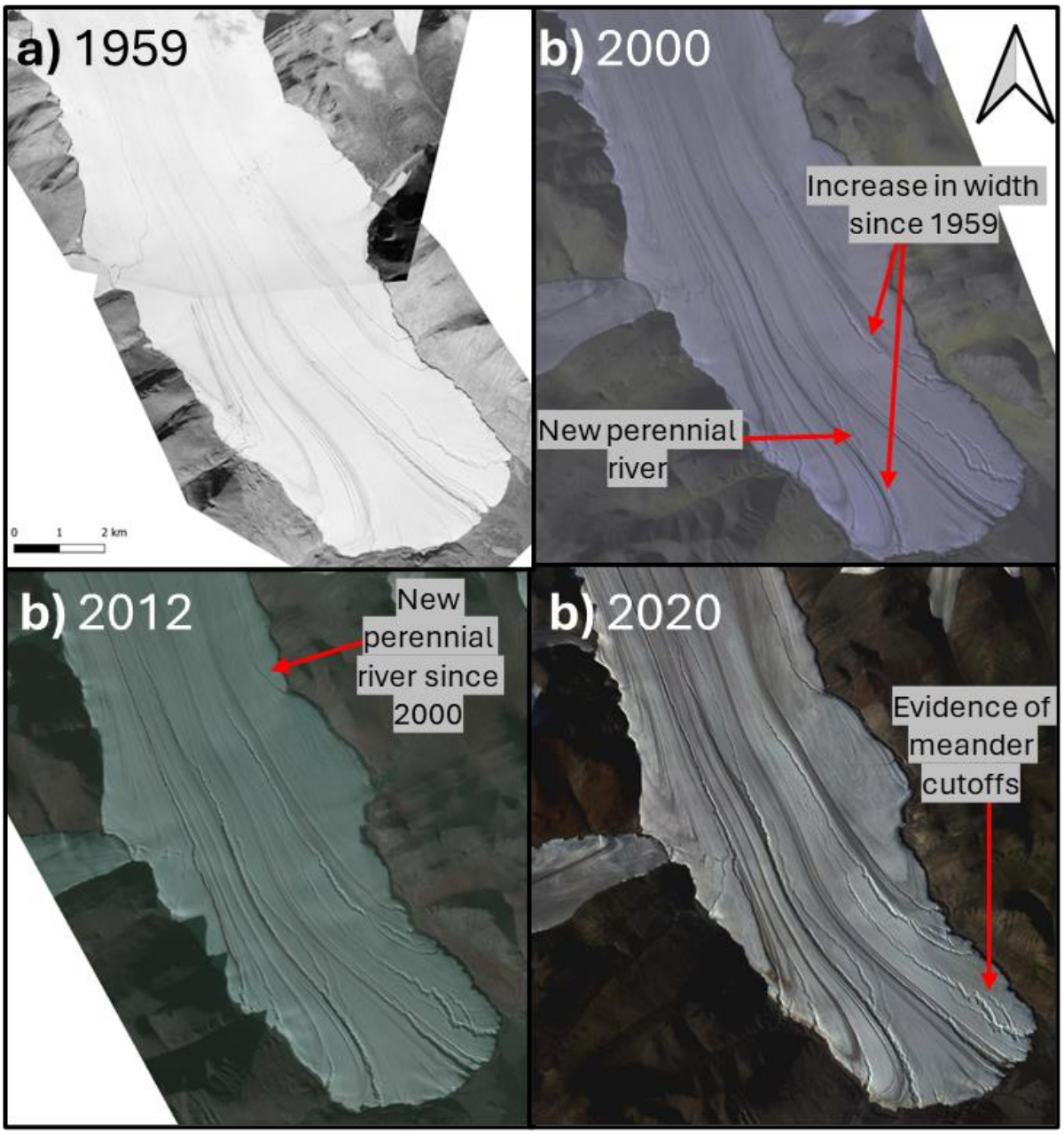

Figure 2-A. Channel evolution on Unnamed 2 Glacier between 1959 and 2020. (a) ~0.6 m resolution historical air photo, (b) and (c) 15 m resolution ASTER image, (d) 3 m PlanetScope image. The red arrows identify new rivers and show the evolution of perennial rivers, highlighting their increase in width and dynamism. See Tables 1 and 2 for image dates.

Comparison between channel model and 2020 manually delineated network on John Evans Glacier as discussed in section 2.5.3.

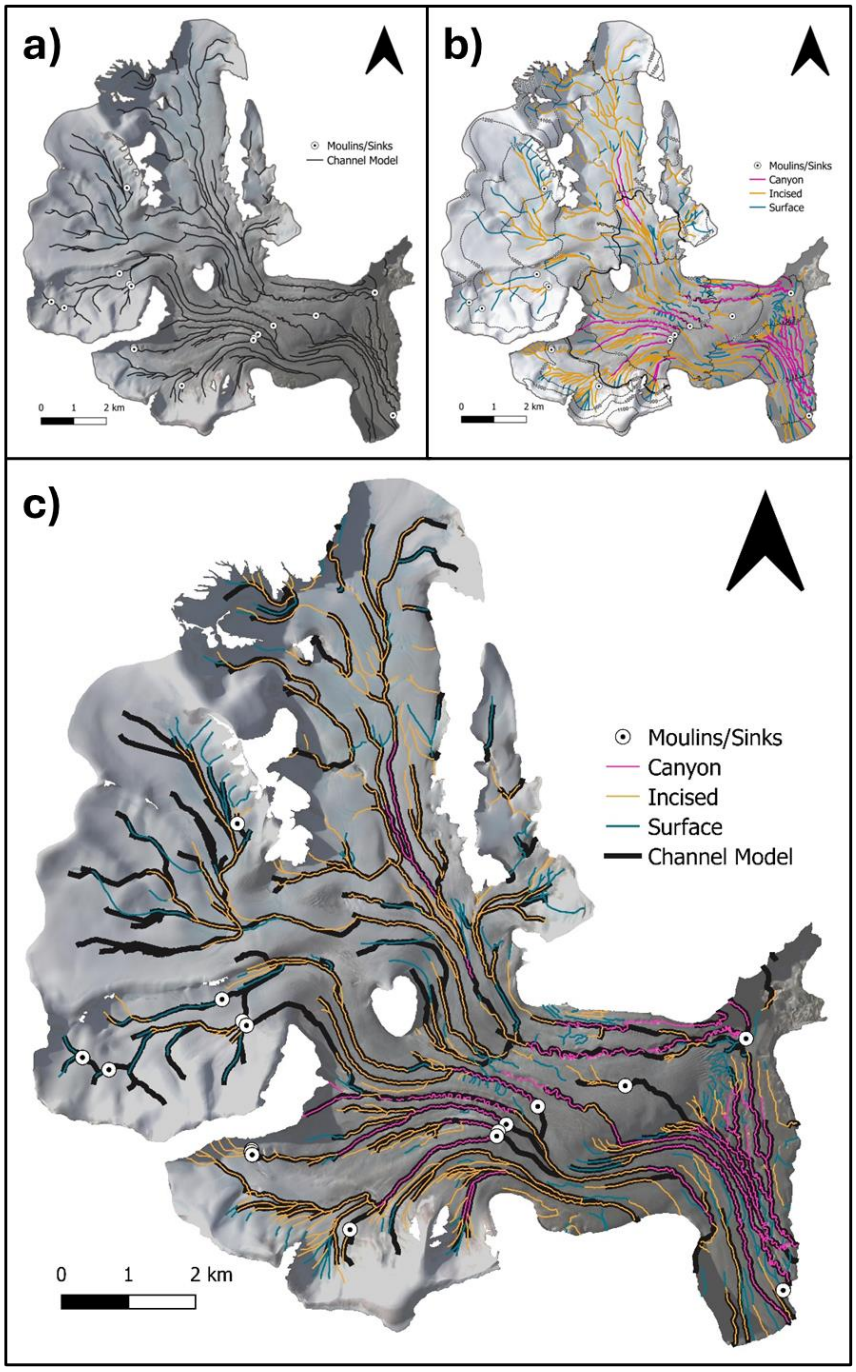

Figure 3-A. Comparison between channel polylines modelled using the D8 algorithm on an ArcticDEM strip from July 26, 2020, and the manually delineated channel networks on a PlanetScope image from July 23, 2020, on John Evans Glacier. a) Channel model polylines, b) manually delineated network, c) manually delineated network overlaid on the channel model polylines.